Master Thesis in Geosciences

COMPACTION, ROCK PROPERTIES AND AVO MODELING IN THE GOLIAT FIELD, SW BARENTS SEA

A petrophysical approach

Honore Dzekamelive Yenwongfai

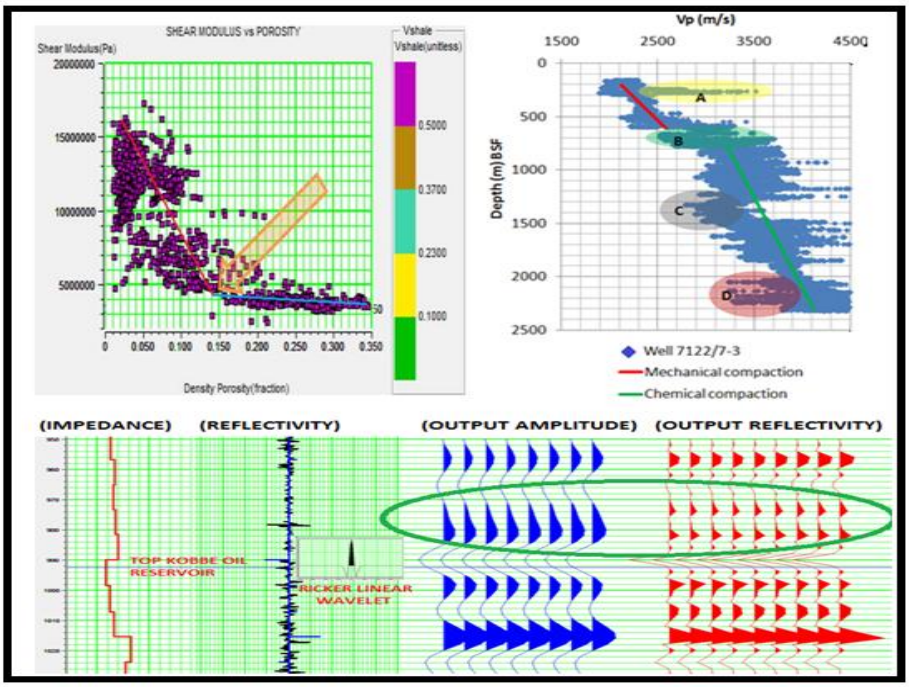

UNIVERSITY OF OSLO
FACULTY OF MATHEMATICS AND NATURAL SCIENCES

COMPACTION, ROCK PROPERTIES AND AVO MODELING IN THE GOLIAT FIELD, SW BARENTS SEA

A petrophysical approach

Honore Dzekamelive Yenwongfai

Master Thesis in Geosciences

Discipline: Petroleum Geology and Petroleum Geophysics

Department of Geosciences

Faculty of Mathematics and Natural Sciences

UNIVERSITY OF OSLO

[01.06.11]

Tutor(s): **Nazmul Mondol (UiO) and Jens Jahren (UiO)**

This work is published digitally through DUO – Digitale Utgivelser ved UiO

http://www.duo.uio.no

It is also catalogued in BIBSYS (http://www.bibsys.no/english)

Key words: Goliat Field, Compaction, AVO, Exhumation, Synthetic seismic

PREFACE

This thesis is part of the BarRock project and is submitted to the Section of Petroleum Geology and Petroleum Geophysics (PEGG), Department of Geosciences, University of Oslo (UiO) in candidacy of the, M.Sc. in Petroleum Geology and Geophysics.

This research has been performed at the Department of Geosciences, UiO during the period from January – May 2011 under the supervision of Associate Professors, Nazmul Mondol and Jens Jahren of the Department of Geosciences, University of Oslo, Norway.

DEDICATION

To Shufai wo Buea, Ma Ndi, Njingti's, Ngala's, Emesum's, Emma, Fredo, Leo and the entire Fai's family.

ACKNOWLEDGEMENTS

It would have been next to impossible to write this thesis without my supervisors, Associate professors Nazmul Mondol and Jens Jahren whose help, guidance, encouragement, and supervision from preliminary to concluding levels, enabled me acquire and develop new analytical techniques.

I am grateful to all my lecturers in the section of Petroleum geology and Petroleum geophysics, most especially, Johan Peter, Knut Bjørlykke, Faleide Inge, Roy Gabrielson, Leiv Gelius, Dag Karlsen, and Michael Heeremans for their support, constructive feedback and recommendations. I would always be indebted to you all.

Many thanks goes to my course mates in the Petroleum Geology and Geophysics who make up a significant diversity from different continents, and enabled me develop alternative models of thinking and an open minded culture.

I also want to acknowledge my study group mates, Abel Onana, Agus Fitriyanto, and Piratheeben K, who have stood by me all the way. Your team spirit, academic and social input will forever be missed. I want to convey thanks to Fawad Manzar for his constructive feedback and relevant discussions in this work.

I am grateful to the Emesum family, whose friendship, hospitality and love, enlightened and helped me stay focused. The good memories and times well spent will always be remembered.

Finally I want to thank all my friends, espacially Olivier Pamen, Daniel Ngembus, Ashu Mpame, Sone Brice, Geraldine Njumbe, Aghendia Alemngu, and last but not least Pongwe Fadimatou. Your moral, emotional, and spiritual support throughout my studies will forever be cherished.

ABSTRACT

The PDO approved Goliat Field, situated on the Finnmark Platform in SW Barents Sea region represents the first oil field to be developed on the Norwegian Barents shelf. Cenozoic exhumation still poses significant challenges in developing frontier exploration models due to its effects on the different elements in a petroleum system.

Understanding the nature of the transition from mechanical to chemical compaction, the degree of overconsolidation and AVO modeling of selected reservoir intervals is the main theme of this work. Data from six wells, laboratory compaction curves and published shale compaction trends have been used to evaluate the rock properties as a function of depth. AVO synthetic single interface models have been carried out using Hampson-Russel.

Experimental laboratory compaction data coupled with compaction trends in the Goliat Field indicate that the amount of exhumation ranges between 700 – 1500m. An integration of the Vp-depth trend together with a porosity-shear modulus cross plot, show that the transition from mechanical to chemical compaction for siliciclastic rocks occurs at approximately 600m BSF. This temperature controlled transition represents a silica phase transformation. The Chemical compaction trends show a smaller change in Vp with depth compared to the mechanical compaction domain. Velocity inversion with depth due to the presence of source rocks, effect of pore fluid and pore pressure has been demonstrated for different wells.

AVO modeling for different fluid saturation scenarios indicates that the synthetic seismic is sensitive only to the initial 10% gas saturation in oil – gas system, with the saturated bulk modulus being the main controlling parameter. The insitu AVO response for the Tubåen reservoir is class IV, meanwhile the Kobbe reservoir gives a class III signature. The corresponding gas models indicate that, ΔVs and Poisson's ratio are key parameters increasing the reflectivity with offset (angle), meanwhile the impedance contrast in the half space single layer models determines the magnitude of the reflection coefficient in both the Tubåen and Kobbe reservoirs.

This study demonstrates that AVO modeling can be used for fluid prediction ahead of drilling during exploration and reservoir monitoring during production. Uplift estimates can be used to correct the porosity depth relationships used in reservoir characterization work flows, and also in assessing the degree of tertiary migration from traps due to exsolution of gas.

TABLE OF CONTENTS

CHAPTER 1 GENERAL INTRODUCTION

1.1 General

In recent years, as the easy to find conventional hydrocarbon reserves in the earth's crust are being exploited, the oil industries tend to search in more difficult terrains like the arctic and much deeper waters to match the growing demand for fossil fuels. Also, the global demand for fossil fuel continues to grow unfortunately at a time when the size of new hydrocarbon finds is progressively decreasing. As such, exploration for oil and gas over time has advanced from being qualitative to quantitative. Quantitative studies of the subsurface in general and hydrocarbon fields in particular, require a lot of integrated data and analysis from geologists, geophysicists, petrophysicists, and reservoir engineers.

Fueled by progressive technological advances and breakthroughs in the oil and gas industry, the possible computing power has also followed suite such that reservoir characterization has extended from deterministic to probabilistic. Accurate characterization requires a combination of 3D and 4D seismic volume interpretations, seismic inversion and amplitude analyses, rock physics and AVO (amplitude versus offset) analysis. In some cases neural networks are also applied to create 3D volumes of petrophysical properties to model inter-well data, thus establish and visualize the spatial variations in reservoir parameters (Goffrey, 2007). Earlier, geophysical data were mainly used in exploration, and to a smaller extent in the development of discoveries. In more recent times geophysical and petrophysical data is integrated in reservoir characterization schemes, and serves as a link between geologic reservoir properties (such as porosity, sorting, clay content, lithology and saturation) and seismic properties (like P-wave and S-wave velocities (Vp/Vs ratio), acoustic impedance, elastic moduli, bulk density) (Avseth et al., 2010). Reservoir characterization therefore simply refers to quantitatively assigning reservoir properties which usually show a non-uniform and non-linear spatial distribution. As a consequence of this reservoir heterogeneity, effective rather than absolute quantitative reservoir parameters become much more important as input for reservoir simulations and subsequent optimal field development (Mohaghegh et al., 1996). By applying an integrated approach in reservoir characterization together with geostatistics (because a simple average of data from even closely spaced wells may lead to a misleading analysis), an adequately constrained reservoir model will be the end result, which can then be

used to quantify the hydrocarbons in place and also in optimizing hydrocarbon production (Jarvis, 2006).

This study will focus on an integrated approach to reservoir characterization of the Goliat field, located on the sub area Finnmark West close to the Hammerfest Basin in the southwestern part of the Barents Sea (Norwegian sector block 7122). A suite of quality controlled well logs will be used to infer the rock property variations with depth in the study area. Well logs will then be used to build high frequency synthetic seismograms to perform AVO modeling.

1.2 Exploration history in the Barents Sea area

In terms of surface area, the Barents sea (245,000 Km^2), is significantly larger than the Norwegian North Sea (130,000 Km^2) (Figure 1.1). Despite its size, the success rate in the Norwegian Barents Sea (one in three wells) is higher than the Norwegian North Sea, with respect to the number of dry wells drilled before the first commercial discovery (Ohm and Karlsen, 2008). A number of 32 dry wells preceded the Ekofisk hydrocarbon field in the Norwegian North Sea. Meanwhile more than 100 dry wells were encountered prior to the Dutch Groningen discovery in the southern part of the North Sea. Approximately one out of three wells generally has been successful in the Barents Sea (Ohm and Karlsen, 2008). Also multiple source rock intervals at different stratigraphic intervals and have been documented in the Barents Sea unlike the North Sea with just one major source rock (Kimmeridge shale) which is equivalent to the Hekkingen Formation. Previously the most common play models in the Barents Sea region involved mainly gas prospects such as the Snøhvit. The hydrocarbon products are usually ranked to be less commercial because of predominance of gas over oil and the distance to the gas market is also an issue. The predominance of gas over oil has been attributed to uplift in this area. However oil discoveries such as the Goliat and Nucula, has implications for established exploration models in this area. These models need to take into consideration long distance migration as a result of different episodes of uplift and also the dynamic nature of traps. A more recent significant oil discovery in Skrugard prospect (1250m BSF in well 7220/8-1), has been made by Statoil ASA, and partners Eni Norway and Petoro in April 2011. This discovery is located about 100 Km North of the Snøhvit gas field and has an estimated 150-250 million recoverable barrels of oil equivalent (Eni Norway Goliat

Factpage). This discovery represents an important break-through for frontier exploration activities in this area.

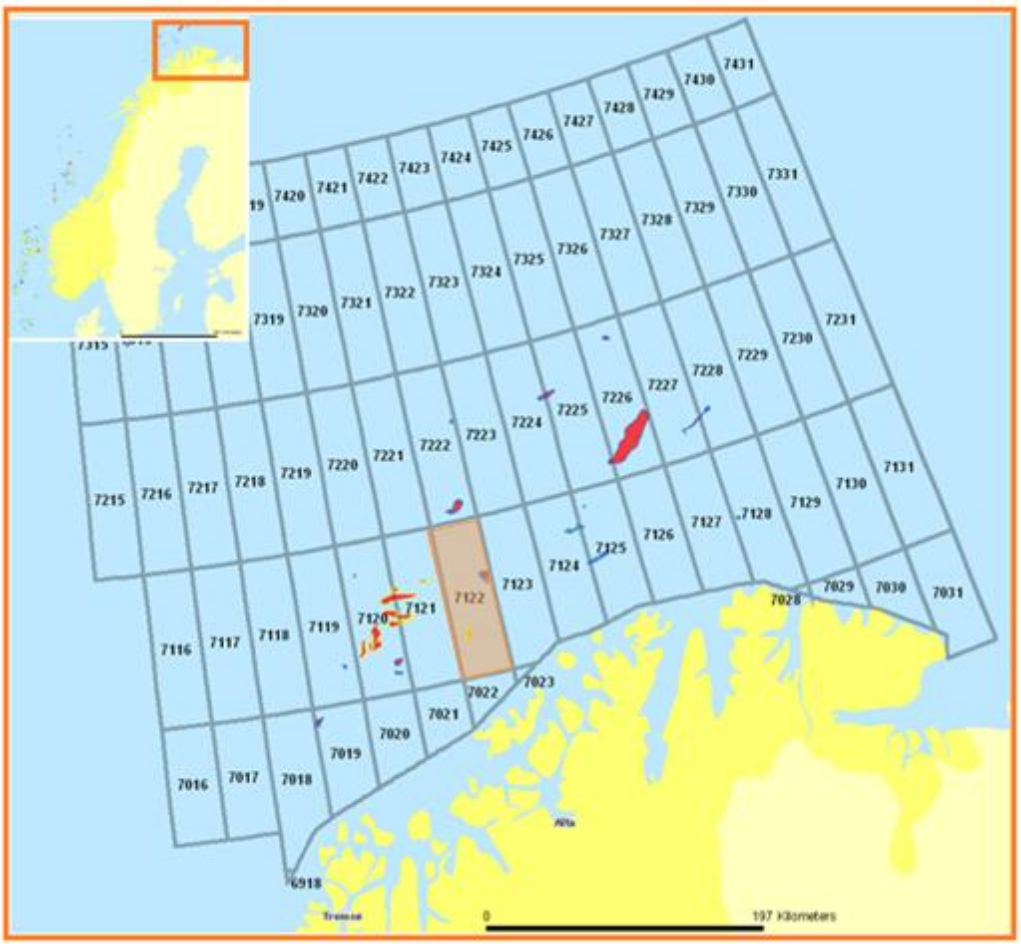

Fig. 1.1 Barents Sea exploration activity.

1.3 Goliat field

The Goliat field is a PDO (Plan for Development and Operation) approved field located in block 7122/7 and 7122/8 (Figure 1.2) in the Norwegian sector of the Barents Sea (Production Licence 229 awarded in 1997). It is about 50 km southeast of the Snøhvit field in the sub area Finnmark West and about 85 km northwest of Hammerfest. It is the first oil field to be developed in the Norwegian sector of the Barents Sea. The licensees of PL229/229B are partitioned between two equity partners; Eni Norge (operator) has 65% meanwhile Statoil Petroleum AS has 35% of equity interest in Goliat field (NPD Factpages).

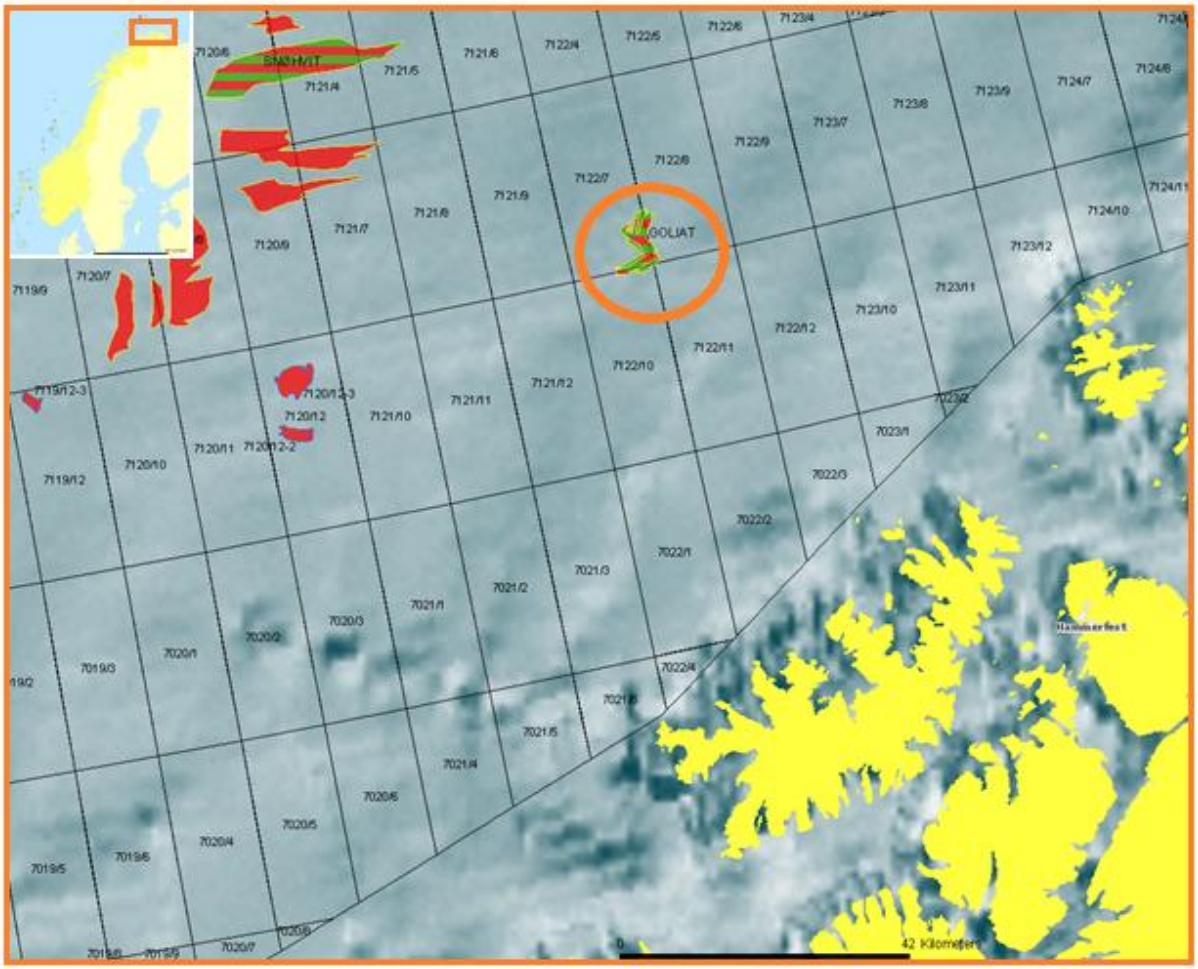

Fig. 1.2 Location map of Goliat Field (NPD Factpages).

Unlike most discoveries in the Barents Sea which are rather gas prone than oil prone, the Goliat field is mainly a crude oil field with a relatively smaller volume of natural gas. This discovery came to light from the first exploration well (7122/7-1) in 2000. The water depths in this area between 360 – 420m (Eni Norway Goliat Factpage). The reservoir lies at about 1100m. A total of 6 wells have been drilled in this area with one well 7122/7-5 being a dry well among the other success stories. The two main reservoir intervals in this field are the Kobbe Formation (Sassendalen Group) of Triassic age and the Tubåen and Fruholmen Formations in the Realgrunnen Subgroup (Kapp Toscana Group) of Jurassic age. Both are oil discoveries with an additional thin gas cap. A couple of other discoveries have been documented in the Snadd Formation (Upper Triassic) and the Klappmyss Formation (Lower Triassic). The main reservoirs in this field are located within the Triassic (NPD Factpages).

The development phase of this field started in the last quarter of 2009, using the Sevan FPSO (Floating Production, Storage and Offloading) 1000 concept. This field is to be developed

with eight integrated subsea templates and about 32 well slots tied to the circular FPSO system (NPD Factpages). Production is estimated to begin by the last quarter of 2013. The pressure in most of the reservoir intervals is low, for example 123 bars have been documented for Realgrunnen Subgroup and 192 bars for Kobbe Formation (Eni Norway Goliat Factpage). As a result, this field will be produced with water injection to optimize recovery.

During the early phases of production, associated gas will be re-injected into the Kobbe Formation until export through the Snøhvit pipeline to Melkøya is possible (NPD Factpages). The low pressures in the reservoir represent a positive element for well control but on the other side of the coin, more artificial energy input in terms of water flooding is necessary to maintain reservoir pressures during production and thus optimize recovery. There is a relatively small support from a natural gas drive due to the thin gas cap. The anticipated production profile indicates a build-up to 5.4 million Sm^3/year by the second year of production followed by a relatively rapid decline to 1.7 million Sm^3/year, then a steady reduction to 0.5 million Sm^3/year (Eni Norway Goliat Factpage). It is anticipated that the maximum volume of gas production including re-injection will take place one year after the onset of production. This volume is estimated at 1300 million Sm^3 / year. Goliat is expected to produce for a period of about 15-20 years. Technological advances coupled with any additional discoveries within its vicinity will probably be important in extending the life of this field.

1.4 Research Objectives

The aim of this thesis is to set an initial framework for compaction and AVO modeling in the Goliat oil field. This involves qualitative and quantitative description of the lithologic and fluid properties of several effective reservoir intervals in the uplifted Goliat field. Emphasis is laid on the shallower, thin Early Jurassic Tubåen reservoir and the deeper and thicker Mid-Triassic Kobbe reservoir. An integrated study is therefore paramount to these outlined objectives;

1. Assess the effect of lithology, pore fluid and pore pressure on the general rock compaction trend.

2. Quantify the total amount of Cenozoic uplift affecting the Goliat oil field, and assess the depth and nature of the transition from mechanical to chemical compaction for the siliciclastic rocks.

3. Fluid prediction and substitution in determined reservoir intervals by theoretically replacing the insitu fluid phase and monitoring the corresponding changes in the synthetic seismic response.

4. Rock physics AVO modeling and classification of specific reservoir intervals.

1.5 Database and Methodology

This research employs an integrated approach, combining a petrophysical study from well data and synthetic seismic data, to qualitatively and quantitatively determine reservoir properties of the Goliat field.

Table 1.1 Well data and status (modified from NPD Factpages).

Well	Entry date	Completion date	Purpose	Content
7122/7-1	16.09.2000	05.10.2000	W	Oil
7122/7-2	12.09.2001	19.10.2001	W / A	Oil
7122/7-3	24.10.2005	08.01.2006	W / A	Oil/Gas
7122/7-4S	21.09.2006	25.11.2006	W / A	Oil/Gas
7122/7-5A	23.12.2006	13.01.2007	W / A	Oil

The data used throughout this work for analysis is based on a complete suite of 6 wells, drilled through Goliat field (Figure 1.3). Most of these wells are wildcat (w) and appraisal wells (A) and one well being a dry well (7122/7-5). The wildcat and appraisal wells used include; 7122/7-1, 7122/7-2, 7122/7-3, 7122/7-4S, and 7122/7-5 A. With production scheduled to commence in 2013, the status of these 5 wells (Table 1.1) is now in the appraisal and production phase.

Fig. 1.3 Well locations superimposed on the outline of the Goliat Field (NPD Factpages).

Data analysis and interpretation has been based on the Geoview, Elog, AVO modules in the Hampson-Russel software packages. Elog module has been used for well log conditioning and AVO module was used to generate and extract amplitudes from synthetic seismic data.

AVO modeling for 'in-situ' and 'what if' scenarios has been carried out in this work. This has been used to determine the expected AVO anomaly, based on some principles such as Biot-Gassmann fluid substitution model.

In addition to the well database, laboratory mechanical compaction data for pure sandstones (Etive sand), synthetic silt-clay mixtures and published compaction trends have been used for the compaction study. A detail description of materials and methods is given in the relevant chapter.

1.6 Chapter description

Chapter 2 will describe the regional structural and stratigraphic setting of the Barents shelf area and also give an overview of the petroleum system in the Goliat oil field based on published data.

Chapter 3 will focus on compaction, rock properties, and exhumation estimates in the study area. A brief theoretical background, comprehensive methodology and available data set is presented in this chapter. Major findings with regards to exhumation and compaction trends are also discussed, along with the effects of pore fluids, pore pressure and source rocks.

AVO fluid replacement modeling and classification of some defined target reservoir intervals will be the main focus in chapter 4. A theoretical framework and the assumptions used in modeling the target reservoir zones are also outlined. A sensitivity analysis, variations in AVO half space models, and effect of block size are also discussed in this chapter.

Chapter 5 will then provide a summary of the entire work and the major conclusions arrived at from the results obtained from the available data set.

CHAPTER 2 REGIONAL GEOLOGIC SETTING

2. I Structure and Tectonic

The physiographic association of the Goliat Field in the Barents Sea together with other known chains of circumpolar basins such as the Sverdrup Basin and Mackenzie Delta of Canada, Western Siberia Basin, Mid-Norwegian Shelf and the North Sea amongst others, makes this area of the globe particularly interesting for hydrocarbon exploration. The Barents shelf is located on the north-western edge of the Eurasian plate, with average water depths of about 300m, defining an area of about 1.3 million km^2. According to Larsen et al. (1993), the area open for hydrocarbon exploration in this area covers an area of about 230000km^2 which compared to the Norwegian sector of the North Sea is more than one and a half times its area.

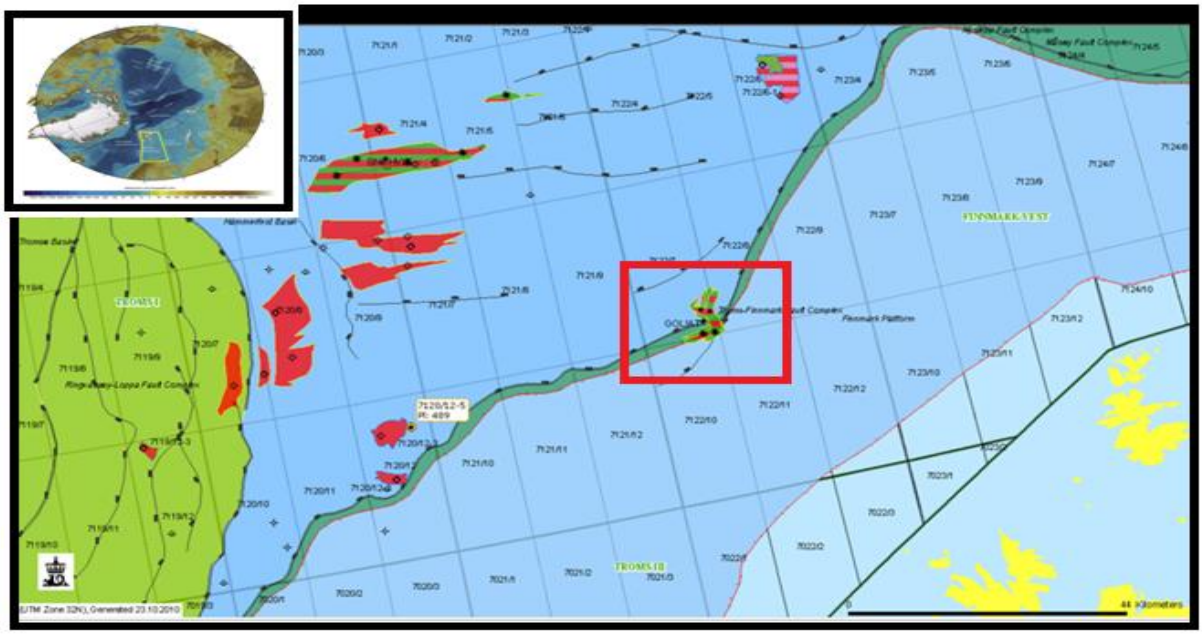

Fig. 2.1 Map showing the Goliat Field and the Troms-Finnmark Fault Complex (modified from NPD website). Bathymetric map modified from Jacobsson et al. (2008).

The Goliat field cuts across the Troms-Finnmark fault complex and sits on the sub area Finnmark West in the southwestern part of the Barents Sea (Figure 2.1). The geologic history of most sedimentary basins usually involves an interesting interplay between tectonic subsidence, possible reactivation of older faults and sediment supply ultimately affecting the basin infill and the South Western Barents shelf is no exception. Two major continental collisions and resultant orogenies typify the early history of the Barents shelf. The Caledonian

Orogeny closing the Iapetus Ocean approximately 400 Ma and the Uralian Orogeny representing one of the last collision elements in Permian-Triassic times creating the supercontinent, Pangea. These major Orogenies dominate the basement substructure of this area, and it is thought to have influenced later structural development (Glørstad-Clark et al., 2010).

Subsequent to Orogenic episodes, the Barents Sea area became dominated by later periods of extension, beginning with the collapse of the previous orogenic belts and progressive breakup of the already established Pangea supercontinent during the Late Paleozoic and Mesozoic. This resulted to a complex mosaic of platforms, structural highs and rift basins across the Barents shelf (Johansen et al., 1993) as shown in Figure 2.2.

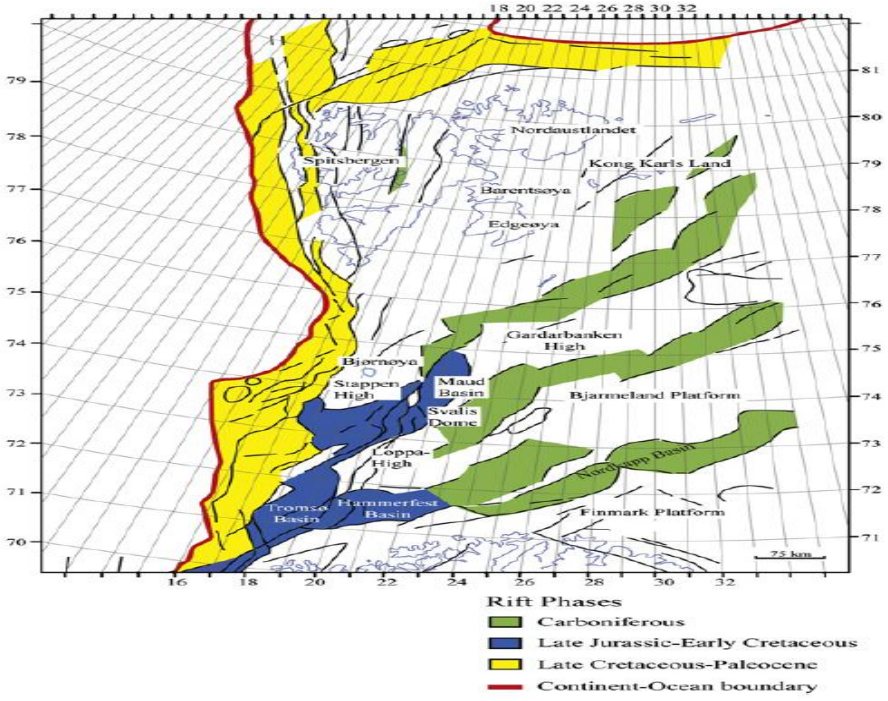

Fig. 2.2 Main Structural Elements in the Barents Sea (Faleide et al., 2008, Gabrielsen et al., 1990, Gudlaugsson et al., 1998).

The colors shown in Figure 2.2, show the focus of tectonic activity through time in the Western Barents Sea. The focus of tectonic activity is seen to progress towards the west over geologic time. The Hammerfest Basin is shown to be the main area of tectonic activity in Late Jurassic – Early Cretaceous times.

2.2 Stratigraphy

The Barents shelf stratigraphic succession shows two major distinct sets of lithologies at different Periods in its geologic history. The Devonian, Carboniferous and Permian on the Barents Shelf is dominated by carbonates with some evaporites. Meanwhile the Triassic and younger sediments are mainly represented by clastic sediments (Figure 2.3). This correlates well with the drifting of the entire Barents shelf from warmer paleolatitude of 20^{o}N during the Carboniferous to a colder paleolatitude of 55^{o} N during the Triassic and finally to present day 75^{o}N. This clearly demonstrates a combined tectonic and climatic influence on lithology, as progressively more temperate conditions prevailed (Worsley et al., 1986). The Triassic in the Western Barents sea area rather represents a relatively quiet period with svalbard inclusive ,in contrast to the Northern and Southern Barents Sea Basins which were progressively forming depocenters through significant subsidence in these regions (Riis et al., 2008). Acording in to Mørk et al. (1989), relatively thick Triassic clastic units (Figure 2.4) are present throughout the Barents Sea usually showing coarsening upward sequences thus indicative of transgressive-regressive depostional cycles. Multiple source rock intervals have been documented in the Barents sea stratigraphy, from Carboniferous to Cretaceous (Ohm and Karlsen, 2008).

The Lower-Middle Jurassic interval in the study area (Figure 2.4) is represented mainly by sandstones which extend throughout the Hammerfest Basin and possibly also covered the Loppa High and Finnmark Platform, but probably exhumed and eroded during later tectonic events (Glørstad-Clark et al., 2010).

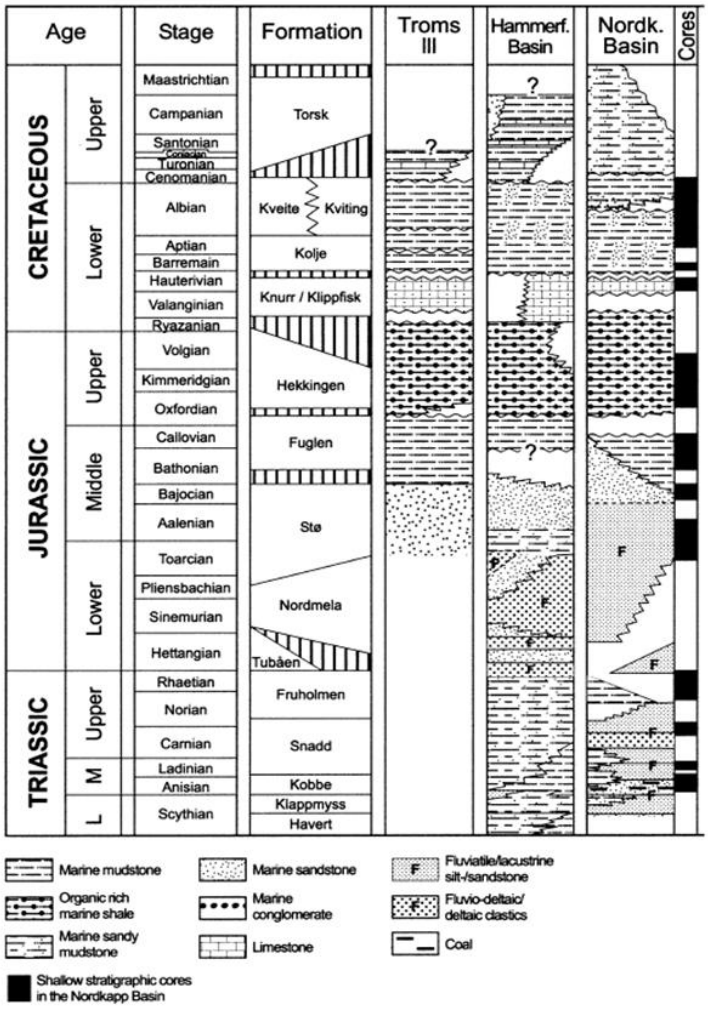

Fig. 2.3 Regional stratigraphy of the Barents Shelf. The cored interval in the Nordkapp basin are shown (modified after Bugge et al., 2002).

The stratigraphy of the Goliat Field on the Finnmark platform shows an incomplete stratigraphic section. This is the result of the Pliocene-Pleistocene glaciations, which eroded most of the Paleogene and Neogene stratigraphic units. This erosion is more significant from the eastern Barents Sea, with shallow units like the Torsk and Kviting Formations present in the Hammerfest basin, but eroded out in the Bjarmeland Platform, Nordkapp Basin in the east. The deepest well in this field is well 7122/7-3 and goes as far deep as the Permian with the oldest unit being the Tempelfjorden Group (Table 2.1). The complete stratigraphy encountered in well 7122/7-3 is shown in Table 2.2. The focus in this study will mainly be on the Mesozoic Sub-Era and of particular interest the Triassic and Early Jurassic Periods.

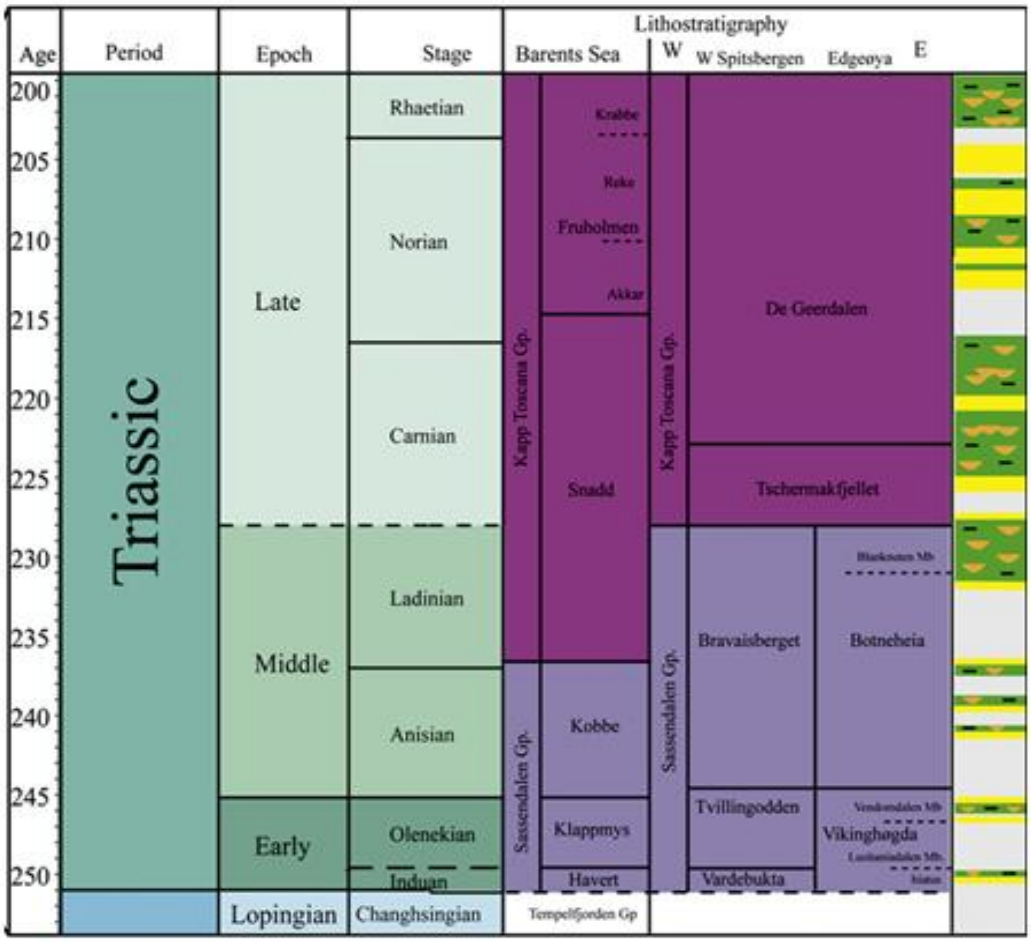

Fig. 2.4 Lithostratigraphy of the Triassic in the Western Barents Sea (modified after Glørstad-Clark et al., 2010).

Table 2.1 Well bores and corresponding oldest Group and Formations penetrated.

Well bore	Total Depth [m] KB	Oldest Unit	Age	Kelly bushing elevation KB [m]
7122/7-1	1524	Snadd Fm	Triassic	24
7122/7-2	1418	Snadd Fm	Triassic	18
7122/7-3	2726	Tempelfjorden GP	Permian	25
7122/7-4S	2550	Havert Fm	Early Triassic	23
7122/7-5A	2186	Kobbe Fm	Middle Triassic	23

The lithostratigraphic description of the Kapp Toscana Group and the Sassendalen group that follow are based mainly on published data in the Hammerfest Basin and other closely related structural basins (NPD Factpages).

Table 2.2 Formations and Groups encountered in well 7122/7-3 (NPD fact pages).

Top Depth m (BSF)	Top Name
0	NORDLAND GP
266	NYGRUNNEN GP
266	KVITING FM
282	ADVENTDALEN GP
282	KOLMULE FM
497	KOLJE FM
592	KNURR FM
650	HEKKINGEN FM
705	FUGLEN FM
719	KAPP TOSCANA GP
719	TUBÅEN FM
812	SNADD FM
1440	SASSENDALEN GP
1440	KOBBE FM
1676	KLAPPMYSS FM
1844	HAVERT FM
2227	TEMPELFJORDEN GP

2.2.1 Kapp Toscana Group

This group is dominated by sandstones, siltstones and shales, with age ranging from Late Triassic to Middle Jurassic (Ladinian to Bathonian) and it is exposed along the Tertiary fold-thrust belt on Spitsbergen, Barentsøya, Edgeøya, Hopen, Kong Karls Land and Bjørnoya. It also extends southwards across the Barents Sea Shelf to the Bjarmeland Platform, the Hammerfest and Nordkapp basins. This group has been interpreted in general to have been deposited in a nearshore deltaic environment characterized by shallow marine and coastal reworking of fluviodeltaic and deltaic sediments (Mørk et al., 1982).

The main reservoir units of interest in the Kapp Toscana Group from the Goliat Field are represented by the Tubåen, Fruholmen (Realgrunnen Sub Group), Snadd (Storfjorden Sub Group) and Kobbe Formations.

2.2.2 Sassendalen Group

This group is dominated by shales and siltstones with subordinate sandstones and minor carbonate intervals. This group is of Early and Middle Triassic and is exposed along the Svalbard Tertiary fold belt, Barentsøya, Edgeøya, southwestern Nordaustlandet and Bjørnoya continuing in the subsurface southwards in the Barents Sea shelf to the Hammerfest basin. This group has been interpreted to represent coastal, deltaic to shallow shelf deposits in Western Spitsbergen. This group is represented by a series of stacked transgressive-regressive successions, each formation being initiated by a regionally significant transgression (Mørk et al., 1989).

2.3 Petroleum system

A petroleum system takes into consideration a pod of active source rock and its genetically related oil and gas accumulations. This includes all the geologic processes and elements which are essential ingredients for a hydrocarbon accumulation to occur. The essential elements include; source rock, reservoir rock, seal and overburden. The two main processes that need to be present include; trap formation and generation-migration-accumulation of hydrocarbons. All events and processes need to be placed correctly in time and space to obtain a higher probability for the occurrence of a functioning petroleum system. It is this interdependence of the different elements and processes to form a hydrocarbon accumulation that makes it a system. The proven hydrocarbon reserves in the Goliat field are evidence of a working petroleum system. This petroleum system, like others on the Barents shelf, has suffered the effects of different episodes of Cenozoic exhumation and erosion. This triggered tertiary migration from the available traps. Uplift and erosion also possibly raised the source rock ‘kitchen’ to shallower depths thus reducing its potential for producing more hydrocarbons. This has serious consequences for exploration within such a context. An overview of different source and reservoir intervals in the Barents Sea region has been adequately summarized in Figure 2.5 by Dore (1995).

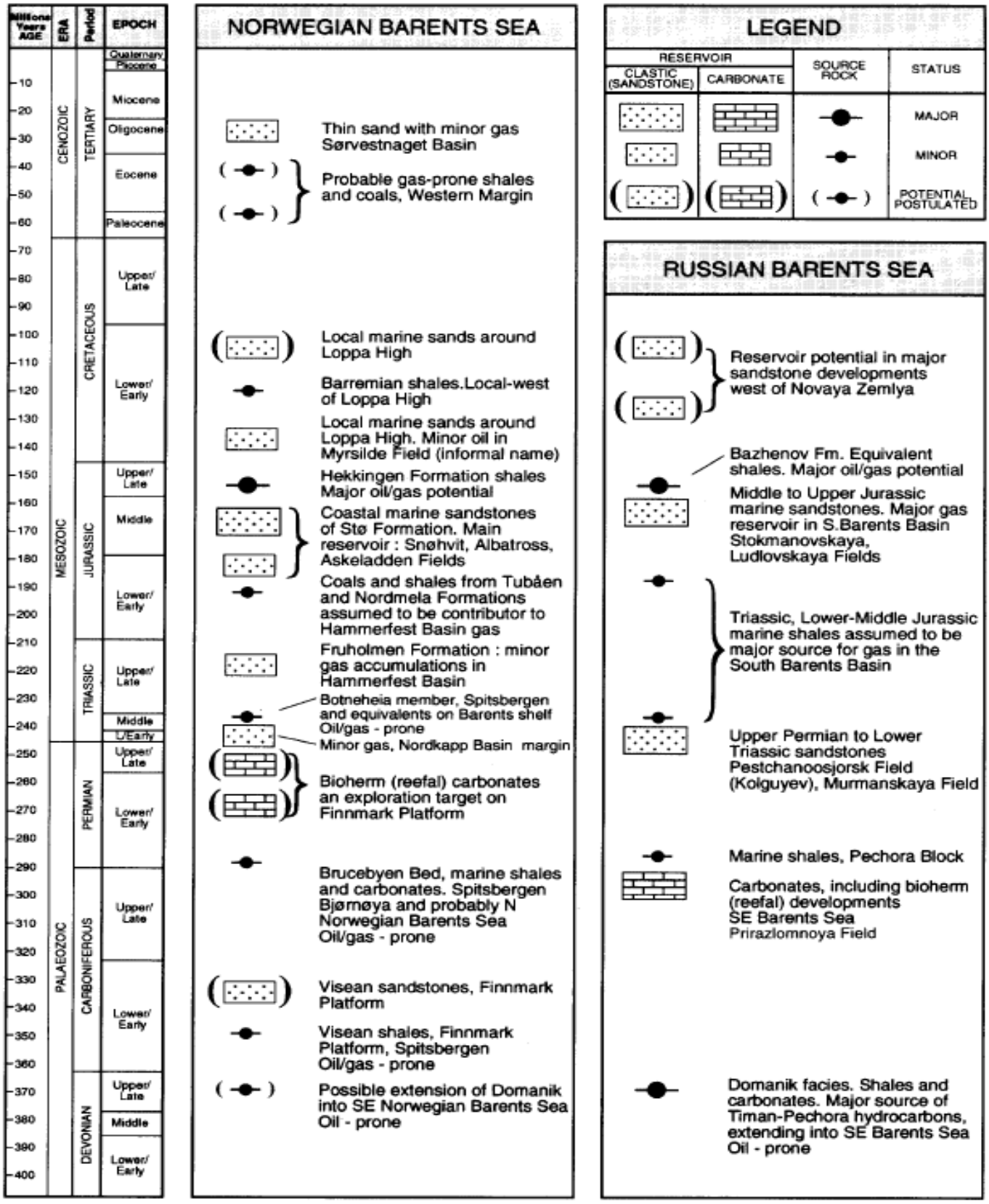

Fig. 2.5 Major source and reservoir rocks in the Barents Sea area (adapted from Dore, 1995).

2.3.1 Source Rock

This refers to a rock rich in organic matter (kerogen), which will generate hydrocarbons if exposed to sufficient burial temperatures in the sedimentary basin. The most widely distributed source rock candidate in this area is the Hekkingen Formation which is composed of dark organic rich shales. The Hekkingen Formation (Figure 2.6) in the Barents Sea is the equivalent of the Kimmeridge marine clay formation in the North Sea. This unit was deposited in anoxic deep marine conditions, as consequence of the local barriers to circulation created by the Kimmerian movements (Dalland et al., 1988). The Hekkingen formation belongs to the Adventdalen Group, deposited during the regional Bathonian/Callovian marine transgression.

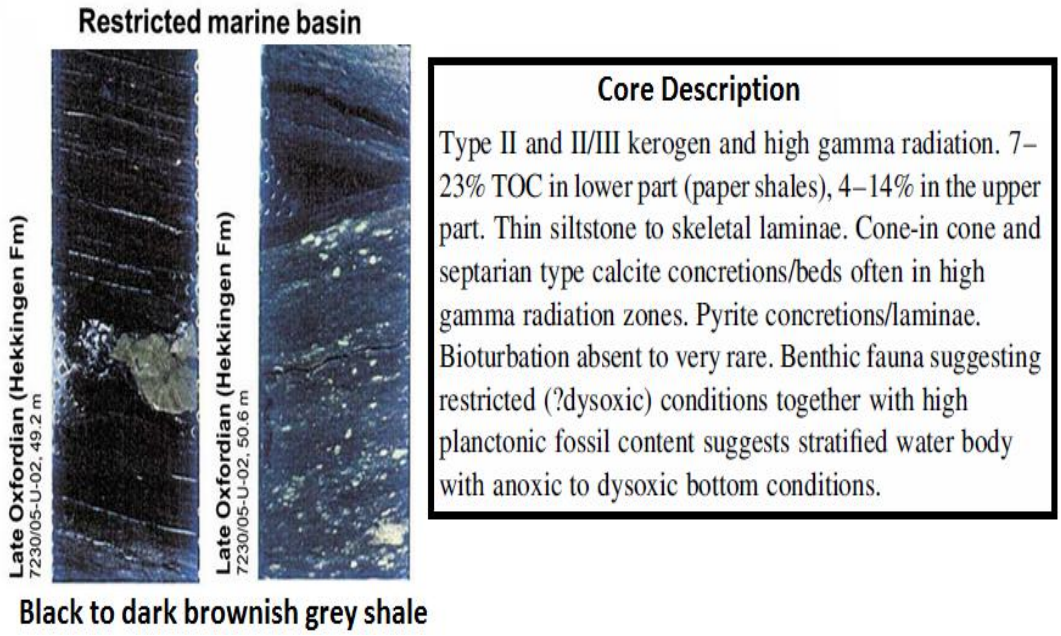

Fig. 2.6 Core description of the Hekkingen Formation (adapted from Bugge et al., 2002).

The Hekkingen Formation is the most prolific in terms of its TOC (Total Organic Carbon) and hydrocarbon generative potential. However the Fuglen formation in the same study shows a more marine dominated depositional environment than the Hekkingen formation. Other potential source rock intervals discussed in are found in the Nordmela, Tubåen, Snadd, Kobbe formations including some source potential in the Permian (Ohm and Karlsen, 2008). According to Ohm and Karlsen (2008), most of the Triassic source rocks enter the oil window, when the Hekkingen Formation is just early mature. Meanwhile the Triassic source rocks enter the gas window when the Hekkingen Formation becomes oil mature. In addition,

it was tentatively concluded based on isotope geochemistry, that Permian and Carboniferous source rocks, yield oils with the lightest isotope values, meanwhile the Triassic sourced intervals, yield rather intermediate, Isotope values.

Salt has a high thermal conductivity and tends to locally pull up the isotherms. The presence of salt in the Nordkapp Basin has enhanced the maturity of the Hekkingen Formation in that area. The Hekkingen Formation on the other hand gives rise to oils with heavy isotope values. However most of the oils found in the traps in the Goliat field have mixed isotope geochemical signatures, due to the variety of source rocks present in the different stratigraphic intervals. Uplift and erosion, has negative consequences for hydrocarbon generation from the source rocks on the Barents shelf. However, evidence of non-cogenetic gas has been documented in this area, indicating the presence of a live petroleum system in the area (Ohm and Karlsen, 2008).

2.3.2 Reservoir units

The main reservoir units encountered in the well data in this study are the Tubåen, Fruholmen, Snadd, Kobbe and Klappmyss Formations. During the deposition of the Adventdalen Group, sandstone distribution was restricted to local highs and platforms. The Triassic interval is important in the Goliat Field due to the reservoir intervals deposited during that period. The corresponding Lower Upper-Triassic (Carnian) reservoir units further north had a volcanic provenance area. This makes them relatively texturally and mineralogically immature and hence more susceptible to diagenetic alterations at depth, compared to areas further south. Areas further south such as the Finnmark platform, were under the influence of continues progradation from the Baltic Shield which represents a relatively mature provenance, with primary reservoir quality increased by marine reworking in near-coastal environments during highstand (Worsley, 2008).

The lithostratigraphic descriptions of these reservoir units are based on Dalland et al. (1988).

- **Tubåen Formation**; this formation belongs to the Realgrunnen Sub Group of the Kap Toscana Group and is dominated by sandstones with subordinate shales and minor coals. It shows a tripartite development, with a shale interval sandwiched between sand-rich units. This unit is probably distributed sub parallel to the Troms-Finnmark Fault Complex. The base of this formation is of Late Rhaetian to early Hettangian

though it probably extends locally into the Sinemurian. The sand intervals in the Tubåen Formation have been suggested to represent a stacked series of high energy marginal marine (tidal inlet dominated barrier complex and/or estuarine) environments.

- **Fruholmen Formation**; this formation belongs to the Realgrunnen Sub Group of the Kap Toscana Group. The base of this unit is early Norian while the top is thought to be rather diachronous at the Triassic-Jurassic transition. Open marine shale intervals in this formation grade to coastal and fluvial dominated sandstone sequences (Figure 2.7). This formation represents a depocentre in south with northward fluviodeltaic progradation.

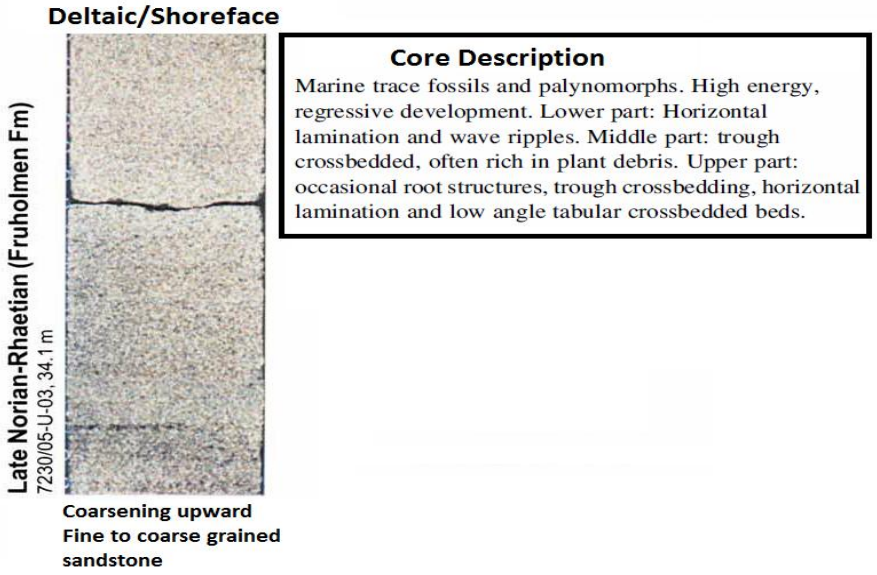

Fig. 2.7 Core description of the Fruholmen Formation (adapted from Bugge et al., 2002).

- **Snadd Formation**; this formation belongs to the Storfjorden Sub Group of the Kap Toscana Group and it is of a Ladinian to early Norian age. This unit generally shows a coarsening upward succession from basal grey shales, into shales with interbeds of grey siltstones and sandstones (Figure 2.8). The lower and middle portions of this formation commonly have limestone and calcareous interbeds. This unit represents a distal marine environment, following a regional marine transgressive event, during which all structural highs and platform areas in the region became submerged.

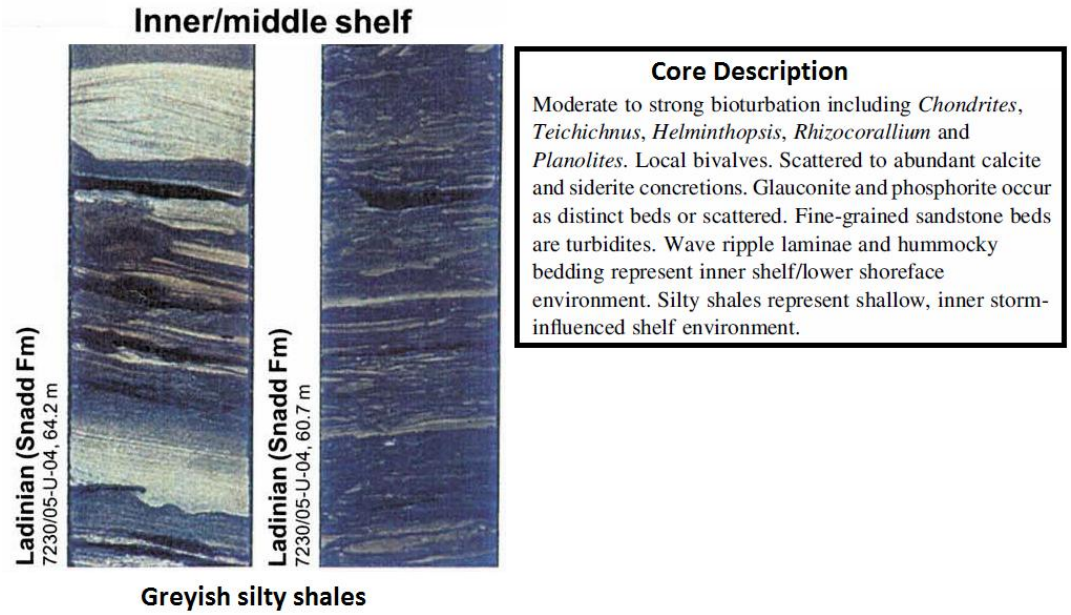

Fig. 2.8 Core description of the Snadd Formation (adapted from Bugge et al., 2002).

- **Kobbe Formation;** this formation belongs to the Sassendalen Group and consists of a thick basal shale unit grading upward into interbedded shale, siltstone and carbonate cemented sandstone (Figure 2.9). A coarser proximal facies development is typical of this unit along the Southern margin of the Hammerfest Basin. This formation thickens on the Troms-Finnmark platform, and is of Anisian age. A transgressive pulse marks the base of this formation following a renewed clastic marginal marine regime from the southern coastal areas.

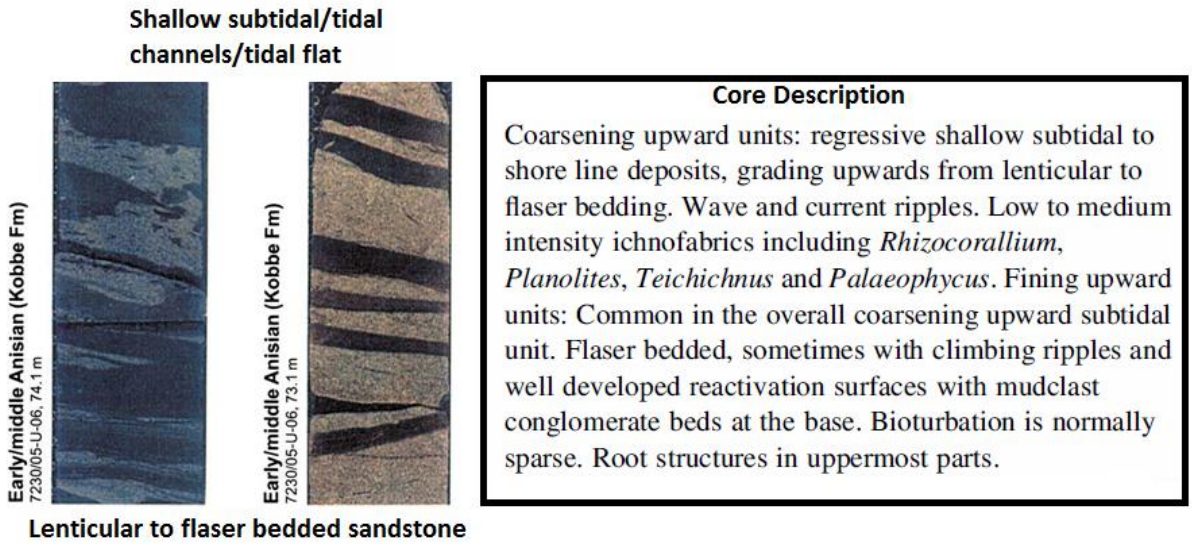

Fig. 2.9 Core description of the Kobbe Formation (adapted from Bugge et al., 2002).

- **Klappmyss Formation;** this formation belongs to the Sassendalen Group. This formation shows a typical coarsening upward succession with medium to dark grey shales at the base followed by interbedded shales, siltstones and sandstones. Its age has been suggested to be Smithian to Spathian and it tends to thicken and fine northwards from the Southern margins of the Hammerfest Basin. This unit was deposited in a marginal to open marine environment with some renewed northwards coastal progradation from the early Smithian transgression.

2.3.1 Trap

The major structural element cutting through the Goliat Field is the Troms-Finnmark Fault Complex (TFFC), which is an old zone of weakness. This fault complex is characterized by listric normal faults and associated hanging-wall roll-over anticlines and antithetic faults (Faleide et al., 1984, Gabrielsen et al., 1990, Dore, 1995). This fault complex has been reactivated several times up to Eocene times. The Goliat and Nucula oil discoveries are located on roll over structures fairly close to the TFFC (Figure 2.10). As described by Ohm and Karlsen (2008), most cap rocks located towards the basin flanks are usually thinner, more faulted and contain more silt compared to the same cap rock close to the basin center. As a result, the sealing capacity of cap rocks closer to the periphery of the basin, is generally poorer than those found close to the basin axis. As a consequence, partly leaking cap rocks most likely found in the periphery of the basin would most likely contain oil, after leaking off accumulating gas. This is typical of Sales type II or III traps and may explain the predominance of oil over gas in the Goliat field. There exists a correlation between the expected hydrocarbon phase and the cap-rock quality in the traps (Ohm and Karlsen, 2008).

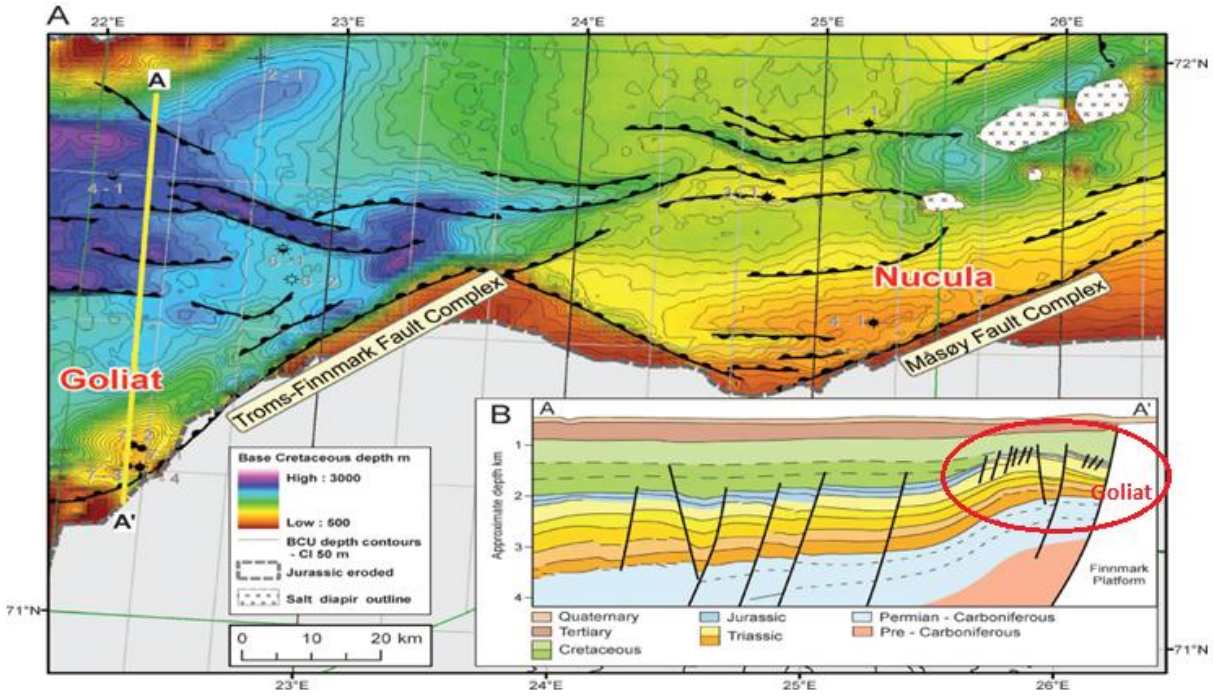

Fig. 2.10 Base cretaceous unconformity depth structure map. Seismic profile shows thinner and more faulted cap rocks (Jurassic and Cretaceous), in the Goliat area than farther out in the basin (modified from Ohm and Karlsen, 2008).

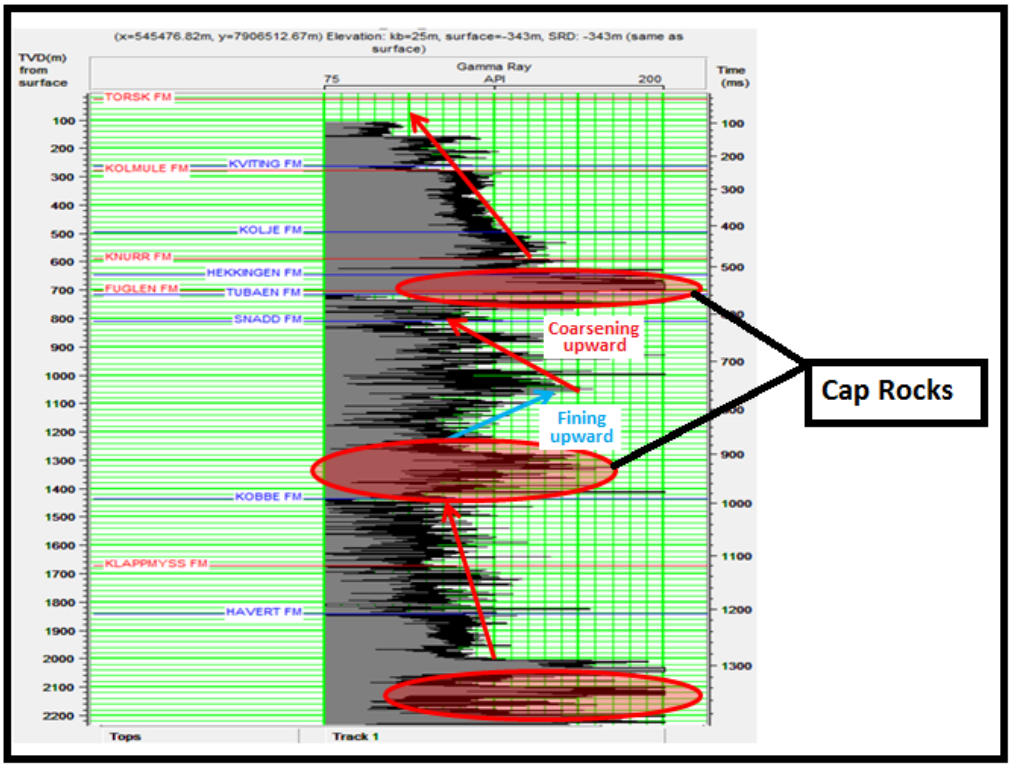

Fig. 2.11 Gamma ray log (API) for well 7122/7-3 showing some source rock intervals (circled in red) including cap rock horizons. Upward coarsening and fining sequences are shown with arrows.

The two main cap rocks of interest in this study are represented by the Fuglen Formation and the base of the Snadd Formation as highlighted in Figure 2.11. The Fuglen cap rock is a relatively tight cap rock and acts as a good seal, retaining a small gas cap in the Tubåen Formation after uplift. On the other hand the deeper cap rock (base of the Snadd Formation), has a relatively poor seal. Based on the gamma ray log, it is seen to be relatively coarser than the Fuglen Formation and is representative of a Sales type II / III trap. Several fill and subsequent spill scenarios may occur during Tertiary migration of hydrocarbons from existing traps in an uplifted sedimentary basin. After uplift the pressure reduction will causes any existing super critical petroleum phase (if present), to exsolve out some gas and form a two phase fraction of oil and gas. Good seals (tight cap rock), have a higher probability to retain gas as illustrated in Figure 2.12.

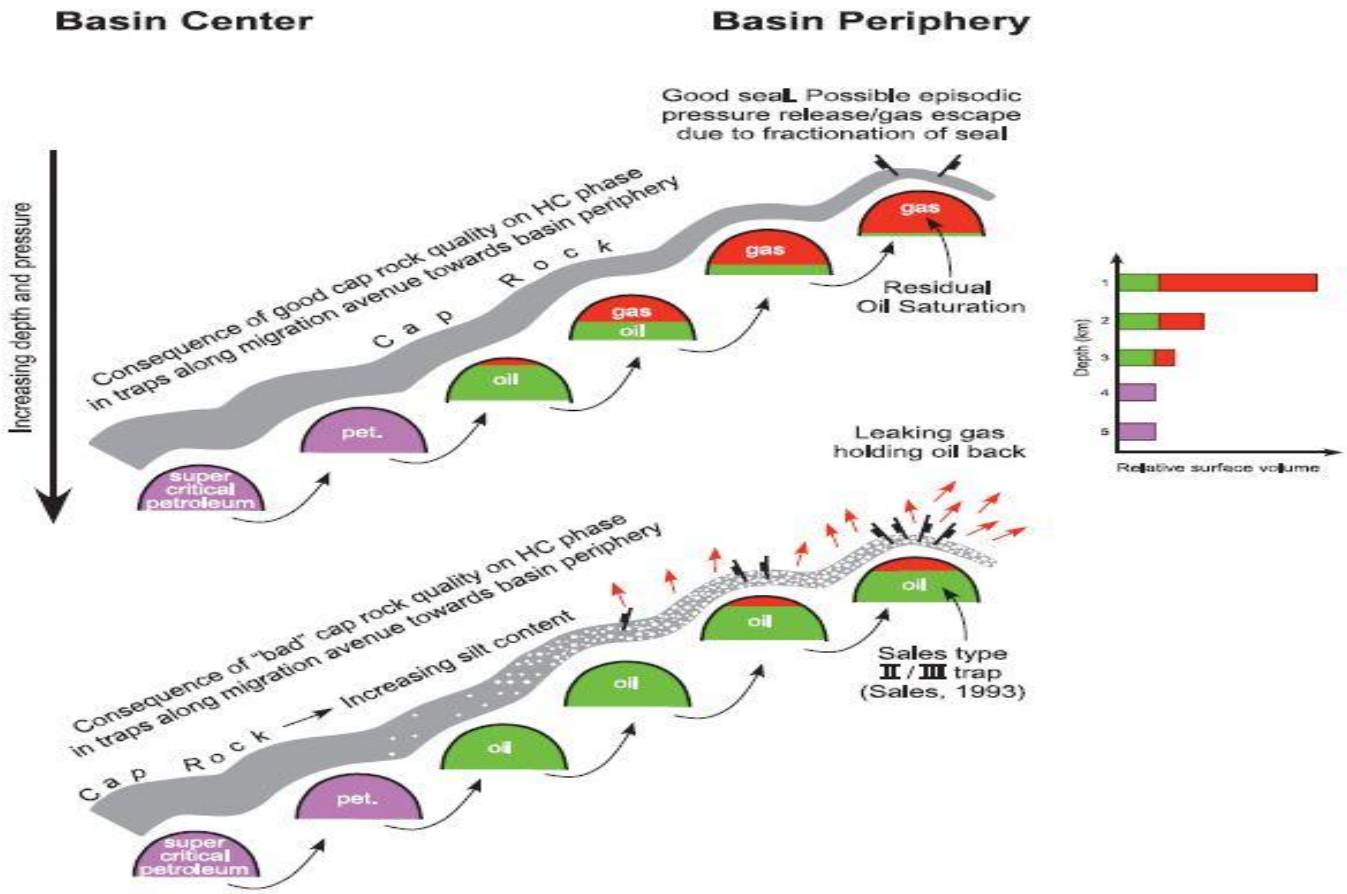

Fig. 2.12 Correlation between hydrocarbon phase and cap-rock quality (adapted from Ohm and Karlsen, 2008).

2.4 Exploration challenges on the Barents shelf

There are several factors (e.g. geological and commercial) that need to be taken into consideration when exploring for hydrocarbons on the Barents shelf. A number of these factors summarized in this study have been described in Dore (1995). The Barents Sea is relatively immature with respect to hydrocarbon exploration, when compared to areas like the Northern North Sea. Some of these challenges include;

- Cenozoic exhumation is the primary geologic consideration which renders hydrocarbon exploration challenging on the Barents shelf. Residual columns of oil have been found beneath several gas finds indicating that the structures were initially or partly filled with oil in the past (Dore, 1995). In terms of the source rocks, cooling as a result of uplift would have caused mature source intervals to stop generating more hydrocarbons. With respect to reservoir rocks, they are of a lower quality than expected at a given depth, because they are overconsolidated. Seal breaching and resultant spilling of hydrocarbon accumulations from traps also occurred as a result of uplift. The pressure release and subsequent expansion of gas adds the number of variables involved in redistribution of the oil to distant traps which would have otherwise not been charged (Ohm and Karlsen, 2008).

- Other commercial considerations involved in hydrocarbon exploration in the Barents shelf, have to do with the distance to potential markets. Harsh arctic climate, remoteness of the area and the need for environmental precautions also adds constraints to exploration in this area. Water depths here are averagely 300m deeper than most oil fields in the North sea (Dore, 1995), and therefore need more technologically advanced solutions for development ,such as subsea installations or floating production systems. Oil finds are commercially more desirable. The predominance of gas over oil needs additional processing facilities, to convert the gas to liquefied natural gas (LNG) before being easily transported through long distance pipelines. All these factors decrease the economic feasibility of hydrocarbon exploration.

CHAPTER 3 COMPACTION AND ROCK PROPERTIES

3.1 Introduction

Sedimentary basins usually go through a continuous cycle of creation and infill of accommodation space. The infill usually takes place layer after layer, and results in a stratified basin infill. The physical and chemical properties of these sediments change significantly with increasing burial depth, from loose sediments to consolidated rocks. The grain fabric undergoes an insignificant reduction in volume so that the increase in bulk density with burial is linked to a reduction in pore volume. This reduction in the bulk sediment volume (porosity loss), and resultant increase in bulk density as a function of burial is generally referred to as compaction. Sediment compaction is driven towards higher density (lower porosity) by mechanical compaction following the laws of rock and soil mechanics and by chemical compaction controlled by thermodynamics and kinetics independent of the stress (Bjørlykke and Jahren, 2010). Log derived rock properties such as velocity, porosity and bulk density, change as a function of both mechanical (effective stress) and chemical compaction (mineral thermodynamics and kinetics). These rock properties are closely related to each other and change in a predictable pattern with increasing amount of compaction. Compaction induced changes in these petrophysical rock properties, provide insight into the nature of, and transition between mechanical and chemical compaction. The prediction of how the above mentioned rock properties vary with depth is vital for input in seismic interpretation, depth conversions, modeling and exhumation characterization (Marcussen et al., 2009).

This chapter will provide a brief theoretical framework as a base for subsequent discussions. A description of the data methodology used to is also presented and the results subsequently explained in the discussion.

3.2 Theoretical Background

3.2.1 Mechanical Compaction

Mechanical compaction starts immediately after sediment deposition, as the subsequent overburden increases. In most sedimentary basins mechanical compaction due to increased effective stress controls the changing rock petrophysical properties down to temperatures

between 70-80^{0}C. The effective stress (which represents the difference between the total stress and the pore pressure), determines the extent of mechanical compaction. This effective stress is transmitted through the grain framework and will be concentrated on the (largest) grains, which experience a grain – to – grain contact stress higher than the overall average effective stress. This eventually leads to grain reorientation and grain crushing, and the rock becomes less compressible. Data from the shallow parts of the sedimentary basin dominated by mechanical compaction show good agreement with experimental compaction data and can be used to predict reservoir properties at depths corresponding to temperatures less than 70 – 80 ^{0}C, before the onset of chemical compaction (Marcussen et al., 2010).

Several factors influencing mechanical compaction such as mineralogy, sorting, grain size, and shape (Figure 3.1), are closely linked to the provenance, duration and mechanism of transport of the sediments into the sedimentary basin (Mondol et al., 2007, Mondol et al., 2008, Mondol et al., 2009a). Poorly sorted sediments tend to compact readily at relatively lower effective stresses than well sorted sediments, as the finer grained material can adequately fill in the space between the coarse grains (Mondol et al., 2007). Rough grains on the other end limit the amount of mechanical compaction due to grain rearrangement, when compared to smooth, well rounded grains. Larger or coarse grained sediments of the same mineralogy will however experience greater amount of grain crushing during mechanical compaction as these grains feel a higher contact stress than fine grained sediments (Mondol et al., 2009a). As a result of this, smectite rich mud which is fine grained and with a large specific surface area, will compact much less readily than kaolinite rich mud which is coarser and with a smaller specific surface area. The same observation is true for sandstones (Figure 3.2).

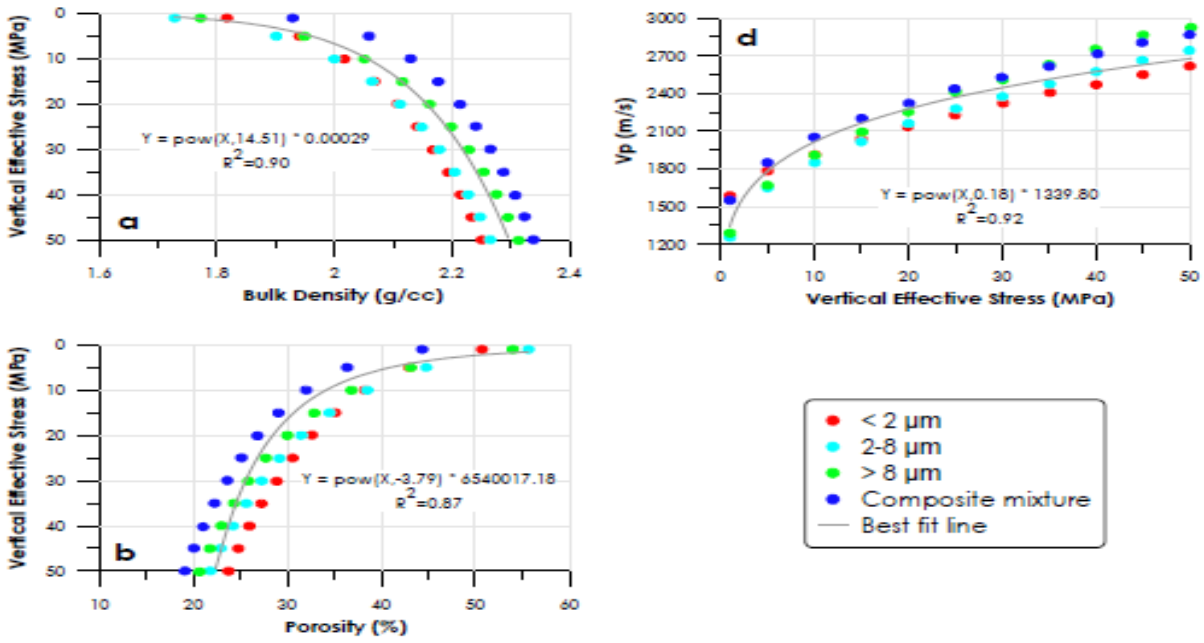

Fig. 3.1 Plots of petrophysical and acoustic properties of brine-saturated kaolinite aggregates as a function of vertical effective stress (adapted from Mondol et al., 2008).

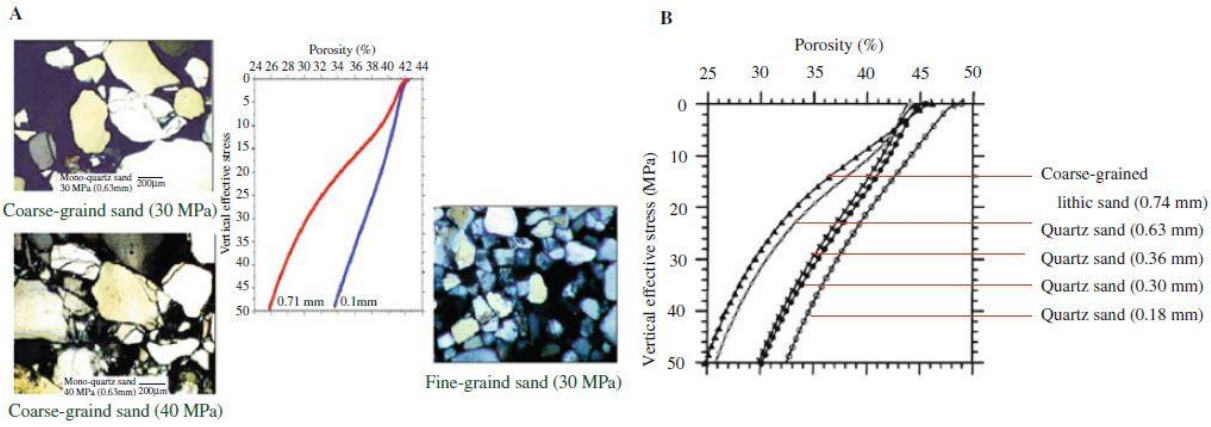

Fig. 3.2 Effect of sand grain size on mechanical compaction with increasing stress (adapted from Bjørlykke and Jahren, 2010).

For the finer grained sediments, the effective stress due to increasing overburden is distributed over larger number of grain contacts and the stress per grain contact is correspondingly lower. The physical properties of mudstones in general will not depend only on geometrical constraints but also on the composition of the pore fluids (Bjørlykke, 2010).

3.2.2 Chemical Compaction

Chemical compaction involves dissolution, precipitation and cementation of the grain framework. Unlike mechanical compaction, chemical compaction is a function of thermodynamics and kinetics (involving a time – temperature integral) during burial. Burial depths corresponding to temperatures higher than 70 – 80 ^{0}C usually corresponds to the transition between mechanical and chemical compaction for siliciclastic rocks. The exact depth range at which this transition occurs varies from basin to basin depending on the geothermal gradient.

Volcanic sediments and sediments containing fossils like diatoms and siliceous sponges tend to be rich in Opal A (amorphous silica) and represent an important source for quartz cement precipitation at a relatively shallower depth compared to the onset of quartz cementation from pure sands and shales (Bjørlykke and Jahren, 2010). Dissolution of fossils rich in Opal A, cause the pore water to be supersaturated with silica relative to quartz and could induce precipitation of micro quartz on clastic quartz grains at relatively low temperatures. This phenomenon is important in preserving porosity with depth. At higher temperatures pore water is only slightly supersaturated with respect to quartz after minerals like smectite, Opal A and Opal CT have reacted. This slight super saturation is not sufficient to precipitate quartz cement on micro quartz coatings (Aase et al., 1996).

Re-crystallization of calcareous organisms and meteoric flushing of aragonite is an important source for calcite cementation. Aragonite and high Mg calcite represent unstable carbonate mineral phases. Fluvial sands with less biogenic production in fresh water have a lower probability of calcite cement compared to shallow marine sandstones.

Very small amounts of cement will prevent grain rearrangement and significant grain framework stiffening. This will result to an abrupt increase in the observed velocity (Storvoll et al., 2005). The temperature range of 70 – 80 ^{0}C represents the activation energy required for the transformation of thermodynamically unstable smectite to illite via mixed layer minerals. A simplification of this reaction is shown below:

Smectite + K-feldspar = Illite + Silica + H_2O

For this reaction to proceed, the silica released in the process needs to be precipitated as quartz cement. A readily available k^+ source, (such as from the dissolution of k-feldspars), needs to be present.

The formation of stylolites (Figure 3.3) from pressure solution is critical for the destruction of porosity in sandstones and grain framework stiffening (Bjørlykke and Jahren, 2010). Mudstones may survive chemical compaction to greater depths in the absence of the more thermodynamically unstable minerals like smectite.

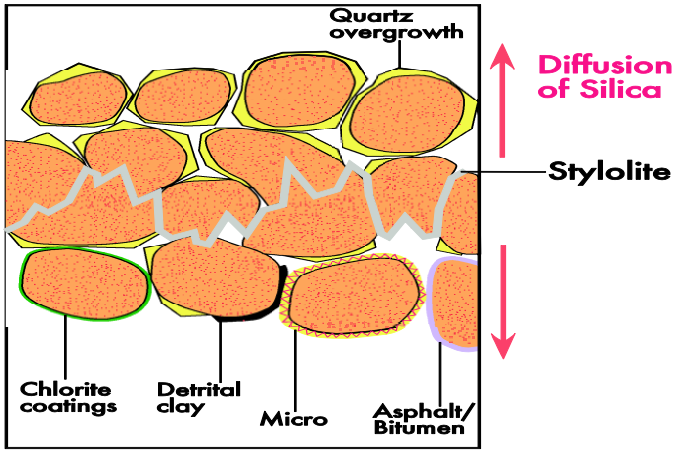

Fig. 3.3 Quartz cement formation in sandstones and grain coatings (Byørlykke and Jahren, 2010).

At higher temperatures of about 130 ^{0}C and in the presence of K-feldspar, kaolinite becomes unstable. It then reacts with K-feldspar, leading to the precipitation of illite and quartz cement. The presence of K^+ ions and removal of the silica from solution is necessary for the forward reaction to be successful. Below is a simplified expression of this reaction:

$$KAlSi_3O_8 + Al_2Si_20_5(OH)_4 = KAl_3Si_3O_{10}(OH)_2 + SiO_2 + 2H_2O$$

K- Feldspar + Kaolinite = Illite + Quartz

The precipitation of quartz cement in either sand or clays has the effect of reducing the porosity and increasing the grain–to-grain contact area. This makes the rock less sensitive to changing effective stresses and inhibits further volumetric loss by mechanical compaction as a result of stabilizing the grain framework. Very low geothermal gradients and fast rates of deposition and subsidence in cold basins will enhance mechanical compaction and grain crushing at even greater depths, unless an overpressure exists to counter the increasing effective stress (Bjørlykke and Jahren, 2010). The volume of quartz cement that can be

precipitated is not only limited by the temperature – time integral but also by the total grain surface available for quartz cement precipitation (Walderhaug, 1994).

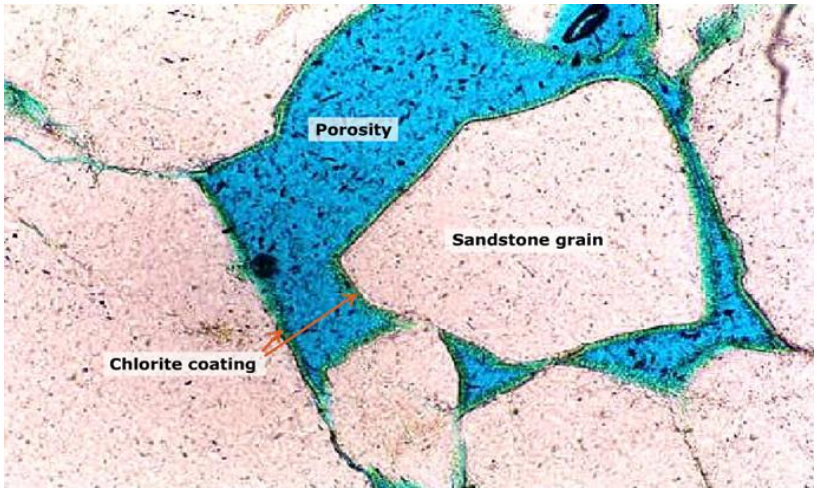

Fig. 3.4 Grain coating by chlorite, well 6506/12-10, depth 5024.50m RKB, Smørbukk Field, Haltenbanken (adapted from Byørlykke and Jahren, 2010).

The presence of grain coatings such as micro quartz, detrital clay, asphalt (bitumen) and chlorite could preserve much of the primary porosity in deep seated reservoirs (Figure 3.4). Quartz cementation will continue to cement the rock and further reduce the porosity even during uplift (Bjørlykke and Jahren, 2010) as shown in Figure 3.5, provided the temperatures stay above 70 – 80 ^{0}C which represents the minimum activation energy required for the process. A simplification of the temperature controlled nature of this transition is shown in Figure 3.5. When rocks have been subjected to higher effective stresses in their geologic past, due to exhumation and glacial loading, they tend to have greater bulk and shear modulus than corresponding rocks at the same present day burial depth. As a result they are referred to as overconsolidated. Chemical compaction provides rocks with a substantial increase in bulk and shear modulus as a result of grain framework stiffening. This phenomenon on the other hand is referred to as pseudo- over consolidation, because the strength of the rock is not attributable to higher prior effective stresses (Bjørlykke and Jahren, 2010).

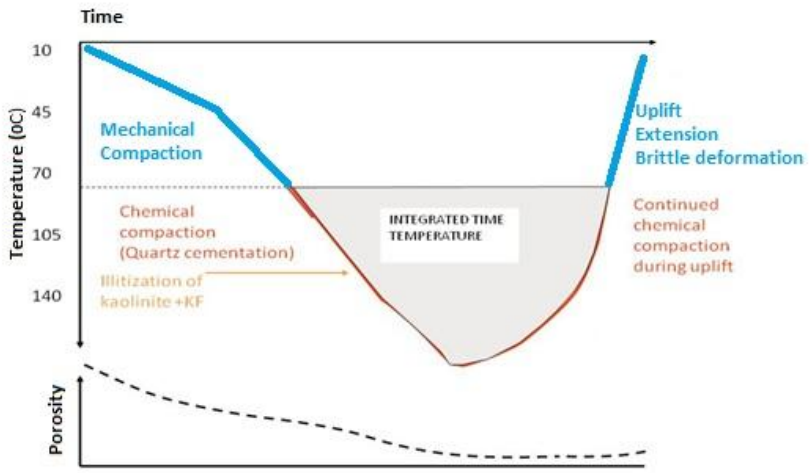

Fig. 3.5 Diagenesis as a function of temperature and time (adapted from Byørlykke and Jahren, 2010).

3.3 Materials and Methods

Overconsolidation of rocks due to uplift and Pseudo overconsolidation due to cementation of the grain framework, gives reservoir rocks greater bulk and shear modulus than they would normally have at the same depth, in the absence of these two factors. The rock properties change and the reservoir quality becomes less than expected. This has consequences for production. However delineating in advance at which target depth the reservoir properties are hampered by cementation, will assist future development of a drilled prospect. Quantifying the amount of uplift will give an idea of the degree of overconsolidation. The pressure release also has consequences as to what extent long distance migration is effective in charging distant traps in the periphery of the basin. The amount of uplift will also help ascertain if 'source kitchen' is located at depths, deep enough to constitute a live petroleum system.

The Vp, density, neutron logs were used to investigate changing rock properties due to compaction as a function of burial depth. The gamma ray log, published regional data and well completion reports have been used as the main lithologic control with depth for the different petrophysical logs under investigation.

Three of the wells (7122/7-1, 7122/7-2, and 7122/7-5A), have a relatively poor and incomplete sonic log coverage for the drilled formations and are not incorporated in further compaction analysis. Two of the wells chosen for further analysis (7122/7-3 and 7122/7-4) have proven hydrocarbon reserves and therefore the velocity-depth trend will be subject to

effects of varying pore-fluid saturation and overpressure effects. The reference well chosen (7122/7-3) has the deepest depth coverage up to the Tempelfjorden Group also has direct recordings of shear wave velocity and used for rock physics AVO modeling for selected reservoir zones (Chapter 4). In all plots, the velocity is given in meters per second and the depths are displayed in meters below sea floor (BSF).

A composite velocity versus depth plot comprising data from the 6 wells, was compared with published data (used as a geophysical reference to investigate exhumation and possible overpressure intervals); a first order linear velocity-depth trend based on Storvoll et al. (2005), a kaolinite–silt curve from experimental laboratory compaction data based on Mondol 2011 (personal communication), and a Cenozoic marine shale velocity-depth trend line based on Japsen (1999). These published trend lines are based mainly on shale data from several wells in North Sea but can equally used to calibrate exhumation estimates from the Barents shelf even though data from the Barents shelf will generally show a higher velocity-depth gradient considering extensive Cenozoic exhumation and subsequent increases in geothermal gradients and thermal exposure of sediments over time leading to a higher probability of extensive quartz cementation.

The marine Cenozoic shale trend published by Japsen (1999), tends to agree more with shales richer in smectite or illite. Meanwhile in estimating the linear trend based on Storvoll et al. (2005), velocity data from carbonates and salts were not included. This linear trend shows a close agreement to data published by Japsen (1999). The Storvoll et al. (2005) linear trend is just a first order approximation, simply represented by equation 3.1;

$$Z = 1.76Vp - 2600 \quad (3.1)$$

Where Z = depth (meters) and Vp = P-wave velocity (meters per second).

The experimental compaction trend of brine-saturated kaolinite–silt (50:50) mixtures was used as a base to estimate the amount of exhumation in the Goliat Field. The choice of the laboratory kaolinite-silt compaction trend rather than end members sand, silt or clay is based on the fact that, mudrock in nature occurs mostly as a composite mixture of sands, silts and clays of varying weight fractions. The shallowest formations (such as Kolmule, Kolje and Knur) in the wells under investigation are rich in shale and silt beds, still in the mechanical compaction regime.

No analytical work on textural and mineralogical compositions has been carried out on the formations mentioned in this study, and the trends described in the well log data are based on published information about group and formation lithology from NPD (Norwegian Petroleum Directorate) website and Worsley (2008). Problems related to depth measurements in this dataset are minimized because all the wells are vertical (except well 7122/7-5A which is a side track from well 7122/7-5) and therefore assumed to correspond closely to the true vertical depth. A more precise variation of velocity with depth is presented in this study as the entire log data sets from six wells have been used without any statistical averaging. This results in the wide data spread observed as a consequence of varying lithology and degree of diagenetic alteration (subsurface heterogeneity).

3.4 Results

3.4.1 General porosity/density/Vp versus depth trends

There is an inherent interdependent relationship between the different log petrophysical properties such as Vp, density and porosity as function of burial depth due to the combined effects of mechanical and chemical compaction. For a given uniform lithology and constant pore fluid and pressure, the density and Vp will increase as a function of burial depth, meanwhile the porosity will correspondingly decrease.

The Vp-depth trends in all the wells generally tend to increase with depth, with exception of some anomalous zones due to varying lithology, pore fluid and possible effects of pore pressure (Figures 3.6 and 3.7). The gamma ray log used here serves as a lithologic control to constrain the variation in Vp, porosity and bulk density with depth. Very high Vp values of approximately 3500 m/s at shallow burial depths of 250 m (BSF) are observed in all the wells except in well 7122/7-1.

It is clear from Figure 3.6 and 3.7 that the transition from mechanical to chemical compaction for silicilastics (excluding the carbonates) tends to occur at similar depths in all the wells, at approximately 600m. The transition defined here is based on the Vp-depth trend, at 600m BSF (extrapolated across the other depth trends) where for the same lithology there is a rapid increase in the Vp response. When correlated with the gamma ray log, it is confirmed that the increase in Vp is not due to a change in lithology. The trend line representing chemical compaction generally shows a smaller change in velocity with depth.

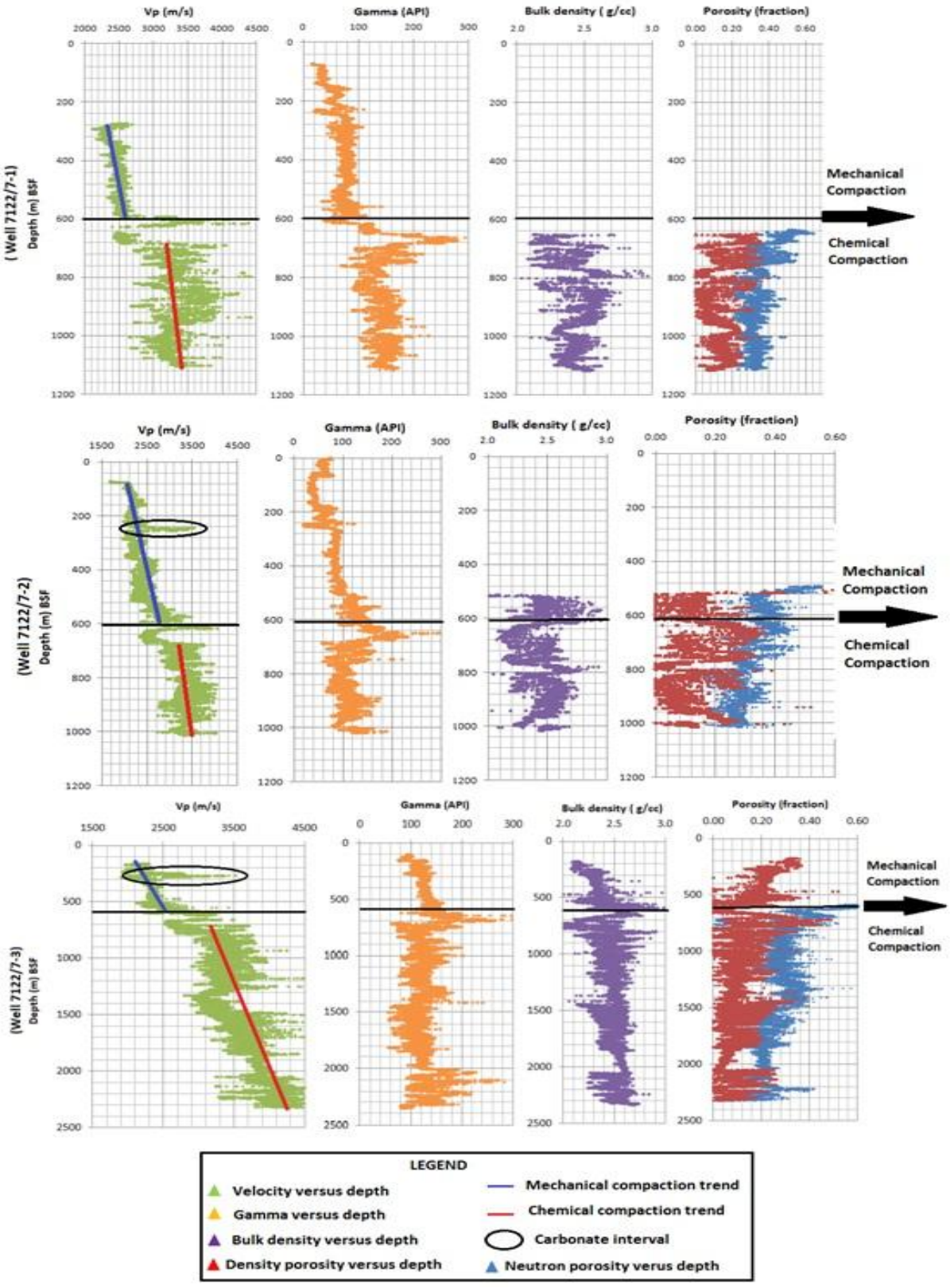

Fig. 3.6 Compaction trends observed in wells 7122/7-1, 7122/7-2 and 7122/7-3.

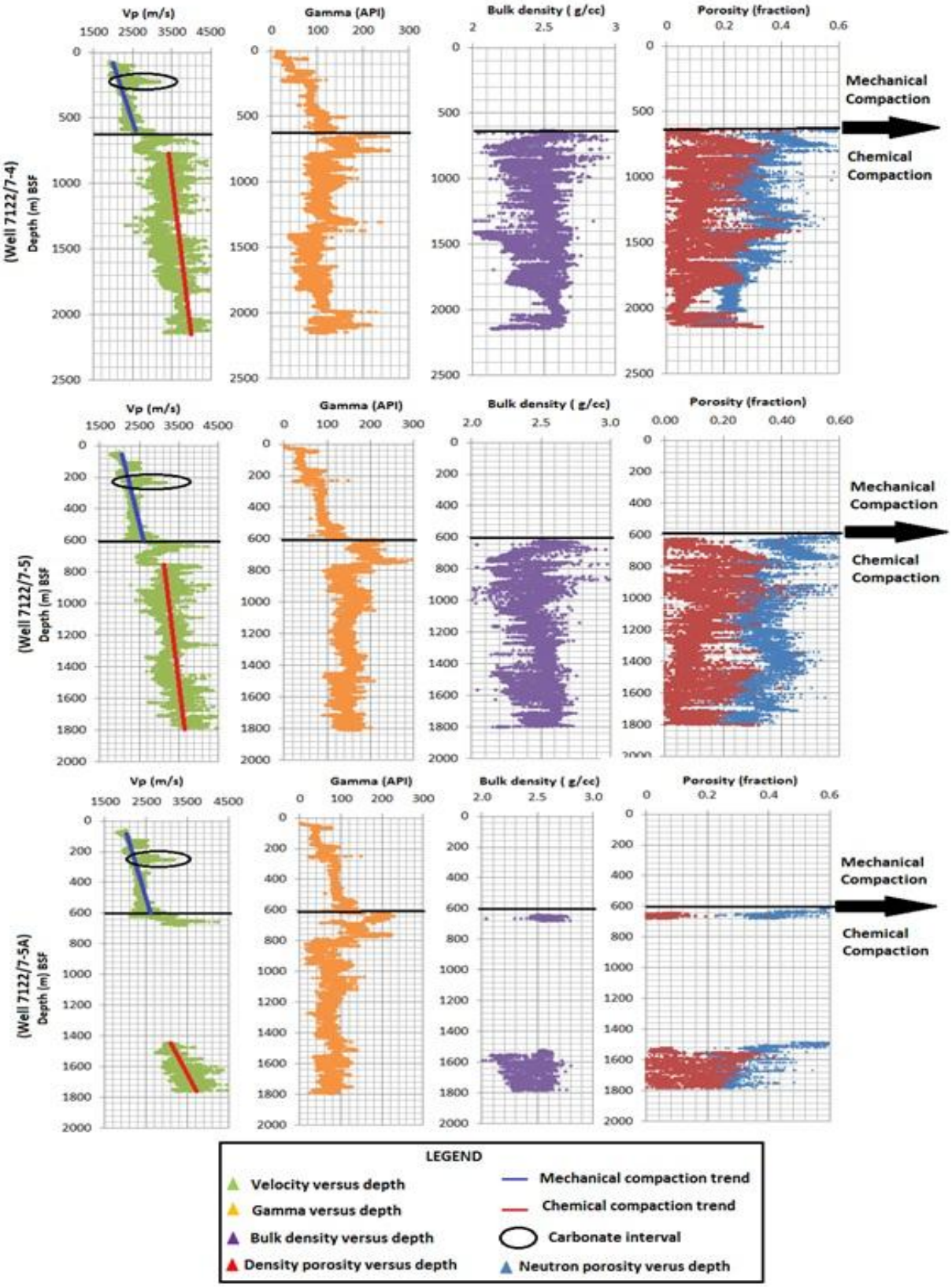

Fig. 3.7 Compaction trends observed in wells 7122/7-4, 7122/7-5 and 7122/7-5A.

Beneath the transition from mechanical to chemical compaction, there is a decrease in observed Vp with depth in all the wells, and correlates with low bulk densities and high gamma readings at the same depth interval. This corresponds to the major source rock in this area (Hekkingen Formation). Both the neutron and density porosities tend to decrease with depth. The density porosity was calculated using a constant matrix density of 2.65 g/cc which is the matrix density of sandstone. There is therefore a deviation between both porosities in depth intervals with high gamma. Negative density porosities are not shown as they physically represent data points with matrix densities greater than 2.65 g/cc. There is an apparent inverse relationship between the gamma and Vp depth trends in all the wells. Generally the density shows a fairly linear increase with depth. Despite the general increase of density with depth, there are zones showing a decrease in density with depth and these areas correlate with high gamma values such as, at depths of about 700m BSF (Figures 3.6 and 3.7). It is observed that depths with significant changes in the gamma ray log, show corresponding changes in the density, Vp, and porosity depth trends due to a lithologic control on these parameters.

3.4.2 Vp-depth trend for well 7122/7-3

Well 7122/7-3 is chosen as the reference well. This well has the deepest depth coverage, most complete log suits and also direct measurements of shear wave velocities (Vs). The Vp-depth trend in Figure 3.8 shows a general increase in Vp with depth. There is however a break in the Velocity depth gradient with depth at about 600m BSF and is taken to be the transition between the mechanical and chemical compaction for siliciclastic rocks in this well. Two simplified trends (shown as solid red and green lines) can be made for mechanical and chemical compaction as shown in Figure 3.8. The first trend corresponding to mechanical compaction (red) from approximately 150m to 600m BSF shows a lower gradient of 0.85; meanwhile the chemical compaction trend (blue) from approximately 650 m to 2350m has a higher gradient of 1.68 compared to the trend above.

Velocities in the shallowest part of the trend belonging to mechanical compaction are less than 2500 m/s. There is however an exception in zone A. The Zone A located at shallow depths of about 250m BSF shows an abrupt increase in the Vp-depth trend up to 3500 m/s. Zone B, C, and D show a decrease in Vp with depth and deviate from the general trend line (green) for chemical compaction.

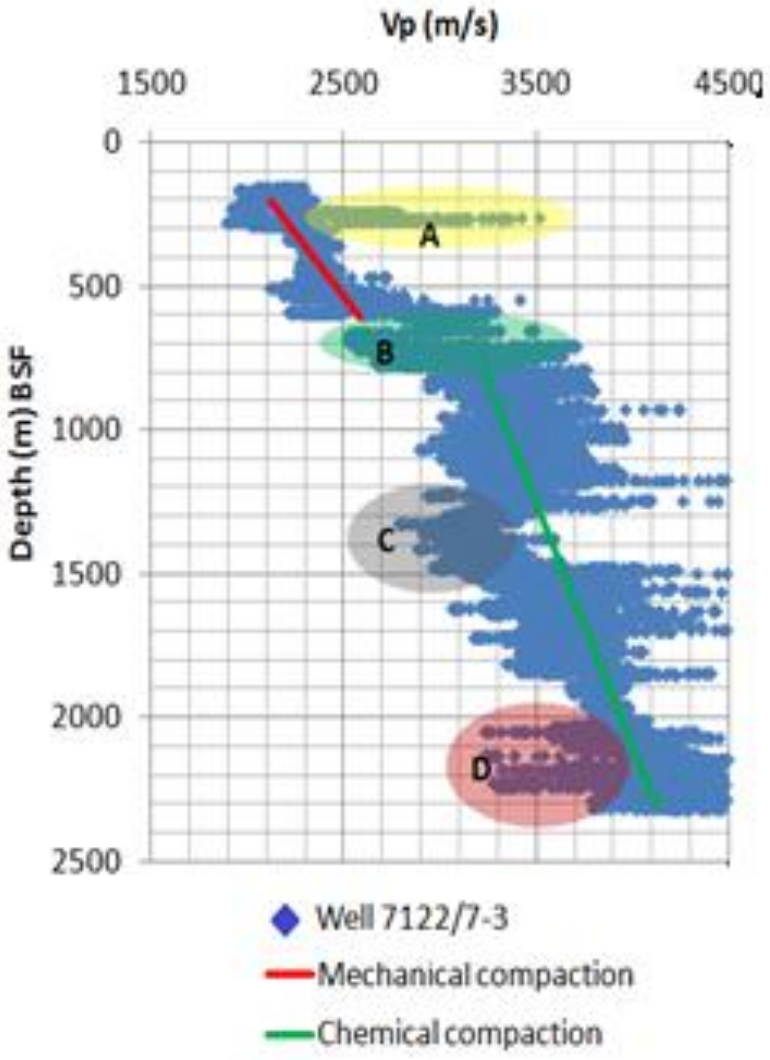

Fig. 3.8 Well 7122/7-3 Vp-depth trend and anomalous zones.

3.4.3 Transition from mechanical to chemical compaction

The transition from mechanical to chemical compaction has been defined based on the Vp-depth trend and a shear modulus-porosity cross plot (Figure 3.9). This transition has been defined based on the sudden sharp increase in Vp for a given lithology at present day depths of approximately 600m below sea floor. The depth at which this transition occurs is seen to occur at similar depths in all the wells as defined in Figure 3.6 and Figure 3.7. The depth at which this transition occurs as defined from the Vp depth trend correlates with the result obtained from the shear modulus/porosity cross plot in Figure 3.9.

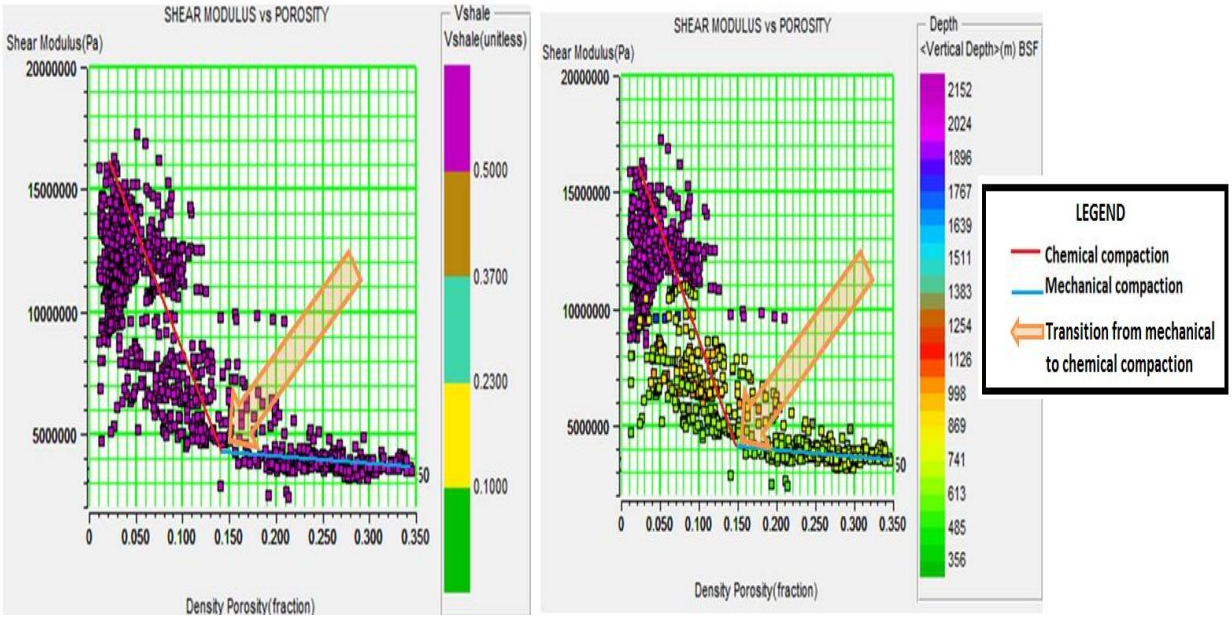

Fig. 3.9 Shear modulus-Porosity cross plot color coded with Vshale and depth.

The shear modulus has been computed using the directly measured shear velocity and bulk density. A cross plot between shear modulus and density porosity (calculated using matrix density of 2.57 g/cc for shales only, in well 7122/7-3 shows a 'knick' point transition from mechanical to chemical compaction. Careful analysis indicates that chemical compaction sets in with approximately 15% porosity left in the shales and at a shear modulus of approximately 5 MPa. The average shear modulus for data points within the mechanical compaction regime is about 4 MPa with a wider range in porosities up to 35%. The entire data set shows a wide range of shear modulus from approximately 3-17 MPa. There is a significant increase in the shear modulus after onset of chemical compaction, and a continuous reduction in porosity. The shear modulus-porosity plot color coded with depth in Figure 3.9 shows the transition from mechanical to chemical compaction ('knick' point) at about 613 m BSF. This closely agrees with the transition obtained using the Vp-depth trend of 600m BSF.

The bottom hole temperature in well 7122/7-3 is 73°C at a true vertical depth of 2725m (NPD Factpages). The sea floor temperatures, based on Coastal Water and North Atlantic Water is >2°C and 3°C respectively (Loeng, 1991). An estimated geothermal gradient can then be made of 29.2^0C/km. This gradient is slightly lower than the actual, because the bottom hole temperatures recorded are less than the true temperatures as the drilling mud tends to cool the down hole assembly during drilling. However geothermal gradients measured from a shallow well on Spitsbergen-banken are slightly higher at 31°C/km (Solheim and Elverhoi, 1993).

The transition from mechanical to chemical occurs at approximately 1.3 km (after applying a 700m correction for uplift in Figure 3.12). This depth corresponds approximately to temperatures of 41°C using a geothermal gradient of 31°C/km.

3.3.4 Uplift estimation

Only sorted shale data has been used for uplift estimation. Figure 3.10 shows a composite plot comprising of shales only from selected wells with sufficient coverage. When compared with experimental compaction curves of Kaolinite – silt (50:50) and the pure Kaolinite trends, there is a significant mismatch between the published trends and the composite Vp-depth profile. This mismatch is seen even for the mechanical compaction regime. This deviation is greater for the chemical compaction regime. An even greater deviation is seen for the trend lines proposed by Japsen (1999) and Storvoll et al. (2005). This observation could be interpreted as the overconsolidation of the shales in this area due to uplift. It is therefore important to quantify this exhumation (uplift and erosion) as it has consequences on the petroleum system in the Goliat field.

The data presented has been sorted based the volume of shale (Vshale>80%). The composite shale trend shown in Figure 3.10 displays mainly data points corresponding to well 7122/7-3 in the mechanical compaction domain, and as a result further exhumation estimates are based on this well only.

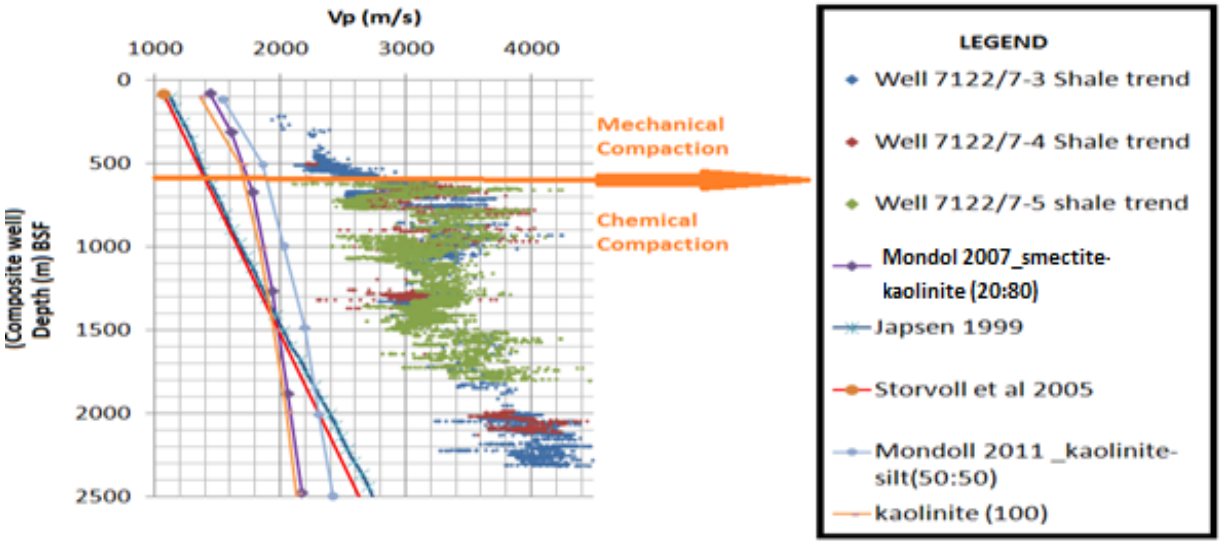

Fig. 3.10 Composite shale trend compared with clay –clay and clay –silt curves.

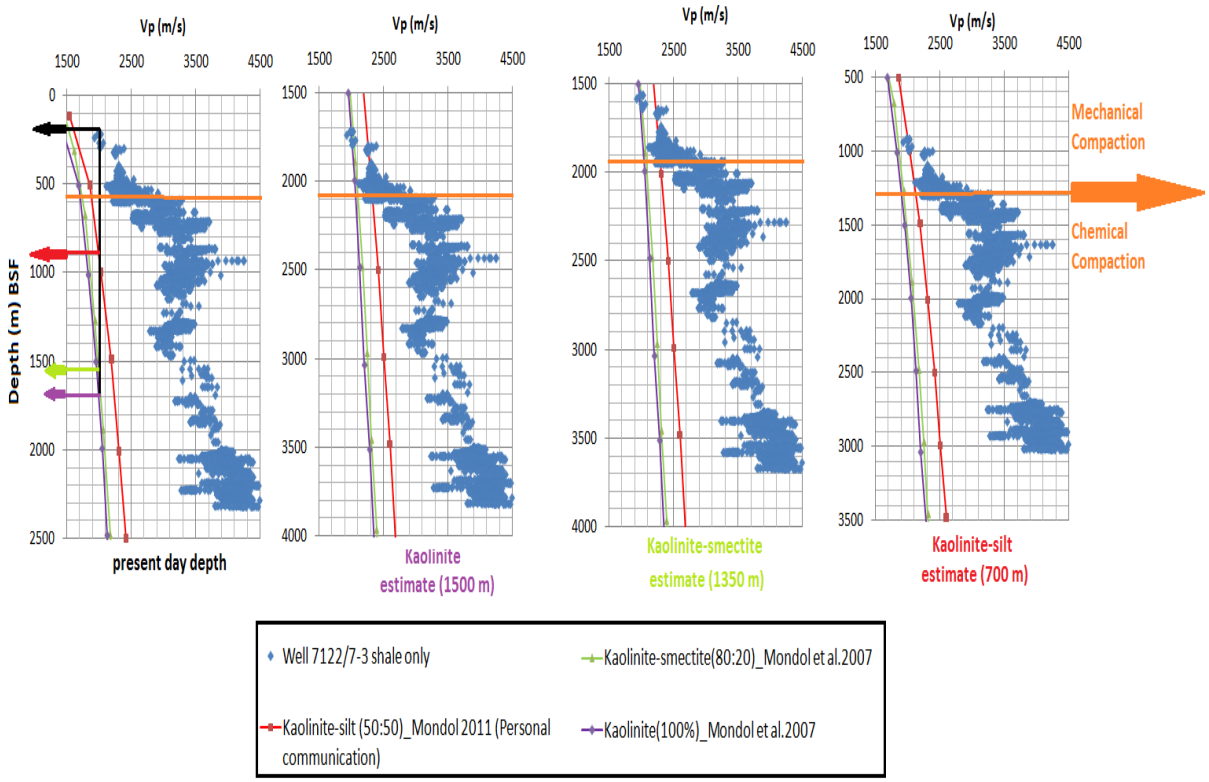

Fig. 3.11 Exhumation estimates using clay –clay and clay –silt curves.

Different estimates for exhumation were obtained by extrapolating data points (well above the transition into chemical compaction) onto the different experimental laboratory compaction curves as shown in Figure 3.11. The largest exhumation estimates of 1500m were observed using the pure kaolinite curve, meanwhile the kaolinite – silt curve resulted to a minimum estimates of 700m, which is almost half that obtained from the pure kaolinite curve. The kaolinite – smectite estimates are much closer to the kaolinite estimates.

The Vp-depth profile for well 7122/7-3 shown in Figure 3.12 (after correction for exhumation based on the kaolinite – silt compaction curve in Figure 3.11), illustrates that, the part of the curve belonging to mechanical compaction (blue) shows a better fit to the Kaolinite – silt trend compared to the first order linear velocity trend and the Cenozoic marine shale trend. The shale trend by (Japsen, 1999) shows a relatively close fit only to shallowest Torsk Formation of the Sotbakken Group deposited during the opening of the Norwegian – Greenland sea.

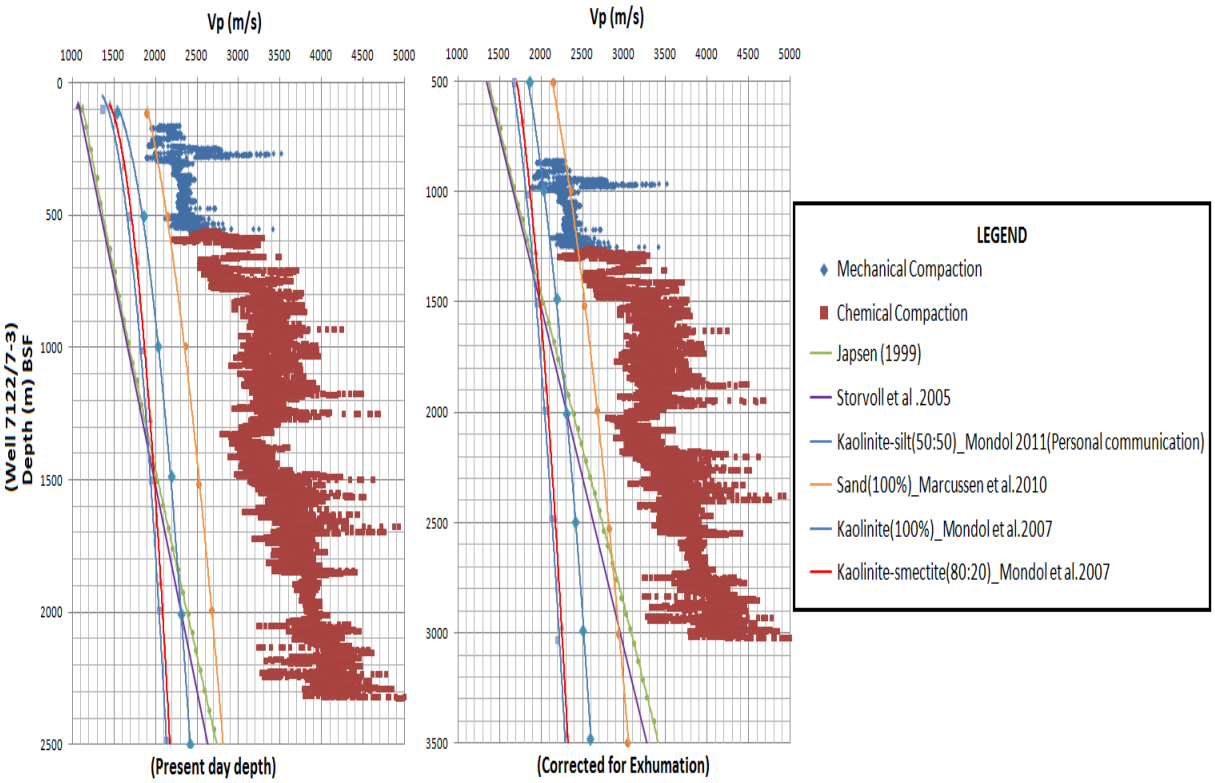

Fig. 3.12 Well 7122/7-3 Vp-depth trend before and after exhumation showing transition from mechanical to chemical compaction.

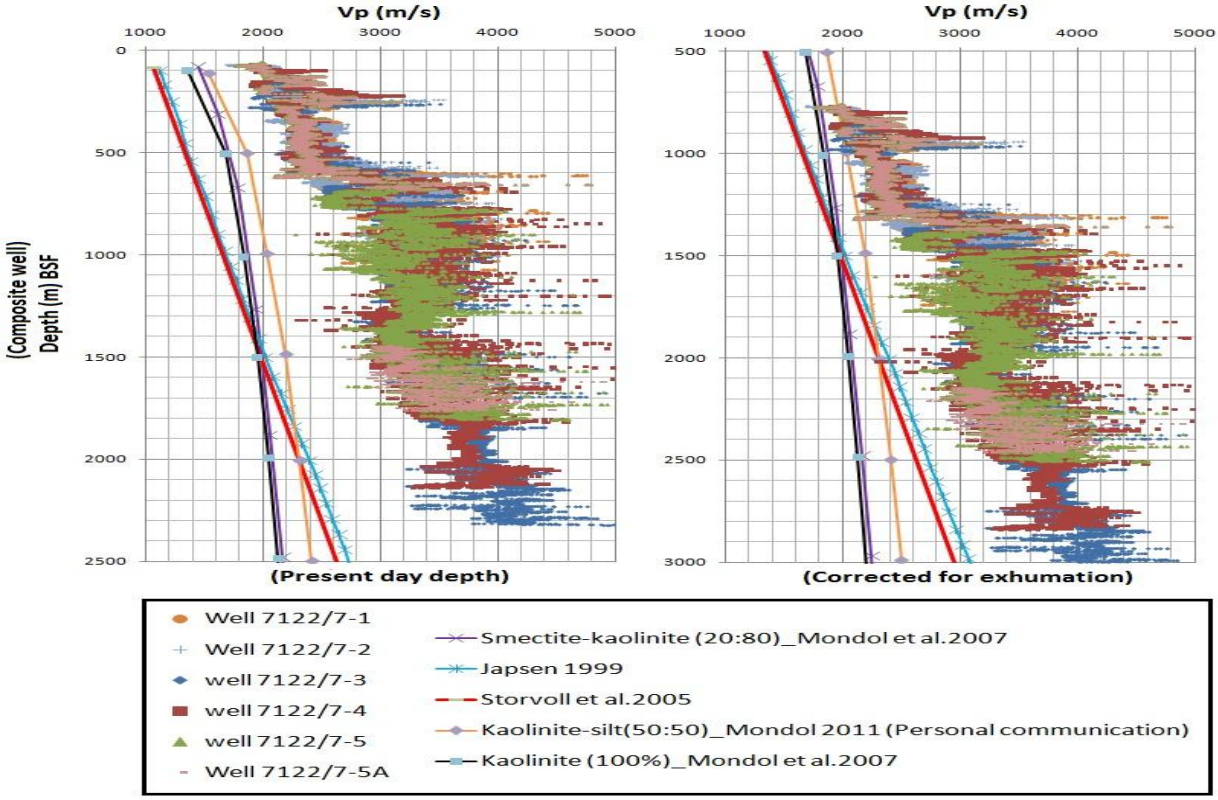

Fig. 3.13 Complete composite well data before and after exhumation.

The composite Vp-depth plot for all six wells in Figure 3.13 shows a closer match to experimental compaction clay data after applying 700m correction for uplift derived from the kaolinite – silt (50:50) curve.

3.4.5 Sand and shale compaction trends

The sand and shale trends for well 7122/7-3 have been sorted out based on Vshale, computed from the gamma ray log in the same well. Both sand and shale trends shown in Figure 3.14 are in the zone corresponding to chemical compaction. The blue straight line connector represents the mechanical compaction regime. Data points within the mechanical compaction regime are composed dominantly of silts, based on Vshale color code. The shale trend illustrated shows a smaller change of velocity with depth compared to both sand trends. The grey interval represents zone C defined in Figure 3.8.

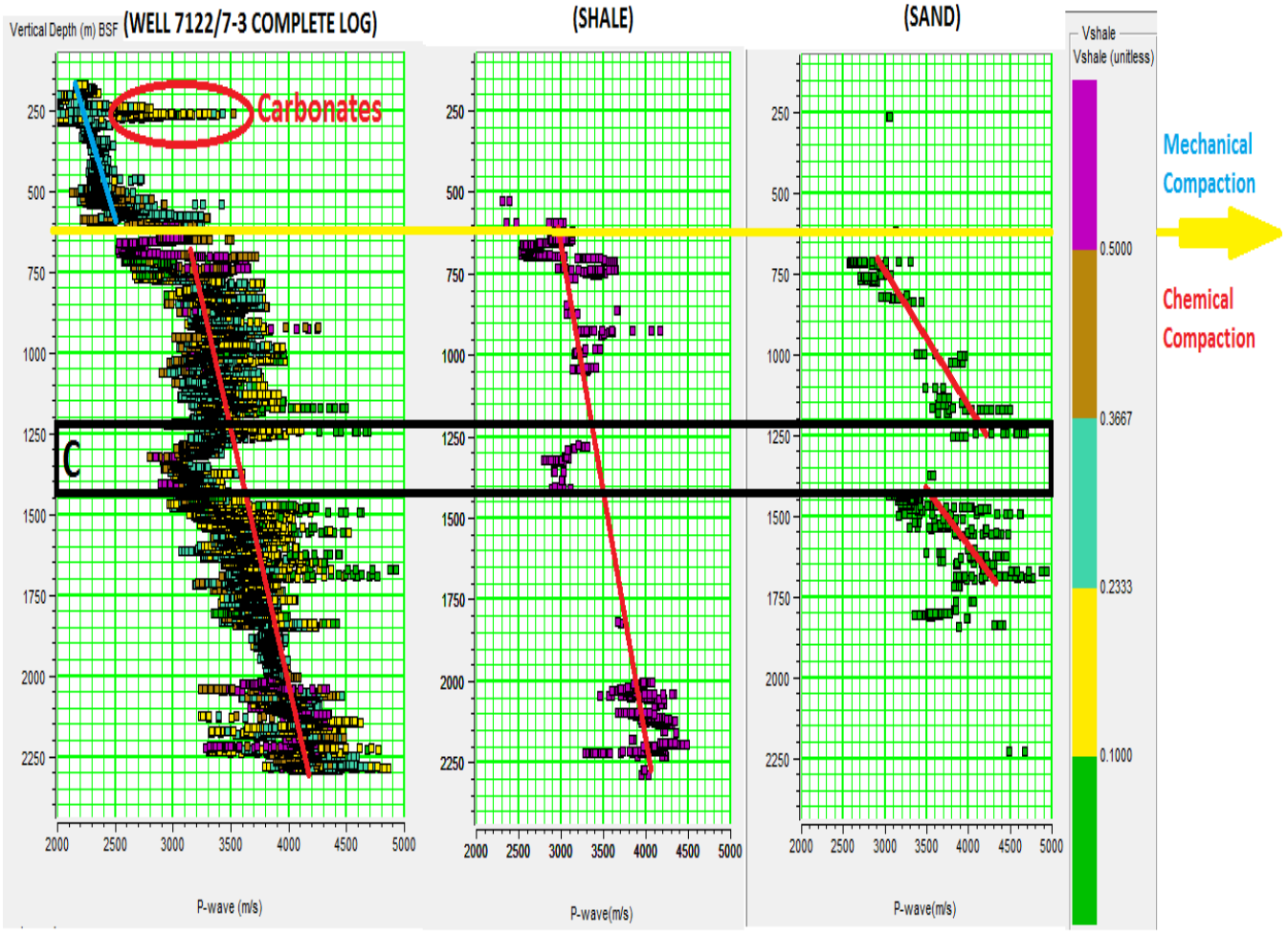

Fig. 3.14 Variations in sand and shale compaction trends.

Zone C shows a lower shale velocity anomalous to the general shale trend line in red. Both sand trends have similar gradients and are separated by the thick shale unit with a lower velocity in Zone C. The beginnings of both sand trends correspond to the Tubåen and Kobbe reservoir units respectively.

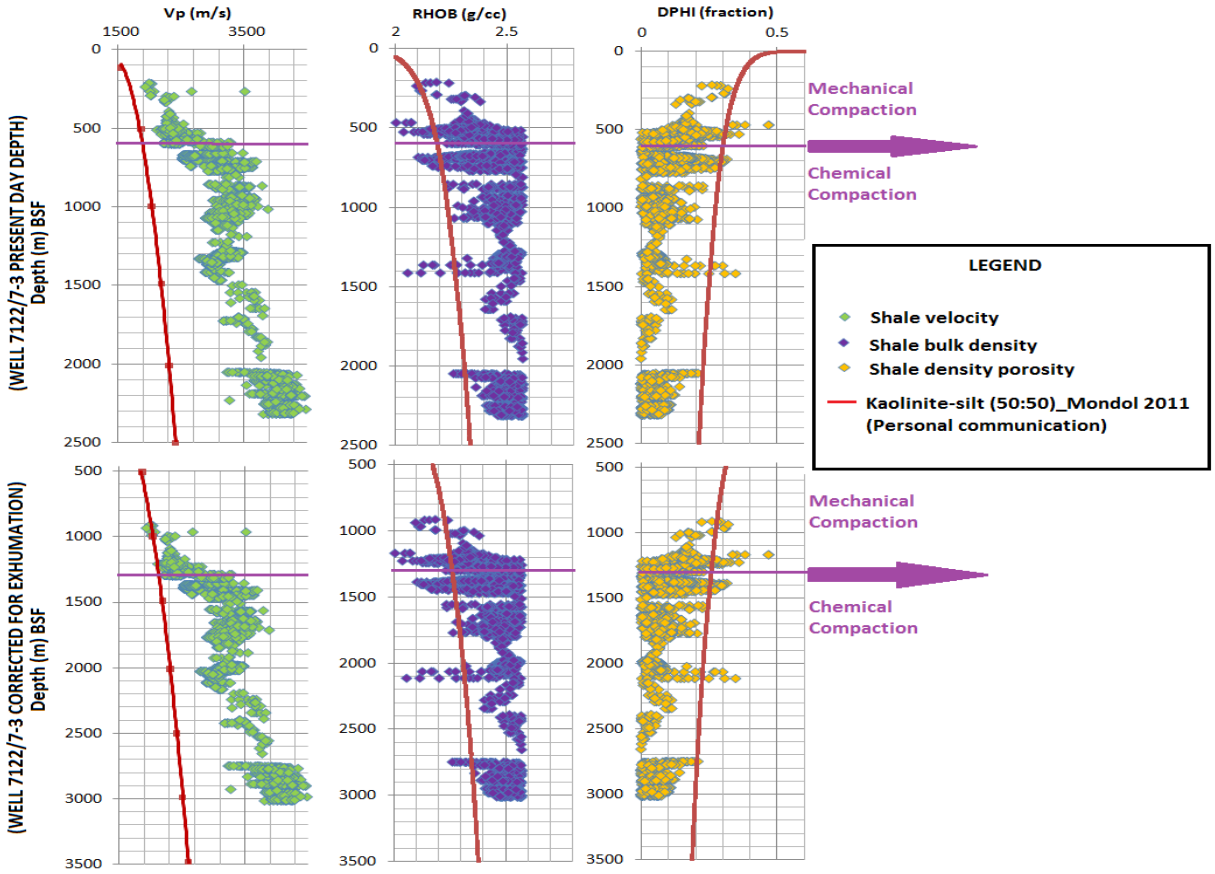

Fig. 3.15 Shale Vp/bulk density/porosity-depth trends.

The data points shown in Figure 3.15 represent shale data points only in well 7122/7-3 selcted based on Vshale > 80%. A bulk density of 2.57 g/cc was then used to compute the density porosity (DPHI). The density and Vp tend to increase with depth meanwhile the density porosity shows an inverse relationship. All three parameters are intricatley linked and predictably vary with depth as a function of burial diagensis. Data points from all three Vp/ bulk density/ porosity depth trends above the transition from mechanical to chemical compaction, deviate from experimental compaction kaolinite – silt (50:50) curve (Mondol 2011, personal communication). This is due to exhumation, as demonstrated in the

corresponding plots beneath showing a much closer fit to experimental laboratory compaction data after applying a correction of 700m upflit to the data.

3.3.6 Effect of pore fluid and pore pressure

Most of the shales represented in Figure 3.16 are already in the chemical compaction regime. The Kobbe oil reservoir is shown in the grey circled zone at approximately 2600m BSF after correcting for exhumation. This demonstrates clearly the effect of varying pore fluid type on the Vp-depth profile in well 7122/7-3. The shale trend shown in red in well 7122/7-3 shows clearly an anormalously low Vp. The grey straight line connector is an approximate best fit line for the shale trend. Meanwhile the circled grey zone represents a cluster of shales which show possible overpressure effects. This circled cluster of shales is the same as zone C in Figure 3.8.

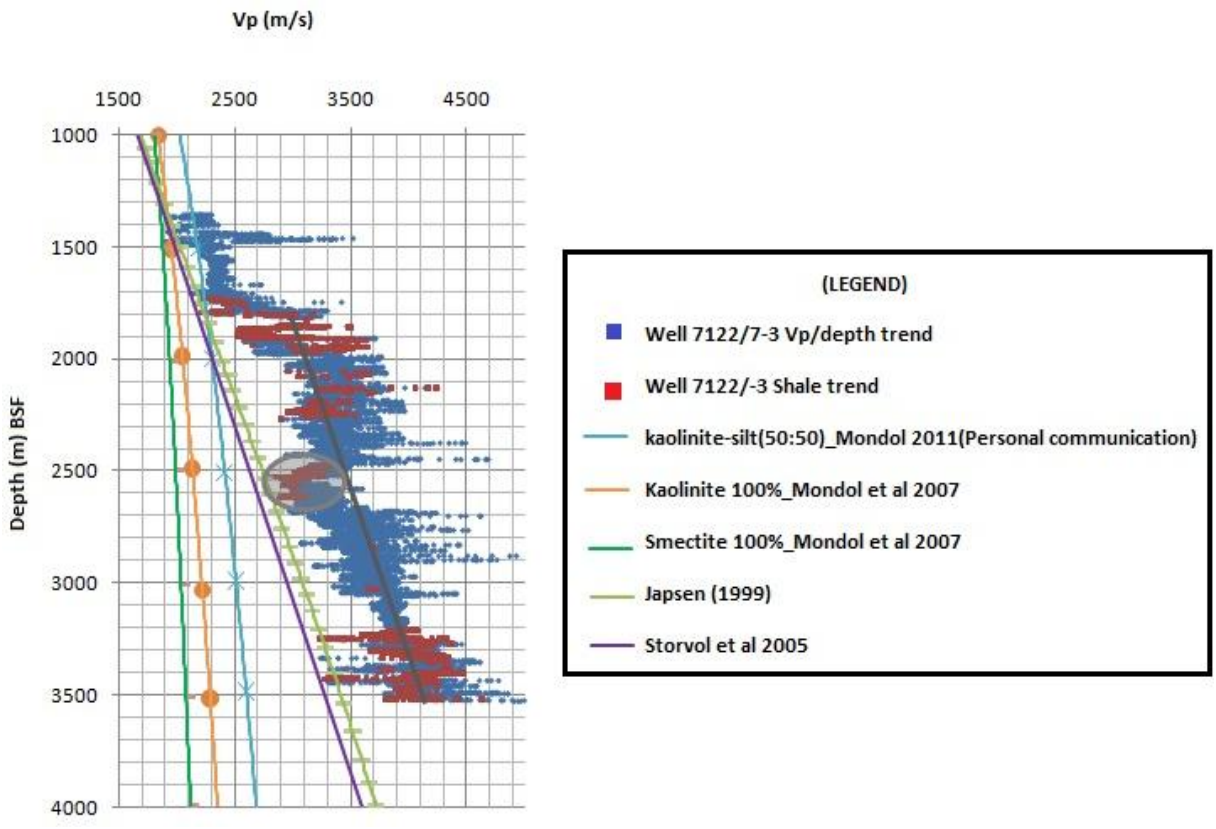

Fig. 3.16 Well 7122/7-3 showing possible overpressure effects.

The smectite curve shows the lower bound while the kaolinite – silt curve represents the upper bound for the experimental data. The shales deviate to higher Vp values away from

the upper bound. The shale trend shows a bettter match to Japsen (1999) and Storvoll et al. (2005), compared to the experimental compaction trends.

3.3.7 Effect of source rock on Vp-depth trend

The major source rock in this area which is also widely distributed throughout the entire Barents Shelf is represented by the marine dominated shales of the Upper Jurassic – Lower Cretaceous Hekkingen Formation. The high kerogen content (Figure. 3.17) is reflected in the high gamma log readings, and low bulk density compared to shales with little or no organic content. The Hekkingen Formation is seen to display a coarsening upward succession with the base of this unit having a significantly higher gamma reading and possibly more organic content. The velocity inversion seen in this interval is also present at similar depths in other wells.

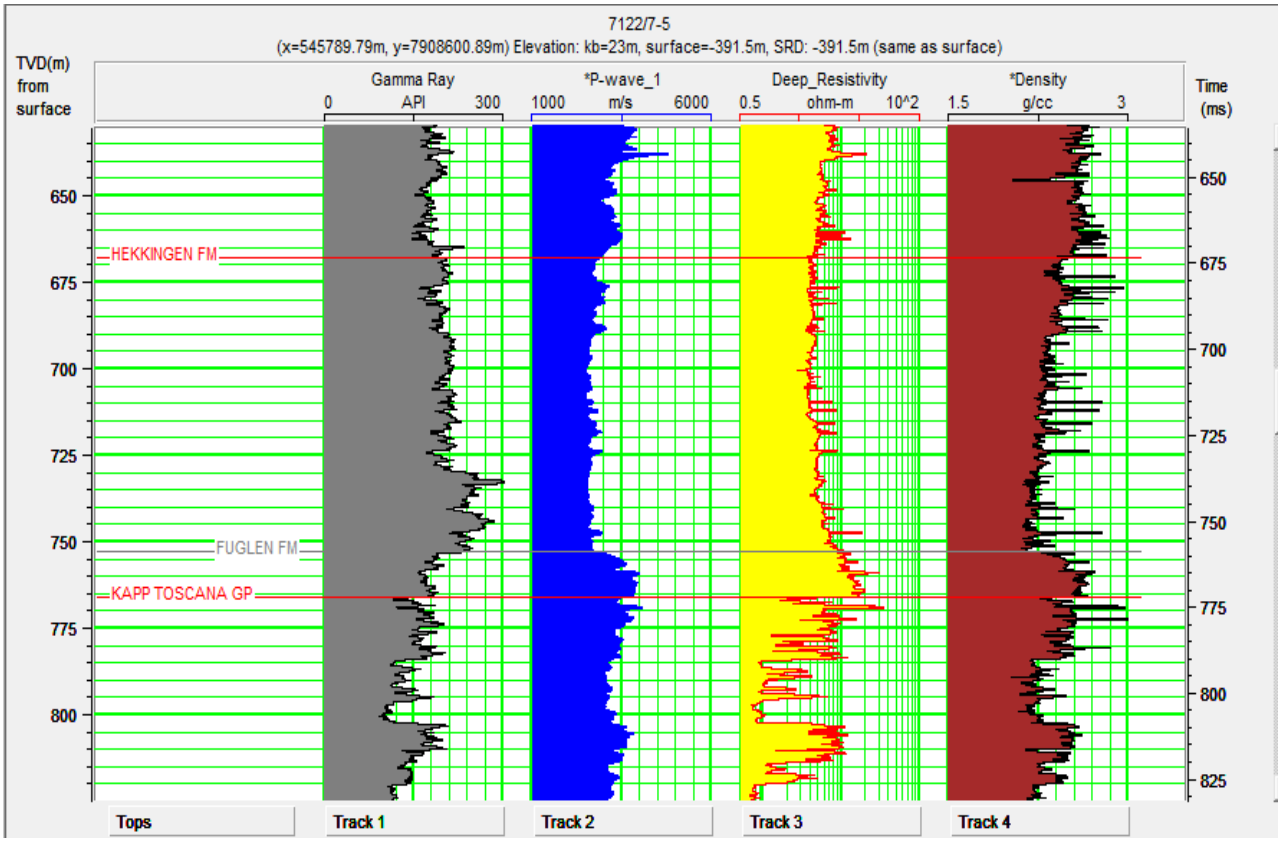

Fig. 3.17 Gamma, Vp, deep resistivity and bulk density petrophysical logs for the source rock interval (Hekkingen formation).

Well 7122/7-5 was selected as the best candidate for the effects of source rocks on Vp, because it is a dry well with no hydrocarbons and only brine. As a result there is no influence from varying pore fluids in the underlying Kapp Toscana Group. The velocity inversion (velocity decreasing with depth) shown in red in Figure 3.18, starts soon after the onset of chemical compaction as shown by the transition with the orange line at present day depths of about 610m BSF up to about 750m BSF. As such Vp-depth variations in this well are assumed to be as a result of varying lithology. The corresponding logs for this interval show very high gamma readings of up to 250 API, and relatively low resistivity less than 75 ohm-m. The Hekkingen Formation is sandwiched between the Fuglen and Knurr Formations and has a bulk density lower than these two, partly due to its high organic content, as shown in the plot in Figure 3.17. Despite the low velocities present in the source rock, it is however still higher than overlying shales of the Kolmule, Kolje and Knurr Formations.

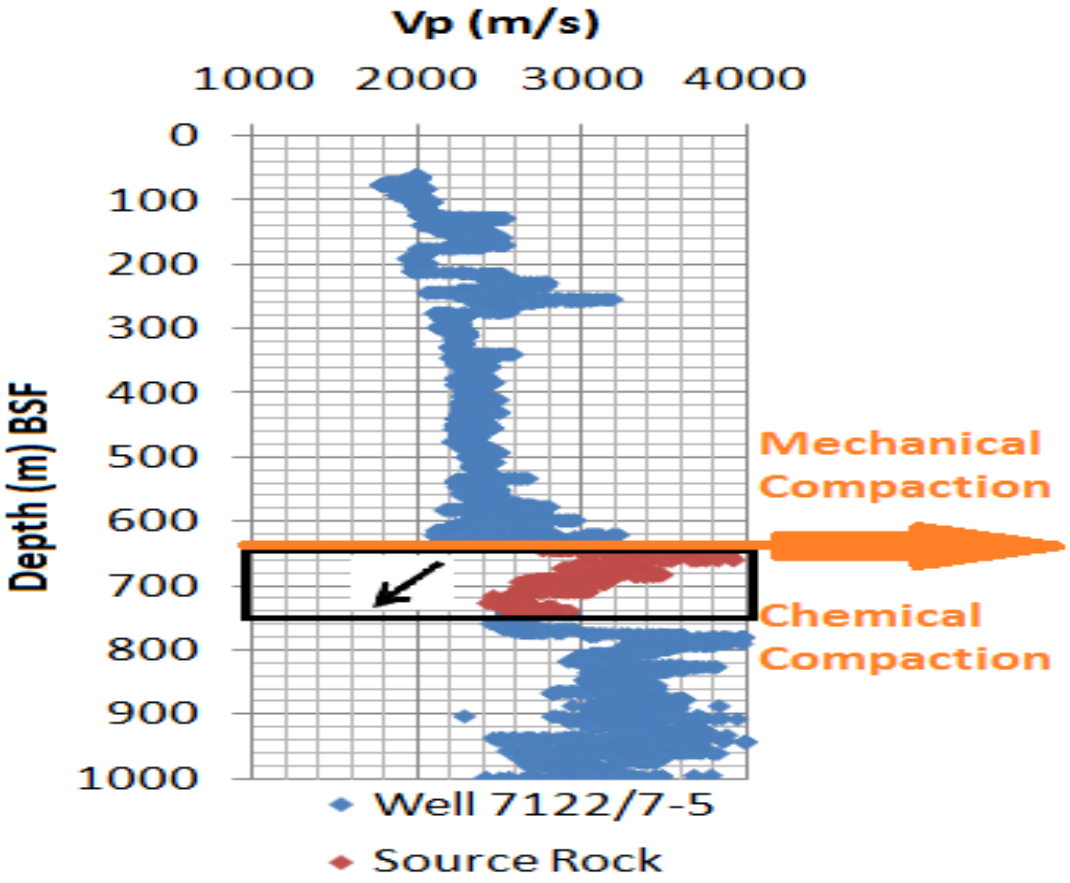

Fig. 3.18 Source rock velocity inversion.

3.4 Discussion

3.4.1 Relationship between porosity/ density/ Vp versus depth trends

There are significant deviations of the composite well data from the Goliat Field compared to the published data. A number of factors can be responsible for this deviation, but separating the independent effects of these factors require of combination of other petrophysical logs such as the density, resistivity and gamma ray curves.

Some of these factors include;

- Lithology variations
- Pore fluid and pore pressure effects
- Transition from mechanical to chemical compaction
- Uplift and erosion (exhumation)

Generally the P-wave velocity (Vp) tends to increase with depth due to corresponding increases in the bulk and shear modulus with depth. The velocity is also inversely proportional to density. Despite the general increase in density with depth as a function of burial and compaction, the velocity still increases because the increase in bulk and shear modulus with depth is greater than the increase of density with depth.

Compaction tends to increase the stiffness, and reduce the porosity (Mondol et al., 2007) in the rock framework through combined effects of increasing effective stress (mechanical compaction) and through dissolution of less stable mineral phases and precipitation of thermodynamically more stable ones (Bjørlykke and Jahren, 2010). The main controls for Velocity however are the porosity and the microfabric (Fawad et al., 2010). The Shallow carbonates (NPD Factpages) stand out with very high Vp of approximately 3500 m/s at very shallow burial depths of 250m BSF. Aragonite and high Mg calcite are unstable carbonate mineral phases and react at much lower temperature and depths compared to common minerals found in siliciclastic rocks. These wells are relatively closely spaced to each other and are therefore expected to have similar geothermal gradients. The trend line representing chemical compaction generally shows a smaller change in Vp with depth, possibly due to increased strength of the rocks due to quartz cementation.

The variation in Vp with depth will further be explained using well 7122/7-3 as a reference as it has the most complete data coverage.

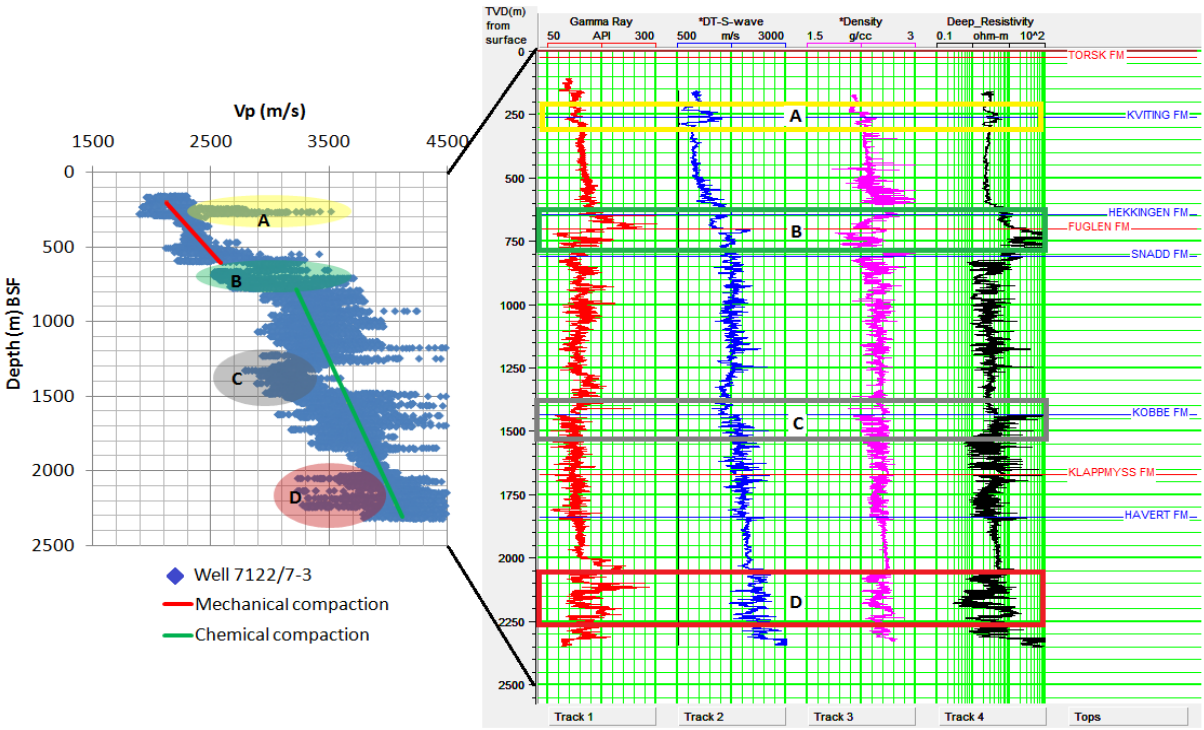

Fig. 3.19 7122/7-3 anomalous zones and corresponding petrophysical logs.

From Figure 3.19, four different zones A, B, C, and D can be can be distinguished, which deviate from the two trend lines for mechanical and chemical compaction.

Zone A: belongs to the Kviting Formation of the Nygrunnen Group. This late Cretaceous unit was formed during periods of platform uplift, and it's rich in claystone with limestone interbeds and calcareous sand units (Worsley, 2008). The carbonates present in this formation are responsible for the very high velocities of up to 3500 m/s at shallow depths of 250 m BSF. The activation energy for calcite cementation is much lower and occurs at much shallower depths unlike quartz cementation (Bjørlykke and Jahren, 2010).

Zone B: corresponds to source rocks of the Upper Jurassic – Lower Cretaceous Hekkingen and Fuglen Formations of the Adventdalen Group and part of the Kapp Toscana Group belonging to the Tubåen Formation (reservoir). The overlying source rocks are rich in marine dominated kerogen shales of up to approximately 20% TOC (Worsley, 2008). These were deposited during a renewed transgressive cycle with reduced coarse clastic input into the basin. The high kerogen content is reflected in the high gamma ray log readings, and low bulk

density, compared to shales with little or no organic content. The velocity inversion seen in this log interval is also present at similar depths in other wells.

The effect of source rocks on Vp will be discussed subsequently. Despite the low velocities present in the source rocks in Zone B, it is however still higher than overlying shales of the Kolmule, Kolje and Knurr Formations. These formations were deposited when there was a reduction in sea level, with better circulation of bottom currents except around local highs in the basin, thus establishing oxic conditions and less preservation of kerogen. The higher velocity of the source rock with more kerogen compared to the overlying shales is due to the transition from mechanically dominated compaction to chemical compaction at approximately the same depth where there is a lithologic transition. The Fuglen Formation acts as cap rock for the Kapp Toscana reservoir sands beneath. The combined effects of the source rock and Tubåen gas cap (NPD Factpages) possibly reduce the Vp in this interval.

Zone C: shows very low velocities in the chemical compaction domain. This interval shows low gamma API in the Kobbe sands then a fining upward succession at the base of the Snadd formation, inferred from gradual increasing gamma. This zone shows a transition from high to low gamma values and corresponds to the transition between the transgressive shales at the base of the Snadd formation to the sands of the Kobbe reservoir. The base of the Snadd formation has thick marine shale units deposited during a regional transgression during which most of the structural highs were submerged. During this time in the Carnian age, there were very high rates of subsidence on the Barents shelf (Worsley, 2008). The overlying sandstone units above Zone C show significantly higher velocities. These Carnian sandstones were sourced from the Baltic Shield and tend to be texturally and mineralogically mature. These sands would have had a relatively good primary reservoir quality at shallow depths. However at burial depths corresponding to chemical compaction, the mature sands will then undergo pervasive quartz cementation possibly sourced from stylolites (Bjørlykke and Jahren, 2010). This could possibly explain the high Vp values for these Carnian sands above Zone C.

Zone D: represents part of the Sassendalen Group deposited at a time when subsidence rates were also high, in the Late Triassic. This zone shows interbedded shale source rock intervals deposited under anoxic conditions, which show up with high gamma, low resistivity and low bulk densities as seen from the corresponding logs. These source rocks are time equivalent to

the oil shale Botnehia formation on Svalbard with approximately 10 %TOC (Worsley, 2008). These intervals account for the low velocities observed in this trend.

3.4.2: Uplift Estimation

Cores from shallow well sections are not usually available. As a result laboratory compaction of synthetic mudstones (different clay fractions) with a control on the initial mineralogy prior to compaction, (Fawad et al., 2010) can be employed as a model to compare data confidently known to belong to the mechanical compaction regime. In nature pure clay fractions are seldom found, and therefore in this study different mixtures of clay – clay and clay – silt have been used to quantify the amount of exhumation. The term ‘’silt ‘’ used here mineralogically refers to quartz while ‘’clay’’ refers to the phyllosilicate minerals kaolinite and smectite, as used in Fawad et al. (2010), except otherwise stated. The clay particle sizes for the experimental compaction curves used in this work are based on Mondol et al. (2008a), and range between 0.4µm-30µm while the silt used is between 4µm-40µm.

The composite shale trend for three wells with significant coverage (Figure 3.10), was sorted based the volume of shale (Vshale>80%). This composite shale plot displays mainly data points corresponding to well 7122/7-3 in the mechanical compaction domain, and as a result further exhumation estimates are based on this well only. Monomineralic shales seldom exist in nature, and usually occur with some silt. Therefore, the estimates derived from the Kaolinite–silt curve have been preferentially considered in this study as opposed to estimates from the pure kaolinite and kaolinite–smectite curves. Shale data points in the mechanical compaction domain, which are greater than the kaolinite–silt (50:50) curve possibly represent samples with kaolinite–silt ratios with more clay than silt, (matrix supported) resulting in enhanced grain reorientation and stiffening of the clay system (Fawad et al., 2010). Exhumation estimates of 700m imply that these shales have been exposed to higher pressures of about 7MPa in the past prior to exhumation, leaving the shales over consolidated. Detailed core analysis in future will be required to prove this relationship. However the kaolinite–smectite curve provides just a minimum exhumation estimate (700m) for the Goliat field. From this study it is not possible to give an exact exhumation estimate due to lack of proper mineralogical control.

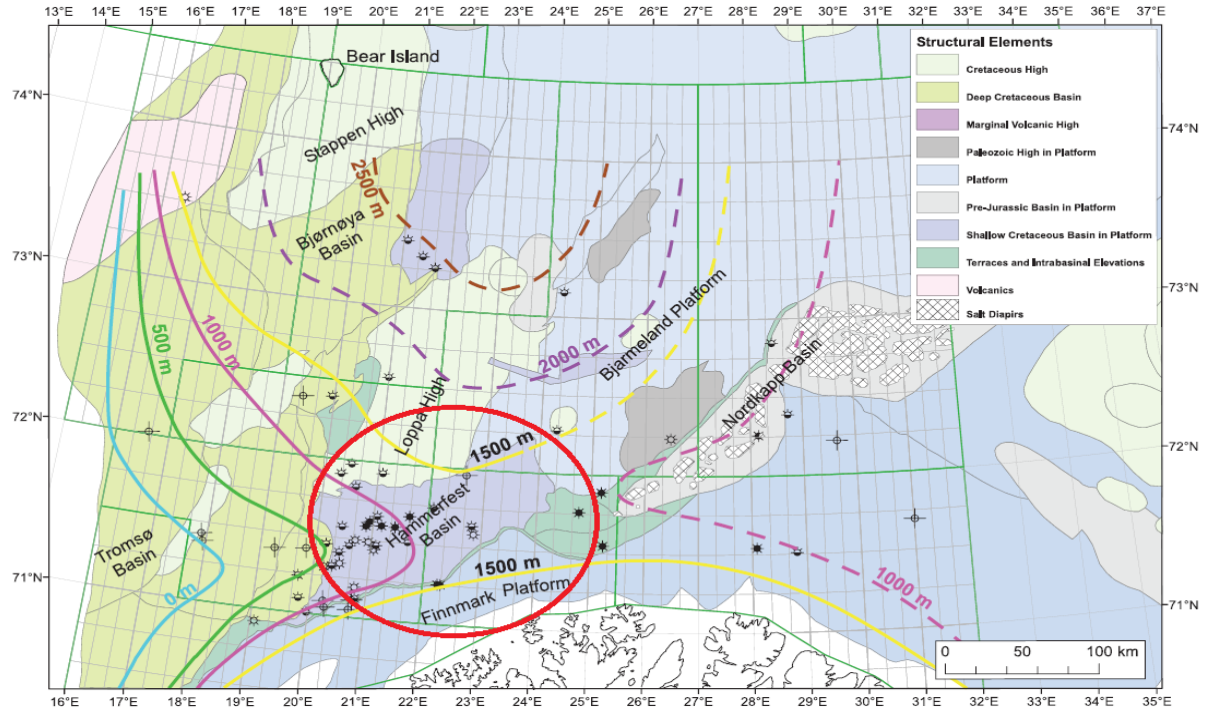

Fig. 3.20 Tentative uplift map based on Vitrinite reflectance data (modified from Ohm and Karlsen, 2008).

However the amount of uplift should range between the upper limit (1500m) defined by pure kaolinite to a lower limit (700m) defined by the mixed kaolinite-smectite curve. The upper limit (1500m) defined for exhumation in this work closely agrees with the upper limit defined by vitrinite reflectance data in Figure 3.20 from a suite of different wells on the Barents shelf (Ohm and Karlsen, 2008).

The estimates provided in this study represent the possible cumulative uplift in this area, without regard to the different episodes over which it occurred. A summary subsidence curve (Figure 3.21) for different areas on the Barents shelf including the Hammerfest basin has been presented by Ohm and Karlsen (2008).

However an intermediate estimate of 1000m may be a more likely scenario. It can be seen from Figure 3.20 that the amount of uplift decreases westward toward the Tromsø Basin and increases north of the Hammerfest basin (circled in red) towards Stappen High.

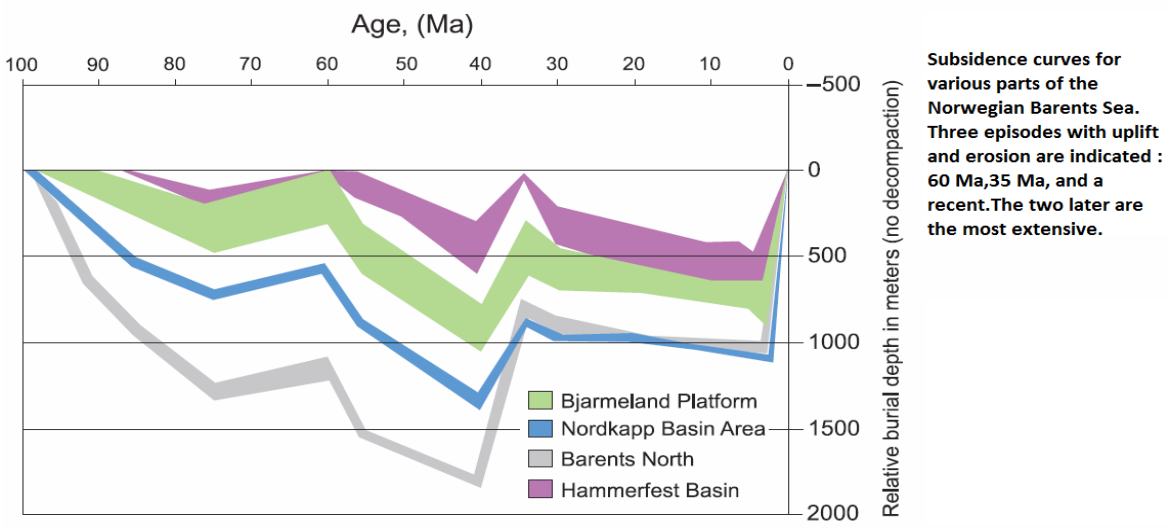

Fig. 3.21 Subsidence curves for different regions on the Barents shelf (adapted from Ohm and Karlsen, 2008).

Detailed XRD and petrographic SEM studies for the mudstones in the zone of mechanical compaction will provide some control on the mineralogy. This will provide the appropriate silt-clay ratio to the used for exhumation estimates and possibly constrain the upper limit for exhumation in the Goliat Field.

3.4.3 Transition from mechanical to chemical compaction

For a normally subsiding sedimentary basin, with average geothermal gradients (35^0C/Km) the temperature controlled transition between mechanical and chemical compaction is expected to occur at approximately 2000m BSF. The shallower transition (600m) observed in all the drilled wells in the Goliat Field provide a clear indication of the effect of uplift.

The shale trend by Japsen (1999) in Figure 3.12 shows a relatively close fit only to the shallowest Torsk Formation of the Sotbakken Group deposited during the opening of the Norwegian – Greenland Sea. The associated volcanism and tuff generation was an important source for smectite in this claystone dominated formation. This may explain the closer relationship to the Japsen (1999) shale trend for this unit considering that this trend generally shows a closer match to formations richer in illite or smectite. Of all the trends the sand trend fits best with the mechanically compacted part of section, despite the fact that these shallow formations are composed mainly of mudstones. The relatively high velocities for these

mudstones emphasize the fact that they are highly over-consolidated and have experienced higher effective stresses in their burial history than is observed today.

Stiffening of the grain framework in the chemical compaction domain may possibly be responsible for the large deviation between the experimental compaction of pure clay, clay – clay and clay – silt mixtures. After correcting for exhumation using the kaolinite – silt experimental curve, the depth at which the transition from mechanical to chemical compaction occurs is approximately 1300m BSF (Figure 3.12). This transition corresponds approximately to temperatures of 41^0C assuming a geothermal gradient of 31^0C/km. This is lower than the expected 70 – 80^0C required for onset of quartz cementation in shales as a result of illitization of smectite in the presence of K-feldspar (Thyberg et al., 2010).

A possible candidate responsible for cementation at this low temperature is the silica phase transformation from Opal-A to Opal CT which may cause an abrupt increase in Vp due to the precipitation of a critical volume of Opal CT which possibly strengthens the grain framework. Lithological changes within the Opal CT field or conversion from Opal CT to quartz may also be responsible. However evidence for the actual mineralogical transition responsible for the log transitions will need to be confirmed in future XRD and SEM petrographic techniques. Opal A is known to occur over a wide area in the Cenozoic of the Barents shelf (Roaldset and He, 1995). Roaldset and He (1995) concluded that the transition from Opal-A to Opal CT occurs at 1.4Km BSF meanwhile Opal CT to quartz transition occurs at 1.7 Km (Figure 3.22) corresponding to temperatures of 40-45^0C and 50-55^0C respectively for both transitions. The depth interval between both transitions is 300m. The expected thermodynamic temperature for the transition between Opal CT and quartz is 60-65^0C. This transition temperature is above the temperature (41^0C) observed in the Goliat Field.

The transition depths/ temperatures found for the opal A to opal CT and opal CT to quartz transitions in well 7117/9-1 indicates approximately 300m of uplift in this well. If the transition from mechanical to chemical compaction in the Goliat area is related to stiffening within the opal-CT stability field, then based on well 7117/9-1 an estimate of 1100m of uplift may be given for the Goliat area. If the transition between Opal CT and quart is responsible, an additional 300m of uplift is inferred giving a total uplift of 1400m in the Goliat area. Both estimates are based on similar geothermal gradients in well 7117/9-1 and the Goliat area.

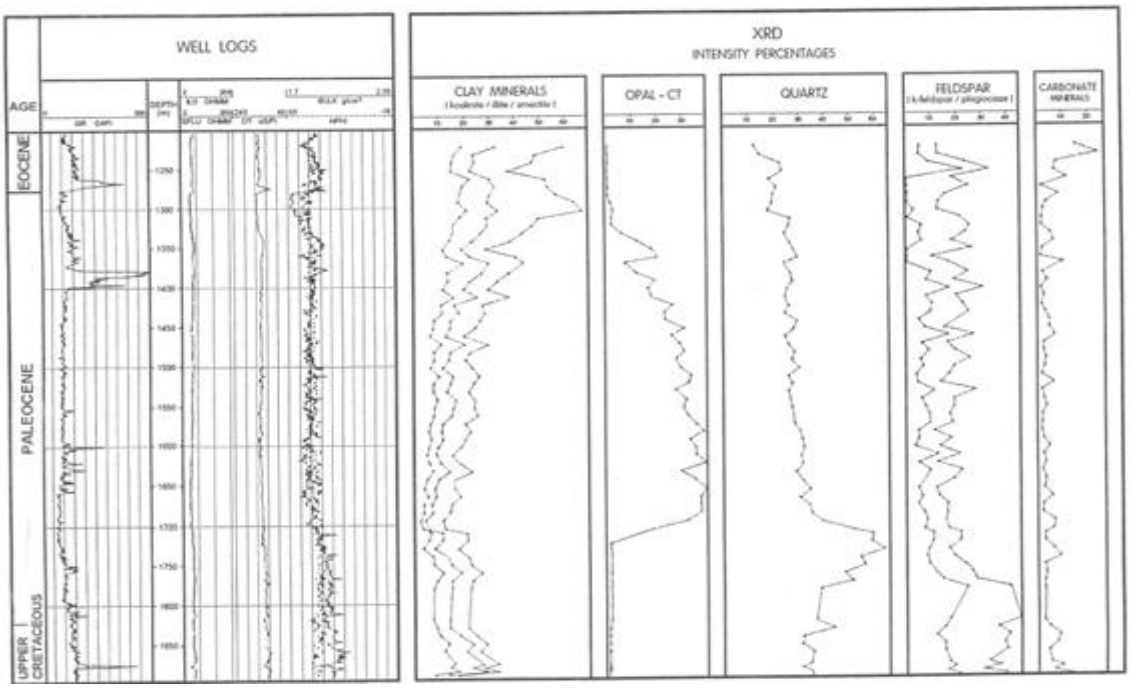

Fig. 3.22 Mineralogy of well 7117/9-1(Roaldset and He, 1995).

The present day depth at which this transition occurs will vary across the Barents shelf due to differential amounts of uplift. From the tentative uplift map shown in Figure 3.20, the amount of uplift reduces west from the Goliat field. The control well (7117/9-1) with the XRD data is located farther west from the Goliat, and as expected the present day depth of transition from Opal A to Opal CT occurs (800m) deeper than in the Goliat. This is due to the larger amount of exhumation experienced in the Goliat. Compared to well 7117/9-1, an additional uplift of the Goliat Field between 800-1100m would be expected, depending on similar paleogeothermal gradients in the two areas. Together with the 300m uplift found in well 7117/9-1 based on the present day Opal CT to quartz transition temperature, an estimate of 1100-1400m uplift in the Goliat area is expected.

In Figure 3.8, the trend corresponding to mechanical compaction (red) shows a gradient of 0.85, meanwhile the chemical compaction trend (blue) has a higher gradient of 1.68. The physical implication of this relates a higher gradient (steeper trend) to a lower change in velocity with depth. As such, in the chemical compaction domain, quartz cementation leads to significant increase in strength and grain framework stability. Thermodynamically more stable mineral assemblages are also expected to be formed. A combined effect of these factors will lower the rock response to further compaction, and therefore a smaller change in Vp with depth. Even a small amount of cement may inhibit compaction due to grain rearrangement and crushing (Bjørlykke and Jahren, 2010).

The cross plot between shear modulus and density porosity (Figure 3.9) for shales only, in well 7122/7-3 shows a 'knick' point transition at approximately 5 MPa. The significant increase in the shear modulus after onset of chemical compaction up to about 17 MPa, may be attributed to the fact that, quartz cementation will prevent further volumetric loss by grain rearrangement. Increasing the effective stress increases the degree of clay mineral alignment in shales and will yield a relatively low shear modulus in the mechanical compaction regime (Fawad et al., 2010). The shear modulus is a good frame indicator because it is insensitive to changes in pore fluid. The bulk modulus and Vp on the other hand are influenced by pore fluid type and saturation. The transition depth of 613m BSF closely agrees with the value obtained from the Vp-depth trend. A combined interpretation from both methods results to a better constraint on the transition from mechanical to chemical compaction, though further petrographic analysis from cores in this depth interval will be important to ascertain this claim.

3.4.4 Variations in the sand and shale compaction trends

Sands and shales tend to compact at varying degrees and rates due to differences in grain size and mineralogy. The shale trend illustrated in Figure 3.14 shows a smaller change of Vp with depth compared to both sand trends. This implies that the shales are stiffer and more consolidated than the sands at the same depth in the chemical compaction regime. As a result they respond less to increasing compaction with depth. Sands have a larger grain size and tend to compact more due to mechanical compaction by grain crushing, as a result of smaller number and area of grain contacts, making the effective stresses high.

Mudstones are usually deposited with a higher depositional porosity than sandstones. At greater burial depths, before the onset of chemical compaction, the inter-granular volume (IGV) for clean sands is usually more than for mudstone. When quartz cementation starts, the greatest effect may be most likely felt in the case with a smaller IGV, and the rock quickly becomes completely cemented and responds less with increasing compaction (smaller change in velocity with depth).

3.4.4 Effect of pore fluid and pore pressure

The dominant fluid in sedimentary basins is brine. Given normal sedimentation rates with equilibrium compaction, sediments will undergo dewatering with depth. The probability of generating an overpressure for the same fluid content is greater for finer grained sediments with lower permeability. The deposition of shale under high sedimentation rates will result to a situation of undrained compaction, leaving these shales at depth with an overpressure. Pore pressures greater than hydrostatic will slow down or even prevent volumetric loss with depth due to less increase of effective stress. This will lead to a larger inter granular volume before the onset of chemical compaction and therefore will require much more cement to fill all pore spaces. Therefore, overpressure during mechanical compaction represents an important mechanism in preserving porosity with depth.

Most of the shales represented here are already in the chemical compaction regime. During chemical compaction , temperature becomes the dominant controlling factor and effective stress (and hence pore pressure) will have little controle on the porosity destribution with depth (Bjørlykke and Jahren, 2010). As shown in Figure 3.16, this zone corresponds to the Kobbe oil reservoir and shows high resistivities. This demonstrates clearly the effect of varying pore fluid type on the Vp-depth profile in well 7122/7-3. The main controlling factors are the bulk modulus and the density of the saturating fluids. The shear modulus is relatively insensitive to changes in the pore fluid, but the compressiblity of hydrocarbon fluids is higher than that of formation brine. As a result even with the lower oil density compared to brine, there is still a significant reduction in Vp in that interval. The circled grey zone represents a cluster of shales which show possible overpressure effects and corresponds to zone C in Figure 3.8. This zone is the base of the Snadd Formation and is possibly an over pressured interval. During this time in the Carnian age, there were very high rates of subsidence in the Barents shelf (Worsley, 2008). Deposition of mudstones under high sedimentation rates may result to undrained compaction with depth, and then develop an overpressure. The base of the Snadd Formation acts as the cap rock for the Kobbe reservoir sands. Possible leakage of hydrocarbons from the Kobbe reservoir into the Snadd cap rock may also account for the decrease in Vp. However overpressure has little effect in the chemical compaction domain. This is because chemical compaction in thermodynamically and kinetically controlled rather than by effective stress. A fluid effect may therefore be the most likely cause for the strong reduction in Vp.

The shales deviate to higher Vp away from the upper bound as shown in Figure 3.16 because they have been over consolidated due to cementation.As a result they deviate from experimental laboratory compaction data and the published trends.

3.3.5 Effect of source rock

The major effect of the presence of source rocks on the Vp-depth profile is to cause a reduction in Vp with increasing depth. This velocity inversion with depth is shown in the Hekkingen Formation in Figure 3.18. The Hekkingen Formation is one of the major source rocks on the Barents shelf and is rich in marine dominated kerogen shales of up to approximately 20% TOC (Worsley, 2008). These were deposited during a renewed transgressive cycle with reduced coarse clastic input into the basin.

Despite the low velocities present in the Hekkingen source rock, it is however still higher than overlying shales of the Kolmule, Kolje and Knurr Formations. These formations were deposited when there was a reduction in sea level, with better circulation of bottom currents except around local highs in the basin, thus establishing oxic conditions and less preservation of kerogen (NPD Factpages). The higher velocity of the source rock with more kerogen compared to the overlying shales in case is due to the transition from mechanically dominated compaction to chemical compaction at approximately same depth where there is a lithologic transition. A combination of several factors may explain the reduction in Vp with depth for source rocks such as the Hekkingen formation in the Goliat Field. Source rocks usually have a 3D net work of compressible kerogen occurring mainly as laminae, with a preferred orientation parallel to bedding. This induces anisotropy in velocity measurements, such that vertical velocity recordings perpendicular to bedding are significantly lower (Stainforth and Reinders, 1990). This anisotropy is enhanced in mature source rocks (such as the Hekkingen Formation) during generation and expulsion of hydrocarbons as a result of adsorbed hydrocarbons on the insoluble kerogen. Conversion of solid kerogen to hydrocarbons in source rocks also increases the porosity. More important, is the geometry of the pores created. Low aspect pores parallel to bedding with low incompressibility as opposed to capillary tube type pore geometry may also further reduce Vp. Collapse of overburden load with increasing vertical effective stress due to sediment loading may be responsible for inducing micro fractures in source rocks parallel to bedding (Vernik and Liu, 1997). A combination of these factors may explain the low Vp observed in the Hekkingen Formation

CHAPTER 4 AVO MODELING

4.1 Introduction

AVO (Amplitude Versus Offset) studies variations in reflection amplitudes with changing distance (angle of incidence) between shot point and receiver for a given target reflector. Over the years this technique has been used as a direct hydrocarbon indicator (DHI), when conducting a bright spot analysis. Unconditional use of this technique without efficient pre–processing, has led to several cases of both false positive and false negative indications of in situ hydrocarbons in the subsurface. Unfortunately, bright spot anomalies are not just fluid related but also lithology dependent. In order to condition the AVO analysis from a seismic section, it is important to correct for spherical divergence, ensure removal of coherent noise such as multiples and a normal move out correction (NMO) (Gelius and Johansen, 2010). In addition to these routine corrections, the effects of variation in the overburden should be accounted for, such as anisotropy effects in the case of a highly layered cap rock and differences in mineralogy and transmission losses (Stainforth and Reinders, 1990). If these corrections are not made, then the amplitude variations with offset on the subsurface target may simply be due to variations in the overburden. Diagenetic alterations have also been documented, (such as the conversion of smectite to illite, involving the precipitation of the released silica as quartz) to be strong enough to be recognized as a seismic event (Thyberg et al., 2010). The impedance contrast between oil and water in most non – biodegraded conventional reservoirs is usually very small, and even smaller in situations where the hydrocarbons in the subsurface are present in a pseudo – critical point where no distinction exists between oil and gas (Batzle et al., 2005).

AVO modeling is a forward modeling approach that links the petrophysical reservoir parameters to seismic elastic rock properties. There is a link between changing reservoir parameters and the resultant seismic expression. For example, increasing the volume of shale in the reservoir will increase the water saturation and reduce the effective porosity. A combined effect of this has consequences for the resultant seismic response as the effective reservoir parameters change. The link between these petrophysical log properties and the effective rock seismic properties can be established using Gassmann's equation (Gelius and Johansen, 2010). Petrophysical logs contain significantly higher frequency measurements and hence better resolution compared to seismic data with attenuation wave propagation effects as

a function of depth and decreasing vertical and horizontal resolution. The effective reservoir parameters are obtained by averaging over defined depth intervals. The petrophysical logs need to be upscaled, in order to model the expected resultant AVO seismic response.

AVO modeling has wide spread applications such as in seismic data acquisition design, and pre–stack processing and interpretation which will go a long way to reduce the risks involved in hydrocarbon exploration models and enhance reservoir characterization. AVO modeling can be carried out over a wide range of approaches and data sets such as; Single interface modeling, single – gather modeling, 2D and 3D stratigraphic modeling, 2D and 3D elastic wave equation modeling (Yongyi et al., 2007).

This chapter will first present the theoretical framework and the assumptions used in generating the different models. The target zones for modeling, data, and methodology are also briefly described. The results obtained based on the assumptions used in generating the different models are subsequently explained in the discussion.

4.2 Theoretical Background

4.2.1 Vp-Vs Relationships

The main input logs required for AVO modeling include Vp, Vs, and bulk density. Not all of these petrophysical logs needed for modeling are usually available. Sometimes if present, they may be in poor condition due to bore hole washouts which significantly affects log measurements. The direct measurements of shear wave logs in particular is not common in the older wells, and even for new oil field discoveries, it is not usually present in whole well sections. As a result of these practical limitations, empirically derived Vs logs from measured Vp logs such as the ‘’Mud Rock Equation’’ (Castagna et al., 1985) is used. This equation is given by;

$$Vp = (1.16 * Vs) + 1.36 \quad (4.1)$$

Where Vp and Vs are the compressional wave and shear wave velocities given in Km/s. This equation has been derived for brine-saturated mudstones and shales, which tend to show a linear relationship. Krief et al., (1990) also suggested a linear relationship (equation 4.2) between Vp and Vs, with lithology dependent regression coefficients x and y.

$$Vp^2 = xVs^2 + y \tag{4.2}$$

Where Vp and Vs are the compressional wave and shear wave velocities given in Km/s. A significant amount of work has been done by several authors, (Han et al., 1986, Dvorkin, 2008, Xu and White, 1996) to estimate the shear wave velocity from the Vp. The Vs log is commonly used as an important frame indicator when accurately combined with Vp logs. There is an inherent lithology dependence on the Vs estimates, in siliciclastic rocks. Variations in the estimates can be observed due to variations in shape, grain size and mineralogy (Mondol et al., 2009b, Mondol et al., 2010). However in this study the Castagna et al. (1985) equation has been used to calculate Vs for shales due to its simple, yet robust nature.

4.2.2 Gassmann fluid substitution

Fluid substitution has widespread applications in time lapse seismic reservoir monitoring and also in AVO modeling and analysis. This technique has the potential to provide information about insitu fluid scenarios and then model ‘’what if ‘’ scenarios. The practical application of this technique is based on (Gassmann, 1951) given by equation 3;

$$K = K_{frame} + \frac{\left(1-\frac{K_{frame}}{K_{grain}}\right)^2}{\left[\frac{\emptyset}{K_{fluid}}+\frac{(1-\emptyset)}{K_{grain}}-\frac{K_{frame}}{\left(k_{grain}\right)^2}\right]} \tag{4.3}$$

K_{frame}, K_{grain}, K_{fluid} represent, the effective drained framework modulus, bulk modulus of the grains and fluids respectively. K and Φ represent the effective saturated bulk modulus and porosity respectively. Gassmann fluid substitution offers a possibility to model the effective seismic Vp, Vs and density of the target subsurface rock units, under different sets of conditions such as; mineralogy, porosity, pressure, temperature, water salinity and pore fluid saturation. However, in nature fluid substitution usually occurs gradually over time, yielding a homogenous rather than a patchy saturation (Gelius and Johansen, 2010). The Gassmann equation links the saturated rock bulk modulus to the porosity, fluid, and frame properties. The main assumptions in Gassmann’s equation include;

- An open pore system, in which all the pores are, connected (effective porosity). As a consequence of this assumption, the fluid offers no resistance to shear deformation and

therefore the effective dry shear modulus is the same as the effective wet shear modulus.

- All the grains are assumed to have the same physical properties. By implication, the properties of rocks with polymineralic phases are modeled into an effective monomineralic phase. This can be achieved by using effective medium models, such as the simple Voigt isostrain model. The Voigt average provides the upper bound to the effective elastic properties of the different mineral phases.
- Fully homogenous saturating pore fluid. This implies that the elastic properties of the multiphase fluid system, is replaced by an effective fluid. This can be done using a simple model such as Reuss isotress model, although more complex effective models are available. A homogenous saturation implies that the fluid properties in the individual pores are representative of the effective fluid properties.
- Gassmann equation is valid for low frequencies. This is due to dispersion effects associated with high frequencies. Frequency dependent fluid oscillations cause velocities to vary as a function of frequency.

Gassmann's theory has a limitation with regards to shaly sequences due to the presence of electrostatically bound water, in unconnected pore systems.

4.2.3 Synthetic Seismogram

From a seismic acquisition point of view, a seismic trace is a time measurement corresponding to a given source-receiver pair. The distance between any given source receiver pair, is referred to as offset. In order to model the effective rock parameters from given petrophysical logs, a synthetic seismogram can then be generated. This synthetic seismogram can then be compared to real seismic data. The main input required to generate a synthetic seismogram are the density, Vp logs and an assigned wavelet. The acoustic impedance (z) of a medium is given by a product of the density and Velocity (Vp) of that medium.

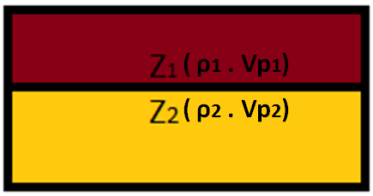

Fig. 4.1 Simple two layer model with contrasts in acoustic impedance (Z).

$$Z = \rho . Vp \tag{4.4}$$

The impedance contrast across an interface is responsible for the wave reflection phenomena. The reflection coefficient (R), across an interface is given by

$$R = \frac{Z_2 - Z_1}{Z_2 + Z_1} \tag{4.5}$$

From the formular above, the magnitude of the reflection coefficient depends on the constrast in acoustic impedance. Mathematicaly a seimic trace can then be modeled as a linear convolution between a wavelet and the earth reflectivity series as shown in Figure 4.2. The earth's reflectivity series can be described as a time series of spikes, each of which actually represents a zero offset plane wave reflection coefficient.

$$s(t) * r(t) = x(t) \tag{4.6}$$

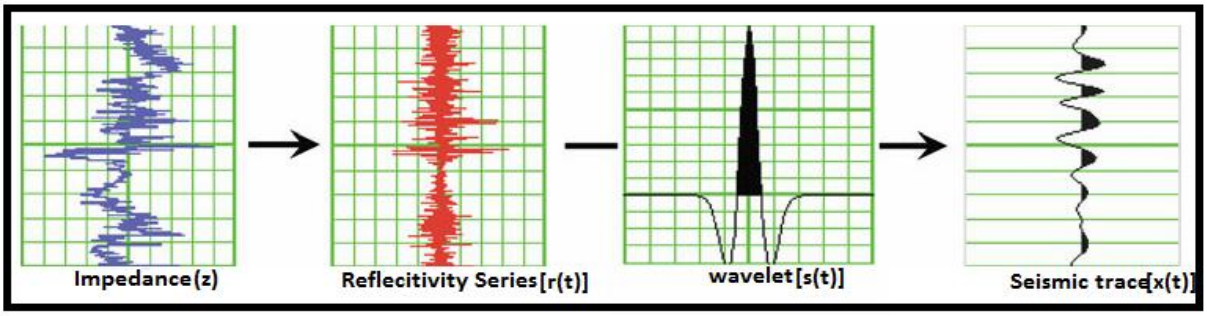

Fig. 4.2 Convolution between the wavelet and the reflectivity series (adapted from Mondol, 2010).

Some assumptions in the convolutional trace model include;

- No variation of the source pulse s(t), with depth i.e. stationary source pulse
- No noise contribution present
- Normal incident plane waves through a simple horizontal stratigraphically layered earth model.

The synthetic seismogram employed in this study, compirise of NMO corrected Common Mid Point (CMP) gathers (groups of traces with a common mid-point between source and recievers). Analysis of these gathers usually show offset dependent reflectivity (variation in the zero-offset reflection coefficient as a function of angle of incidence).

4.2.3 Angle dependent reflection coefficient

A normal incident P-wave on any given interface usually generates only reflected and transmitted P-waves. In cases where the angle of incidence $\Phi_1>0$, a second pair of reflected and transmited S-waves are generated. This phenomenon is known as mode-conversion as shown in Figure 4.3.

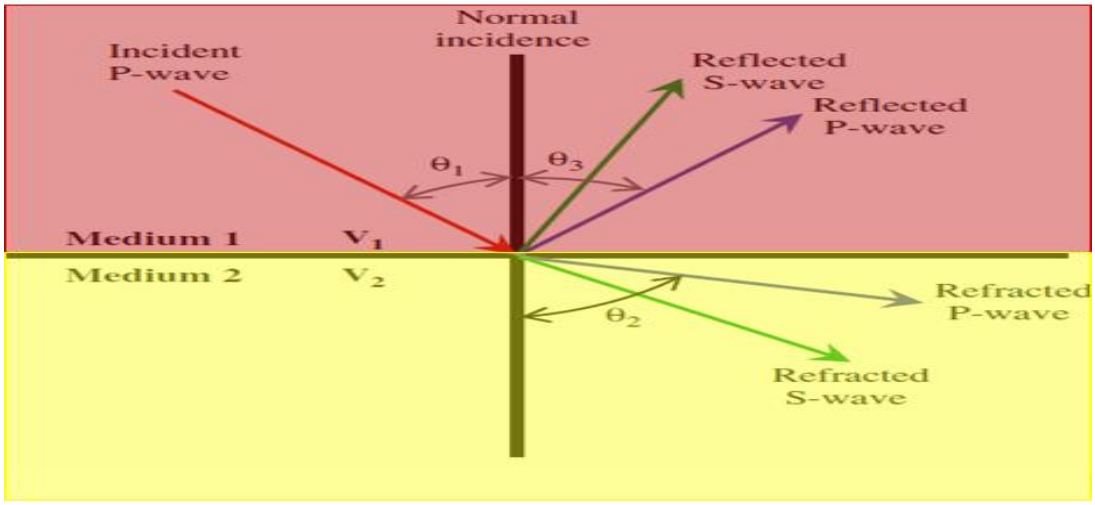

Fig. 4.3 Mode conversion of P-waves (modified from Mondol, 2010).

The waves across the interface between both media are reflected and refracted according to Snell's law given by ;

$$\frac{\sin \emptyset_1}{\sin \emptyset_2} = \frac{V_2}{V_1} \tag{4.7}$$

Conventional marine seismic acquisition surveys with streamers located at the sea surface do not record these converted S-waves. Despite this limmitation, the P-P reflection coefficient contains indirect shear wave information as a result of mode conversion. AVO is the appropriate technique that tries to extract the hidden information.

Knot-Zoeppritz equations describe the variation in reflection coefficient as a function of angle of incidence. The exact Zoeppritz equations do not provide a simple physical interpretation which can be applied practically. There are several approximations to the Zoeppritz equations. Aki and Richards (1980), proposed a first order linear approximation of the Zoeppritz equation. For small angles (best fit to Zoeppritz up to approximately 35^0), the linearised version is simplified according to Wiggens approximation into ;

$$R_{pp}(\emptyset) \approx R_p + BSin^2\,\emptyset \quad (4.8)$$

Where; $R_p = \frac{1}{2}\left(\frac{\Delta V_p}{V_p} + \frac{\Delta \rho}{\rho}\right)$ (4.9)

$$R_s = \frac{1}{2}\left(\frac{\Delta V_s}{V_s} + \frac{\Delta \rho}{\rho}\right) \quad (4.10)$$

$$B = R_p - 2R_s \quad (4.11)$$

$R_{pp}(\Phi)$ is the P-P reflection coeffecient at angle of incidence(Φ). Rp and B in AVO terminology are refered to as the AVO intercept and AVO gradient respectively. Rp and Rs are the zero offset reflection coefficients for V_p and V_s respectively, after performing a linearized first order analysis. ΔV_p and ΔV_s represents the velocity contrast across the interface, meanwhile V_p and V_s represent the average velocity across the interface. $\Delta\rho$ represents the density contrast across the interface, meanwhile ρ is the average denisty across the interface.

The Aki-Richards approximation is simple, yet robust enough to be applied practically in AVO synthetic modeling work flows. The AVO quantities can be plotted seperately as a gradient stack or an intercept stack. Depending on the purpose, combined sections can also be constructed which can enhance bright spot events at the expense of lithological events. On the other hand, the combined sections could be used in a manner so as enhance strong shear wave reflectivities (Gelius and Johansen, 2010).

4.2.4 Classification of reservoir sands based on AVO

The seismically extracted AVO parameters (AVO intercept and AVO gradient) have been used by to classify gas sands (Rutherford and Williams, 1989). This classification was initially based just on the AVO intercept, taken as zero-offset reflection coeffcient. Modern classification schemes combine both the AVO gradient and AVO intercept, giving rise to four gas sand classes in a simplified overlying shale and sand reservoir ;

- ***Class I gas sands*:** These are sands with impedances higher than the overlying shale. They show a large positive zero offset reflection coefficient at the boundery between

shale and sand. The reflection coefficients decreases with offset. This type of behaviour is common for highly compacted mature sands in onshore environments.

- ***Class II gas sands*:** These are sands with a small impedance contrast with the overlying shale. As a result they have very low normal incidence reflectivity. These sands usually show intermediate levels of mechanical and chemical compaction. A large change in reflecitivity with offset is typical of this class, and in some cases polarity changes could occur if the zero offset reflection coefficient is positive. This class is common to both offshore and onshore sands.
- ***Class III and IV gas sands*:** These gas sands have a lower impedance than the overlying shales. This is common for unconsolidated sands, and show a large negative zero-offset reflectivity. These sands are classical ‘’bright spots’’ on stacked seismic data, because they have large reflectivities for all ofsets. Both class III and IV sands are usually associated with a marine envirionment. Class IV sands show decreasing reflectivity with offset (positive gradient), meanwhile class III shows an inverse relationship as shown in Figure 4.4.

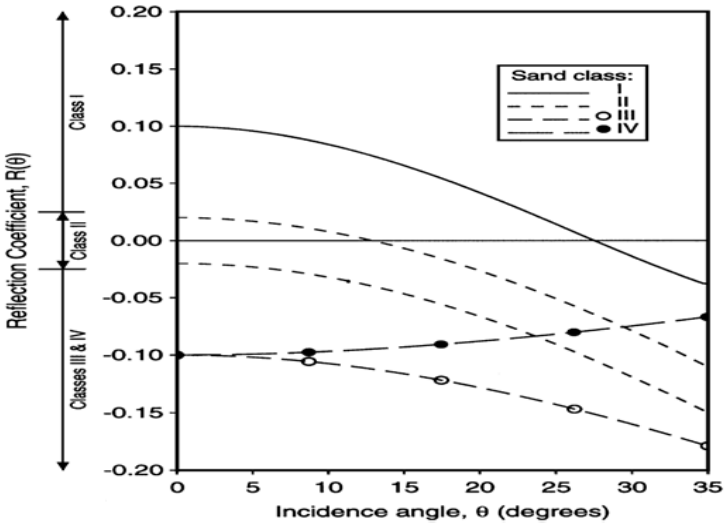

Fig. 4.4 Rutherford and Williams (1989) classification scheme based on the AVO intercept.

From the above classification it is evident that the reflectivities of gas sands do not necessarily increase with offset. More advanced classification schemes combine the AVO gradient and the AVO intercept as shown in Figure 4.5 .

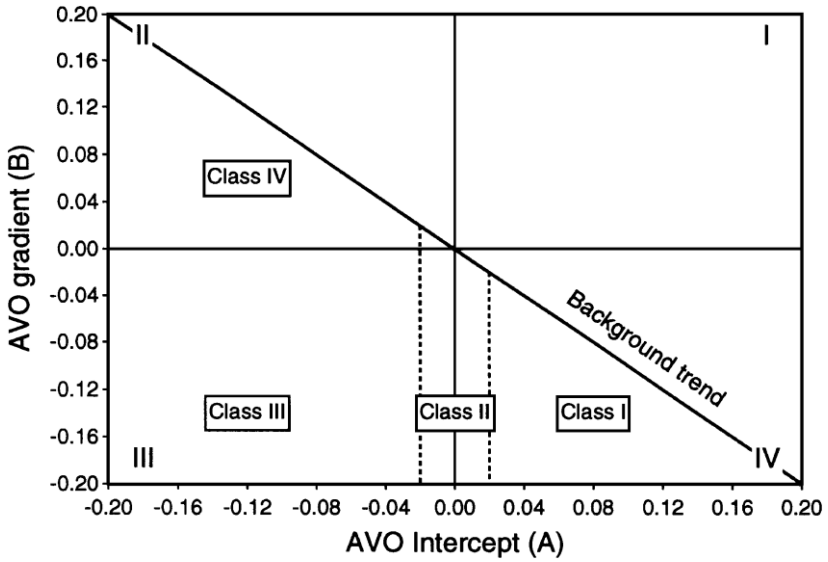

Fig. 4.5 AVO intercept and AVO gradient crossplot classification of gas sands (Rutherford and Williams,1989).

The background trend represents the gradient-intercept trend for a water saturated siliciclastic system, based on the ‘’mud rock’’ line by (Castagna et al., 1985). The background trend line varies depending on the V_p/V_s ratio. By combining Rutherford and Williams (1989) classification scheme, together with the ‘’mud rock’’ line, anomalous data points falling far from the background values can easily be iditified as potential candidates for gas sands. The AVO intercept depends on the impedance constrast, meanwhile the AVO gradient depends on contrasts in the poisson’s ratio. A summary of the behaviour of the various gas sands has been presented in Table 4.1.

Table 4.1 Summary Rutherford and Williams classification scheme assuming a ‘’background’’ trend with a negative slope (Castagna et al., 1998).

CLASS	RELATIVE IMPEDANCE	QUADRANT	A	B	REMARKS
I	Higher than overlying unit	IV	+	-	Reflection coefficient(and magnitude)decrease with increasing offset
II	About the same as the overlying unit	III or IV	±	-	Reflection magnitude may increase or decrease with offset, and may referse

					polarity
III	Lower than overlying unit	III	-	-	Reflection magnitude increases with offset
IV	Lower than overlying unit	II	-	+	Reflection magnitude decreases with offset

4.3 Database and methodology

AVO modeling for 'in-situ' and 'what if' scenarios has been carried out for two main reservoir units; the thicker, and deeper Kobbe oil reservoir of Mid – Triassic age, and the Tubåen reservoir of Jurassic age which is thinner, shallower and with a small gas cap. Both reservoirs have different cap rock properties. The Fuglen cap rock shows a relatively higher resistivity, Vp, Vs, and bulk density compared to the base of the Snadd Formation which acts as the cap rock for the Kobbe reservoir (Figure 4.6). In order to understand the AVO response of these reservoir units, it is important to investigate the lateral consistency of the AVO response for each of these reservoirs throughout in the Goliat Field based on the available well data. In order to achieve this, a suite of 6 wells have been used.

The main input wells for AVO modeling for the Kobbe and Tubåen reservoirs used in this study are presented in Table 4.2 and Table 4.3. The Kobbe reservoir is deeper than the total drilled depth in wells 7122/7-1 and 7122/7-2. The Tubåen reservoir pinches out laterally between the wells into the Fruholmen formation in well 7122/7-4 and well 7122/7-5. Well 7122/7-5A is a side track well from well 7122/7-5, and does not have measured log values for the Tubåen reservoir. Due to a combination of lateral facies variation and incomplete log suits, the same reservoir cannot be analyzed throughout the available well data.

Table 4.2 Kobbe formation depth and thickness variation.

WELL NAME	DEPTH(M) BSF	THICKNESS (M)
7122/7-3	1440	236
7122/7-4	1399	248
7122/7-5	1474	258

Table 4.3 Tubåen formation depth and thickness variation.

WELL NAME	DEPTH(M) BSF	THICKNESS (M)
7122/7-1	696	24
7122/7-2	683	118
7122/7-3	719	93

The Kobbe reservoir (Table 4.2) is located at much deeper depths compared to the Tubåen reservoir (Table 4.3), though both are not presently located at maximum burial depths, due to regional exhumation in this area. Prior to exhumation these reservoirs had been subjected to sufficient burial depths and corresponding temperatures for cementation to take place, which significantly reduces the reservoir quality and increases the degree of heterogeneity. The base of the Snadd formation is characterized by thick shale units in this area which serves as cap rock for the underlying Kobbe reservoirs as shown in Figure 4.6.

From Figure 4.6, it is evident that there is a larger contrast in resistivity between the base of the Snadd Formation, and the underlying Kobbe reservoir, compared to the case of Fuglen cap rock and the Tubåen reservoir. The computed poison's ratio for the highlighted target horizons shows a significant drop. The target for AVO modeling carried out in this study focuses on the top section of the reservoir, at the interface between the cap and reservoir rock. These target interfaces show a relatively clear contrast based on the gamma ray log. Relatively clean sands were chosen to minimize limitations in the Gassmann model with regard to shaly sandstones.

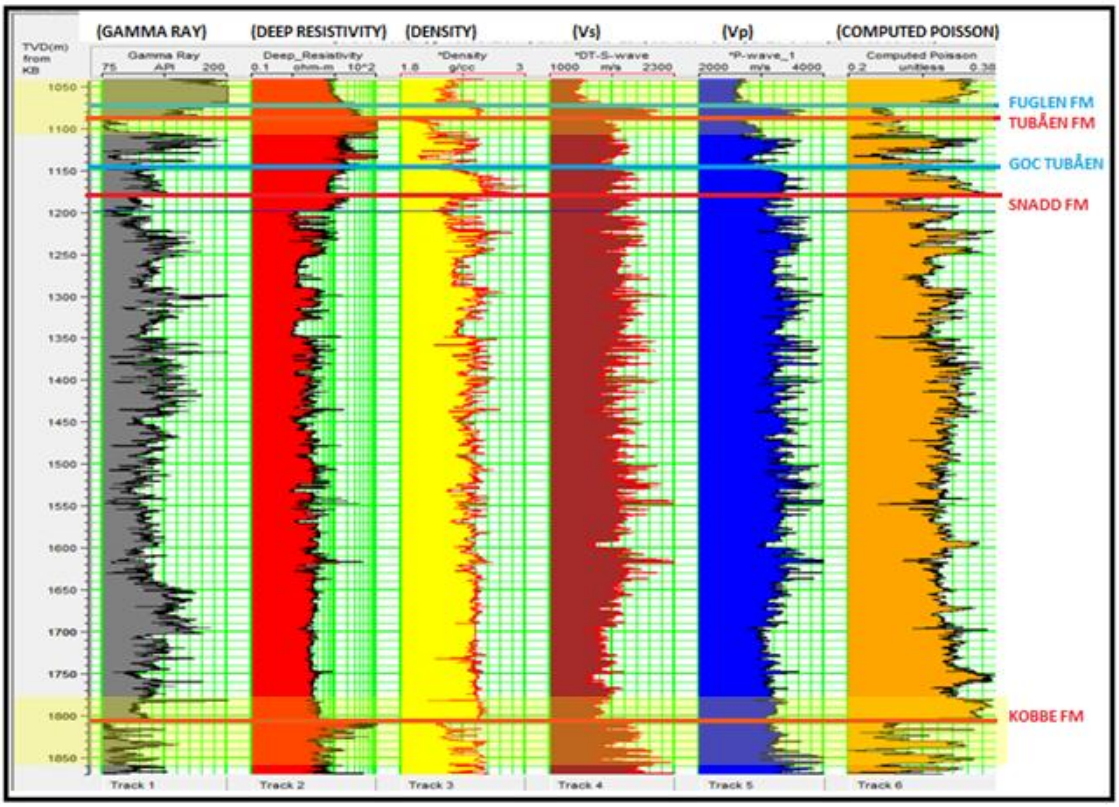

Fig. 4.6 Gamma, Deep Resistivity, Density, Vs, Vp and Computed Poisson log intervals for the target zones (highlighted in yellow) in the Tubåen and Kobbe reservoir (well 7122/7-3).

A practical approach to AVO modeling using Hampson-Russel software involves generating a model for in-situ and then ‘’what if ’’ scenarios. AVO modeling is usually carried out in order to determine the anticipated anomaly.

The main input logs used in AVO modeling are Vp, Vs and density logs. Direct recordings of Vs are usually not present in all the wells, and the Vp log was then used to create a Vs log using linear Log transforms in Hampson-Russel. The Castanga ‘’mud rock’’ equation was then applied to generate Vs in the wells where this log is absent. An appropriate well log upscale was then chosen depending on the size of the target reservoir. Upscaling is important because the well logs contain higher frequency information than actual seismic data. This also reduces the computing time in cases of a large data set. There is usually a tradeoff between the resolution and increasing the block size. Larger block sizes will contain less frequency information. The maximum block size used in this study is 25m. The corresponding computed impedance and computed reflectivity are automatically generated depending on which of the input upscaled logs are active.

One important step in the work flow needed to generate a synthetic seismogram, involves creating a seismic wavelet. The default Ricker Linear wavelet was used in this study. However for comparison to real seismic data, much more complex forms of wavelet extraction is necessary either from the suite of well logs or from the seismic alone.

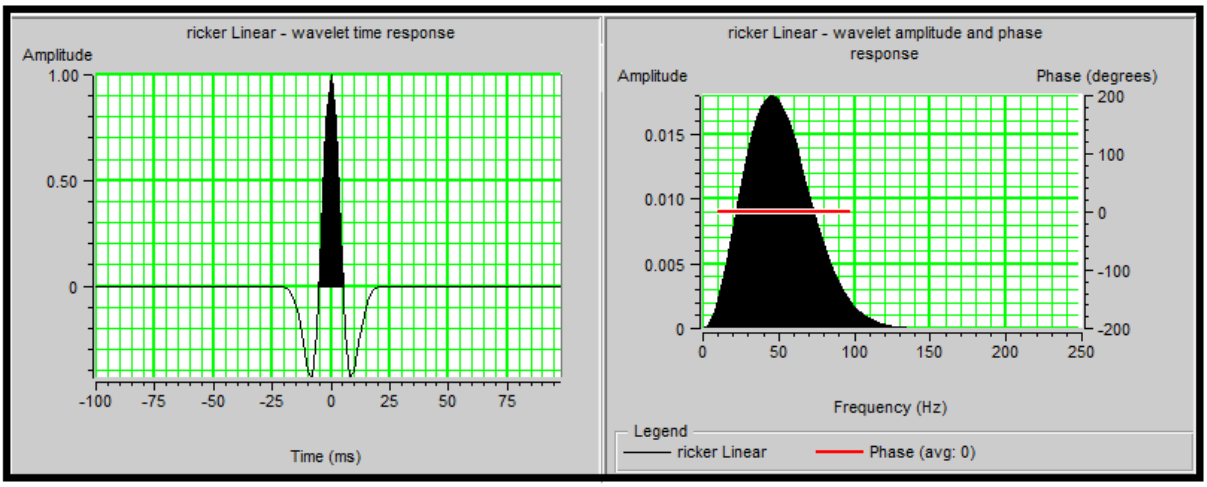

Fig. 4.7 Time and frequency domain of the Ricker linear wavelet used in this study.

A peak using this wavelet signifies an increase in acoustic impedance. The domain frequency of this wavelet as shown in Figure 4.7 is 45 Hz. The Ricker linear wavelet used has a wavelength of 200ms and employs a sample rate of 2ms. The average phase of this wavelet is a zero phase. There are no side lobes in this wavelet, leading to an ideal signal-to-noise ratio. This gives an exaggerated vertical resolution than can be normally achieved in a seismic exploration survey.

In order to generate an offset/angle dependent synthetic seismogram, automated ray tracing was used to calculate the angle of incidence. The amplitudes were then calculated using the full Zoeppritz equation and then analyzed using the simplified Aki-Richard equation. The offset range used in generating the synthetic seismogram ranged from 0-1000m, with an output sample rate of 2ms. No effects of geometrical spreading or transmission losses were considered in the model. The synthetic seismic outputs used in this study are NMO corrected CMP gathers. Output reflectivity was chosen over output amplitude in Hampson-Russel, as this generates a synthetic seismic with better vertical resolution (Figure 4.8).

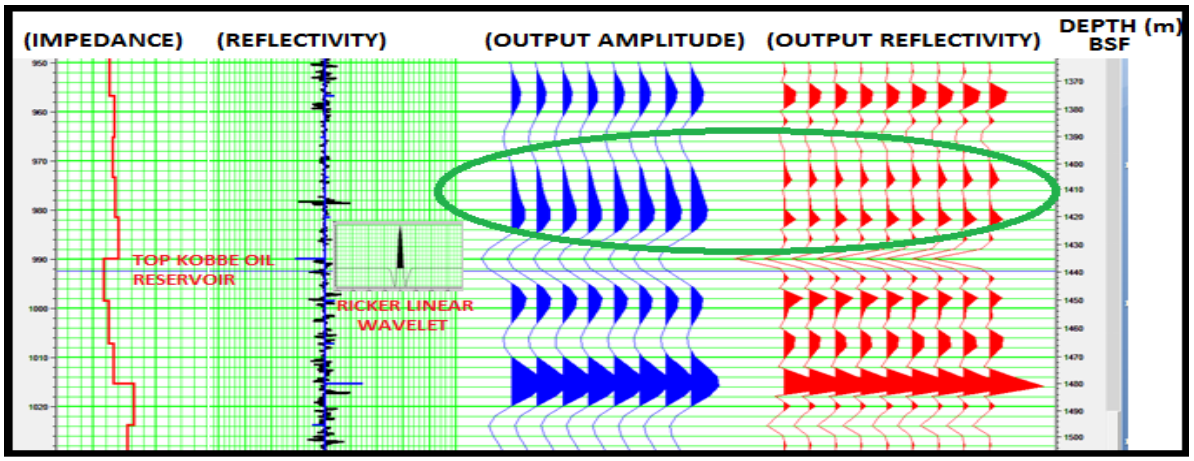

Fig. 4.8 Resolution differences using output ''reflectivity'' compared with output ''amplitude'' for Kobbe reservoir in well 7122/7-3.

The Biot-Gassmann method is then applied using Fluid Replacement Modeling (FRM) in Hampson-Russel to investigate 'what if' scenarios for different fluid types and saturations. The frame properties of the rock are assumed to be constant. Pressure effects are not modeled in this study. As a consequence of this, the input porosity is set to be equal to output fluid substituted model.

Table 4.4 Matrix properties used for fluid replacement modeling.

Matrix Type	Sandstone
Bulk Modulus	40 (GPa)
Shear Modulus	44 (GPa)
Density	2.65 (g/cc)

Table 4.5 Fluid properties used for fluid replacement modeling.

Fluid Type	Bulk Modulus(GPa)	Density (g/cc)
Brine	2.38	1.09
Oil	1	0.75
Gas	0.02	0.1

The matrix and fluid properties presented in Table 4.4 and 4.5 represent the default values in the Hampson-Russel software based on Batzle and Wang (1992). These properties were set as constant and used for the different fluid saturations in this study. The assumed matrix and

fluid properties, used for different reservoir sections is an over simplification of the actual properties. Despite these simplifications, the Biot-Gassmann approach is yet robust enough to give consistent results.

4.4 Results

The two main reservoirs of focus are the Tubåen and Kobbe formations. The input logs shown in Figure 4.9 have been averaged for every 15m (block 15). The density, Vs and Vp upscaled logs of the target zone are highlighted in yellow. The offset dependent reflectivity for all the wells has been generated using the Zoeppritz equation. The amplitudes have been extracted using the Aki-Richard two term parameter equation, and only the best fit lines have been represented.

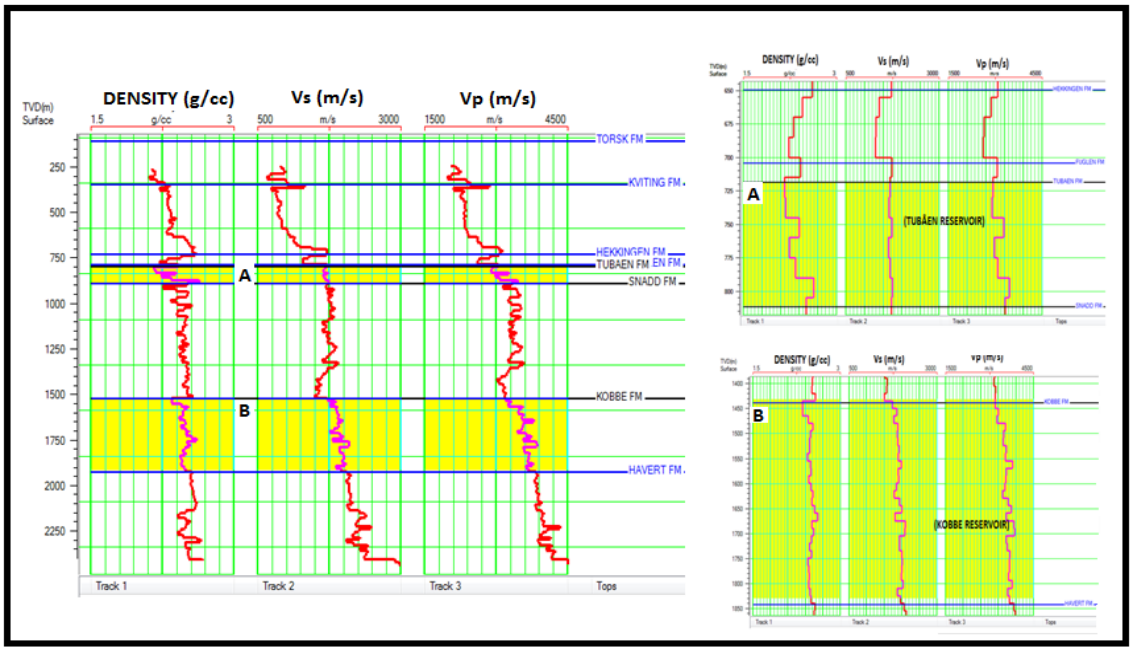

Fig. 4.9 Density, Vs and Vp logs generated by 15 m averaging for Tubåen (A) and Kobbe (B) reservoirs.

4.5 Sensitivity analysis

Despite the simplicity of the Gassmann model, it is still robust enough in providing quantitative changes in petrophysical rock parameters for different fluid scenarios for the Kobbe reservoir in well 7122/7-3. The insitu modeled fluid saturation is an oil filled reservoir.

Table 4.6 Variation in Vp, Vs, density and Poisson's ratio with changing gas saturations.

Gas (%)	%ΔVp	%ΔPoissons Ratio	%ΔDensity	%ΔVs
10	**-17.247**	**-29.637**	**-0.117**	**0.059**
50	**-21.573**	**-43.369**	**-0.588**	**0.296**
90.	**-22.043**	**-45.723**	**-1.059**	**0.534**

The analysis in Table 4.6 compares the sensitivity of the density, Poisson's ratio, Vs and Vp in a gas–oil system. After introducing 10% Gas into the reservoir, there is a significant drop in the Poisson's ratio and Vp by 29.64% and 17.25% respectively as shown in Figure. 4.10. For the same 10% gas saturation, there is a relatively insignificant drop in the density, meanwhile Vs shows a rather slight increase as expected.

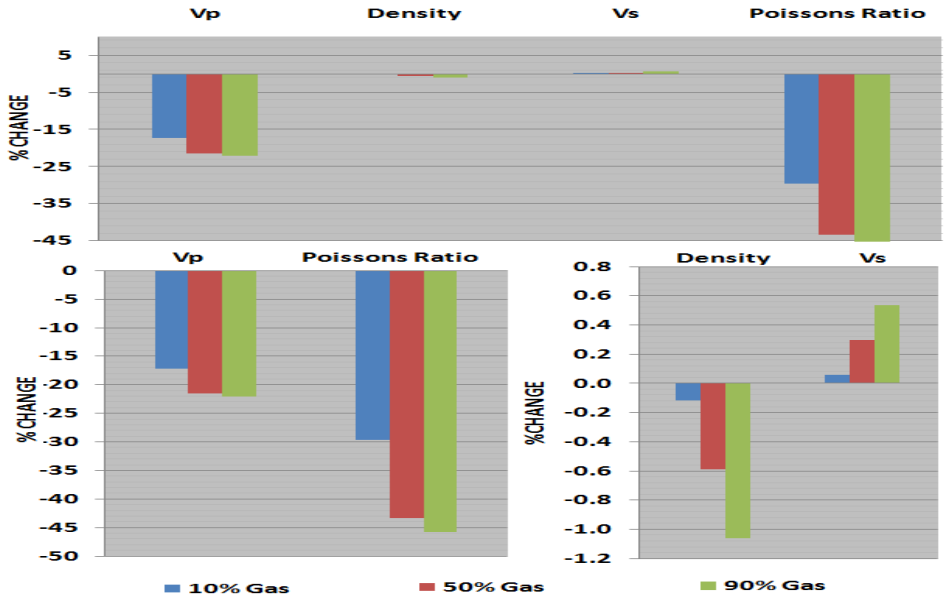

Fig. 4.10 Effect of changing gas saturations on Vp, density, Vs and Poisson's ratio.

Increasing the gas saturations after 10%, results to much smaller changes in these petrophysical rock parameters when compared to incipient introduction of gas. This pattern is the same for increasing gas saturations up to 90% gas. Vs is relatively insensitive to the changing saturations and can be used as frame indicator.

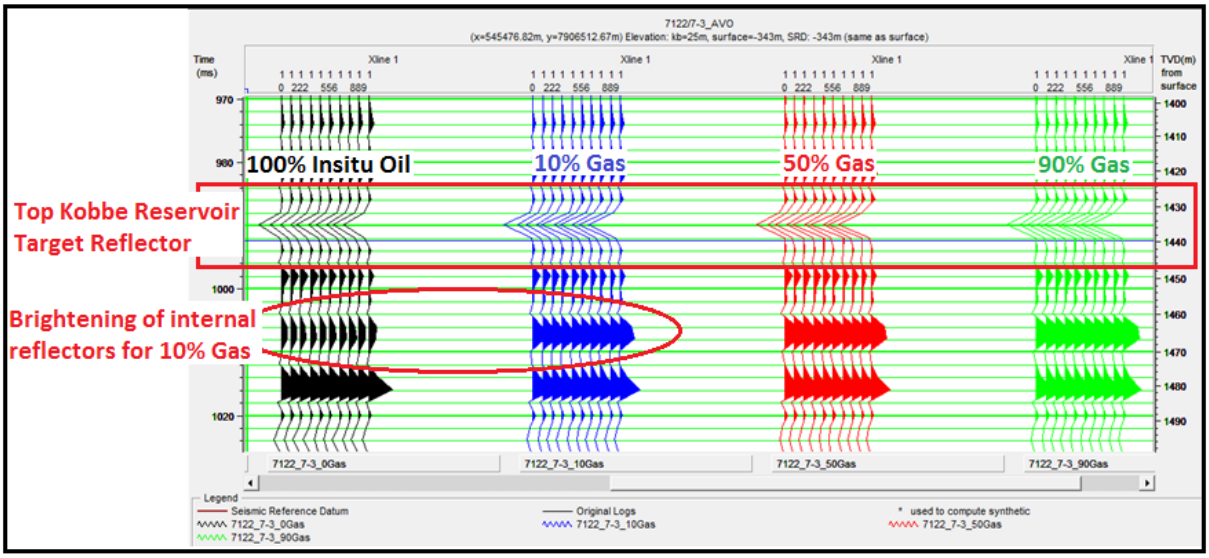

Fig. 4.11 Synthetic seismic generated using a Ricker linear wavelet.

The synthetic seismic for the different saturation scenarios, have been generated using a Ricker Linear wavelet and applying the Zoeppritz equation for a total offset of 1000m (Figure 4.11). The data has been displayed using the normal polarity convention. The wiggled traces have a color infill for the positive reflection coefficients. The corresponding synthetic seismic for the different saturations show a slight change just for the initial 10% gas saturation. The synthetic seismic data for higher gas saturations are more or less the same. This observation is consistent with the relatively large changes in the petrophysical parameters just for incipient 10% gas saturation.

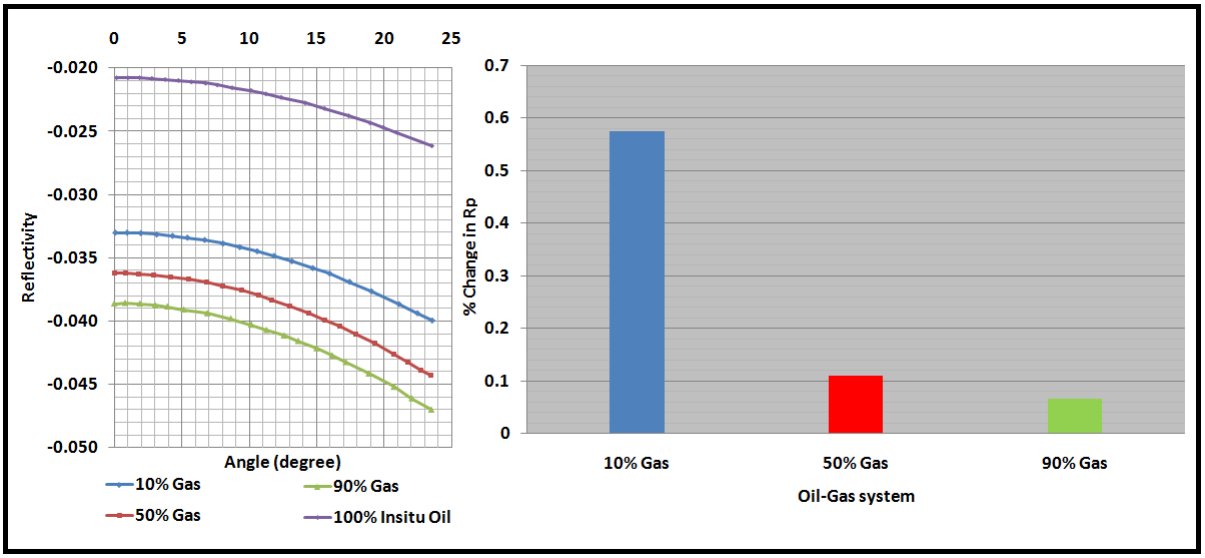

Fig. 4.12 Effect of changing gas saturations on the zero-offset reflectivity (Rp) in an oil-gas system.

The effect of changing saturations is much more evident, by comparing the angle dependent reflectivity with offset (Figure 4.12). The magnitude of the zero offset reflection coefficient (AVO intercept), increases i.e. becomes more negative with increasing gas saturation. All four scenarios have a negative AVO intercept and a negative gradient. The percentage change in the AVO intercept (calculated for each successive increment in gas saturation), is greatest for 10% gas and much smaller for 50% and 90% respectively.

4.5.1 Variations in half space models

The models described here represent simple two layer models with a single interface. Only the top target reflector has been used in this study without considering the base of the reservoir horizon of interest.

The magnitude in the zero offset reflection coefficient, ranges from - 0.050 to -0.009 for all fluid scenarios in the Tubåen and Kobbe Formations considered in this study (Table 4.7 and Table 4.8). Subtracting the magnitudes of both limits and dividing by 2 gives a ‘’cut-off ‘value of -0.021. Rp values more negative than this value are considered in this study as relatively strong, meanwhile amplitude values less negative than the cut-off limit are considered weak. The cap rocks for the Tubåen and Kobbe reservoir units are Fuglen and Snadd Formations.

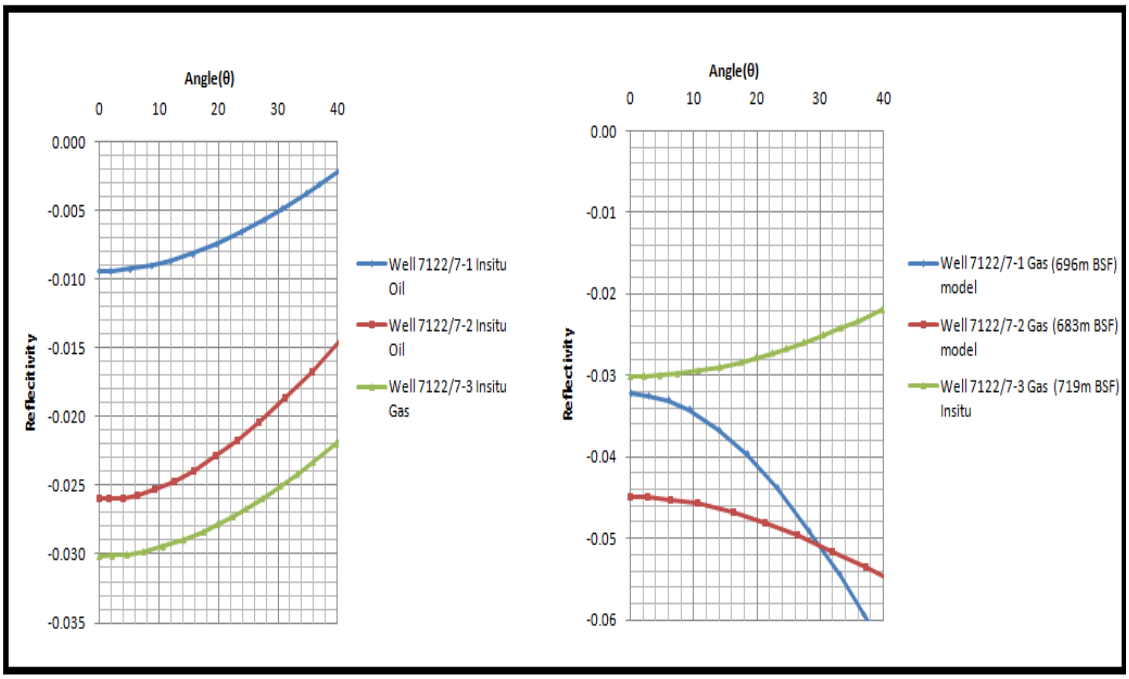

Fig. 4.13 Angle dependent reflectivity for Tubåen Reservoir in an oil-gas system.

Table 4.7 Tubåen Reservoir AVO classification.

WELL	PORE FLUID	CLASS	ZERO OFFSET Rp
7122/7-1	INSITU OIL	WEAK IV	-0.009
	GAS	STRONG III	-0.032
7122/7-2	INSITU OIL	WEAK IV	-0.013
	GAS	STRONG III	-0.032
7122/7-3	INSITU GAS	STRONG IV	-0.030
	BRINE	STRONG IV	-0.031

The Tubåen reservoir shown in Figure 4.13 shows a negative zero offset reflectivity with offset and a positive gradient (class IV) for all three wells. However, there are variations observed in the zero offset reflectivity. Insitu gas scenario in well 7122/7-3 shows the largest zero offset reflectivity compared to the other insitu oil scenarios. After Gassmann fluid replacement modeling (FRM), the insitu oil scenarios, change from weak to relatively strong zero offset reflectivity, and with a negative gradient (becomes more negative with increasing offset). The increase in reflectivity with offset is greatest for the gas model in well 7122/7-1. Meanwhile the change in reflectivity with offset for insitu oil scenario for the Tubåen

reservoir in well 7122/7-2 is greater than that observed for the corresponding gas model in the same well. There is no significant change after replacement of insitu gas with brine in well 7122/7-3 as shown in Figure 4.14.

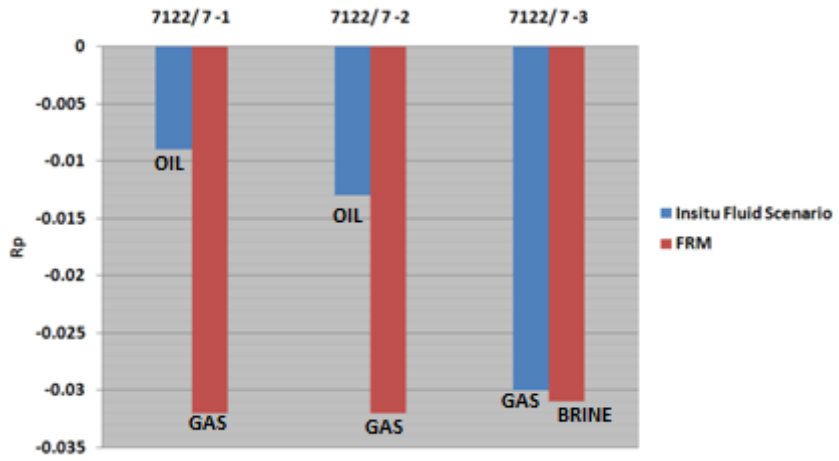

Fig. 4.14 Quantitative changes in Rp for the Tubåen reservoir after fluid replacement modeling.

All insitu models for the Kobbe reservoir based on the ‘’cut off value’’ show weak zero offset reflectivity. The insitu oil models for the Kobbe reservoir in well 7122/7-3 and 7122/7-4 show a positive gradient and negative AVO intercept (Class IV), same with the insitu brine scenario in well 7122/7-5A. Only well 7122/7-3 insitu oil scenario shows a negative gradient. For the insitu scenarios, there is a progressive increase in the strength of the zero offset reflectivity from brine to oil and gas. The zero offset values for insitu Kobbe oil reservoir lies between those of brine and gas. The insitu oil scenario in well 7122/7-3 shows the largest change in reflectivity with offset.

After fluid replacement modeling, the Kobbe reservoir in all the wells, show a stronger zero offset reflectivity, with negative gradients as shown in Figure 4.15. The gas model corresponding to in situ brine shows the strongest zero offset reflectivity, when compared to all modeled gas scenarios in the different wells. Well 7122/7-3 Kobbe gas scenario shows more negative zero offset reflectivity than its insitu counterpart but maintains the same negative gradient. All the other wells show a change in the sign of the gradient, after fluid substitution.

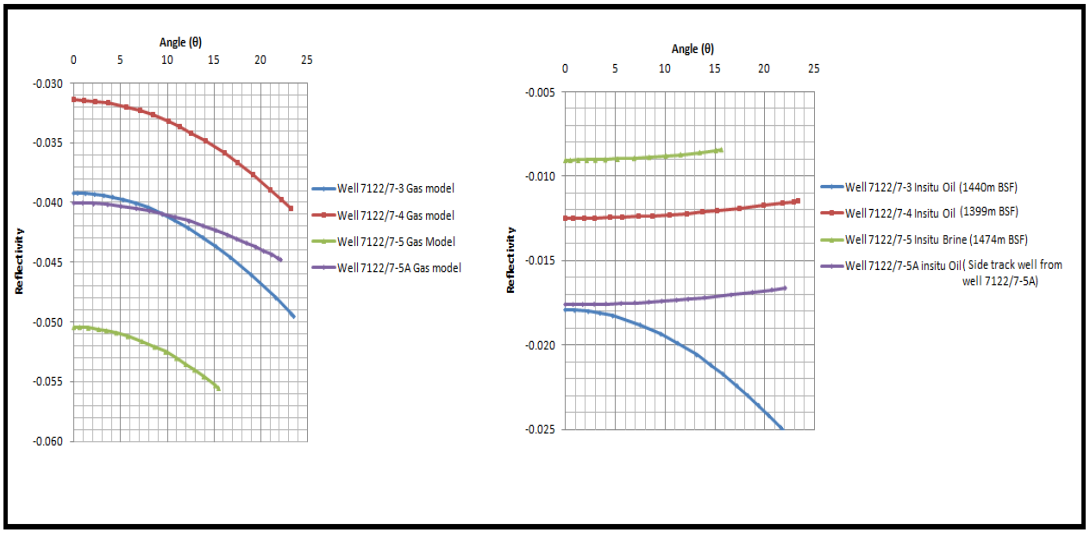

Fig. 4.15 Kobbe reservoir offset dependent reflectivity before and after fluid substitution.

Table 4.8 Kobbe Reservoir AVO classification.

WELL	PORE FLUID	CLASS	ZERO OFFSET Rp
7122/7-3	INSITU OIL	WEAK III	-0.018
	GAS	STRONG III	-0.039
7122/7-4	INSITU OIL	WEAK IV	-0.013
	GAS	STRONG III	-0.032
7122/7-5	INSITU BRINE	WEAK CLASS IV	-0.009
	GAS	STRONG CLASS III	-0.050
7122/7-5A	INSITU OIL	WEAK CLASS IV	-0.018
	GAS	STRONG CLASS III	-0.040

The change in reflectivity (Rp) between the insitu scenarios and the corresponding gas model for the Kobbe reservoir is seen to vary depending on insitu fluid type illustrated in Figure 4.16. The greatest change is observed for insitu brine scenario in well 7122/7-5. The corresponding changes in reflectivity for the insitu oil models are relatively same.

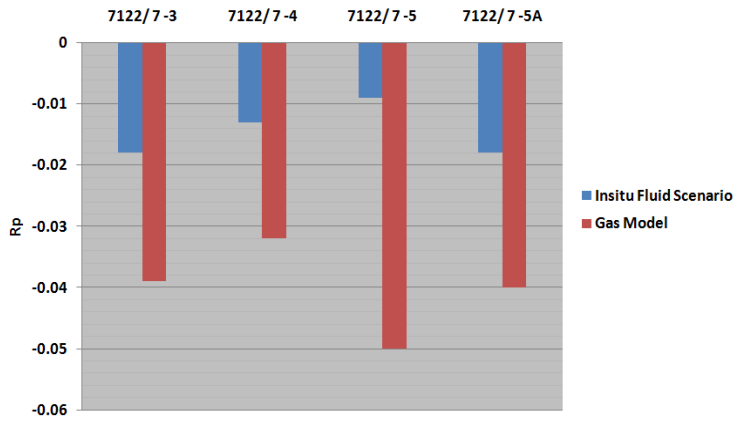

Fig. 4.16 Quantitative changes in Rp for the Kobbe reservoir after fluid replacement modeling.

4.5.2 Effect of block size variation on the AVO signature

The synthetic NMO corrected CDP gathers generated using a Ricker, linear wavelet for the Tubåen reservoir in well 7122/7-3 shows distinct results for different block sizes (Figure. 4.17). Block 25 and Block 15 synthetics are based on averaged Vp, Vs, density logs for every 25m and 15 m respectively.

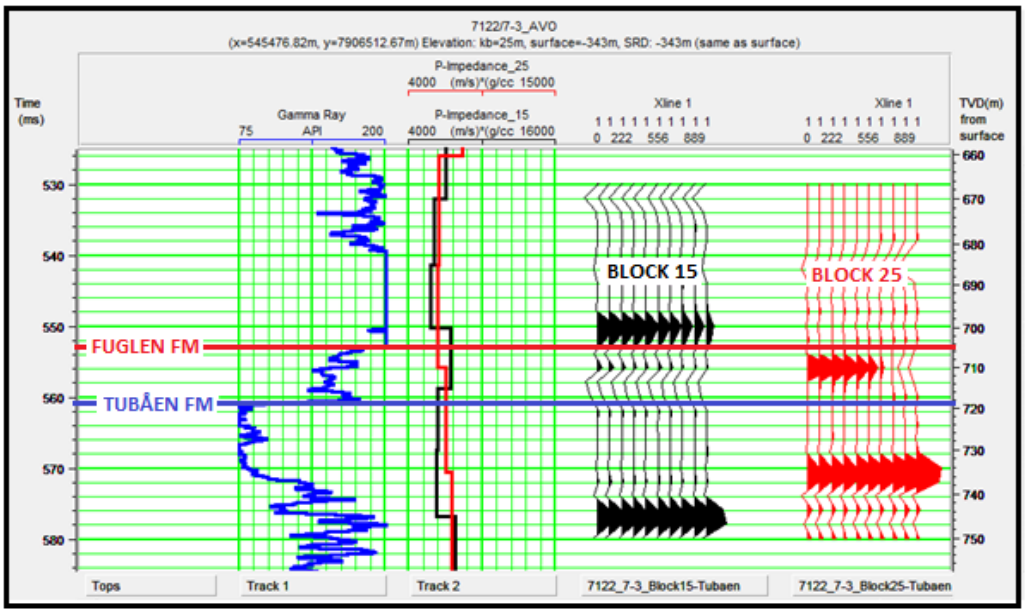

Fig. 4.17 Variation in synthetic NMO corrected CMP gathers with block size 15 and 25.

Block 25 shows data with a lower resolution and more noise introduced into the data. The reflection corresponding to top Fuglen and Tubåen occur at different depths depending on the

averaging size used. This has consequences in the resulting AVO response for the target reflectors.

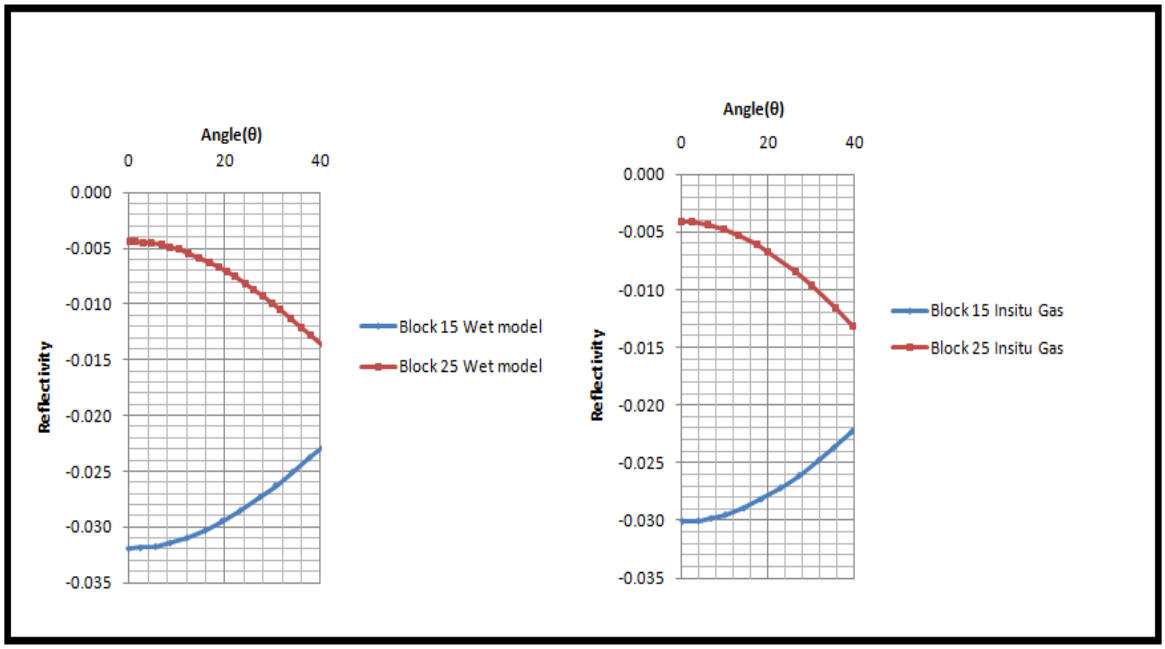

Fig. 4.18 Effect of block size on the AVO gradient.

Block 25 shows a negative gradient for both gas and brine models, meanwhile Block 15 shows a positive gradient for both brine and gas model scenarios (Figure 4.18). There is no significant change in the magnitude of the reflectivity for both block sizes before and after fluid substitution.

4.5.3 Kobbe and Tubåen angle dependent reflectivity comparison

The Tubåen reservoir is located at shallower depths (719m) than the Kobbe reservoir at 1440m BSF. The Fuglen cap rock to the Tubåen reservoir has different properties compared to the shales of the base Snadd Formation which serve as the cap rock for the Kobbe reservoir (Figure 4.6). The insitu fluid scenario for the Tubåen reservoir comprises of a gas-oil system, meanwhile the Kobbe reservoir is insitu oil filled. Both reservoirs fall within the zone affected by quartz cementation, as defined from the Vp-depth trend in this same well (7122/7-3) in chapter 3. Both reservoirs after 100% gas substitution show negative zero offset reflectivity. The Tubåen reservoir shows a typical class IV positive gradient, meanwhile Kobbe reservoir shows reflectivity increasing with offset characteristic of a class III as seen in Figure 4.19.

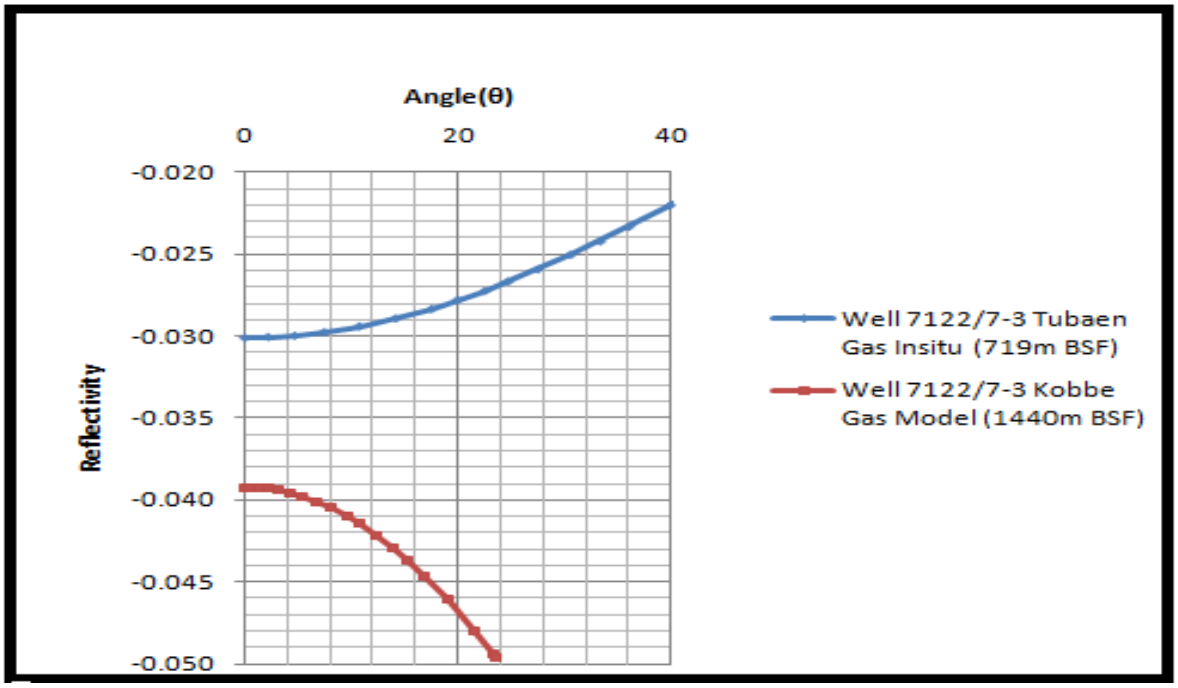

Figure 4.19 Gas scenario reflectivity versus offset for top Tubåen and Kobbe reservoir.

4.6 Discussion

4.6.1 Sensitivity study

The effect of fluid substitution on Vp, Vs, density, and Poisson's ratio in the Kobbe oil reservoir in well 7122/7-3 shows a consistent and interdependent relationship between these petrophysical properties. The Vp/Vs ratio determines the magnitude of the Poisson's ratio.

$$Vp = \sqrt{\frac{K+\frac{4}{3}\mu}{\rho}} \tag{4.12}$$

$$Vs = \sqrt{\frac{\mu}{\rho}} \tag{4.13}$$

K, μ, and ρ represent the effective saturated bulk modulus, shear modulus and density respectively. From equations 4.12 and 4.13, Vp and Vs will both increase with a decrease in effective density, if all other parameters are kept constant. The shear modulus is insensitive to fluid type and saturations, such that the shear modulus of rock frame is same as the shear modulus of the same rock saturated with fluid. Therefore the only varying parameter

controlling Vs is the density. The fluid properties for gas and oil used in this oil-gas two phase system are shown in Table 4.5. The density of gas is lower than density of oil, but the bulk modulus is the controlling factor determining Vp. Gas has much more lower compressibility compared to oil. As a result just a 10% gas input into the oil system, leads to a large percentage drop in Vp of 17.25%. This large change is due to a correspondingly large change in the saturated bulk modulus (Ksat) of the medium.

Table 4.9 Density and velocity cross plot with increasing gas saturation.

%Gas	Density(kg/m^3)	Ksat (Mpa)
0	2561.87	14800
10	2558.86	12200
50	2546.8	11800
90	2534.74	11600

A cross plot of density and the effective saturated bulk modulus (Ksat) in Figure 4.20 shows a consistent decrease in both parameters with increasing gas saturation. The effective fluid bulk modulus used as input in the Gassmann model for the different saturations, is calculated using the Reuss harmonic averaging in Hampson-Russel. This follows the assumption of a homogeneous saturation. However, a much larger decrease is observed for Ksat at the 10% gas saturation. Increasing the gas saturation after 10%, shows very low sensitivities in Ksat compared to density. The percentage change in Vp is higher for 50% and 90% Gas saturation, because these saturations were all compared to the insitu scenario as a reference.

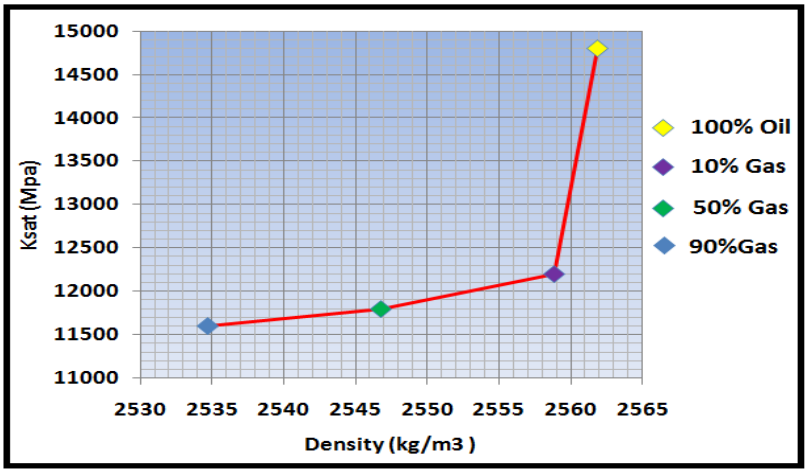

Fig. 4.20 Cross plot between the saturated bulk modulus and density color coded with gas saturation.

However it is evident that adding the gas saturation in the oil-gas system from 50% to 90%, leads to a difference of less than 2% change in the corresponding velocity at 90% gas saturation.

The effective bulk density consistently drops with increasing gas saturation. The model uses Voigt arithmetic average to calculate the effective bulk density. Meanwhile the Reuss harmonic average is used in calculating the effective fluid bulk modulus used in the Gassmann equation. Arithmetic averaging is used for the bulk density because density is a scalar quantity with no directional dependence.

Vs however shows a slight increase with increasing gas saturation. The percentage increase in Vs is roughly proportional to the percentage decrease in density. The Poisson's ratio shows the largest drop with increasing gas saturation. This is just due to the large change in Vp and an almost insignificant change in Vs on addition of gas into the system. When the percentage change of all four petrophysical parameters are compared using the same scale, their sensitivity can be ranked in the order; Poisson's ratio> Vp > density > Vs.

The corresponding synthetic seismic data for all three gas scenarios and the reference insitu oil scenario are shown in Figure 4.11. There is a slight increase in the strength of the internal reservoir reflectors. After introducing gas into the reservoir, the acoustic impedance contrast increases which also causes an increase in the strength of the reflectors. This change is observed just for the initial 10% gas saturation. With increasing gas saturations, the corresponding synthetic seismics look the same. This is largely due to the decreasing sensitivity of the effective saturated bulk modulus and Vp for progressively higher gas saturations. The percentage change in Vp is much larger than Vs and density and tend to control the observed synthetic seismic and AVO response for the different saturations. However negative reflection coefficients, show no apparent change in the reflection strength, just because the data is displayed in the normal polarity convention, in which the negative wiggled trace is not filled.

The top reservoir target reflector shows clearer differences with changing fluid saturations, when comparing the zero offset reflectivity for the different gas saturations. The change in reflectivity as expected is largest for the initial 10% gas. With increasing gas saturation, the reflection coefficient increases in magnitude because, the acoustic impedance contrast between the reservoir and the cap rock also increases.

4.6.2 Variation in half space models

The results shown in Figures 4.13 and 4.15 indicate that fluid substitution in both the Tubåen and Kobbe reservoirs has a significant influence on both the AVO intercept and the AVO gradient. The magnitude of the AVO intercept is controlled by the contrast in acoustic impedance meanwhile the AVO gradient is controlled much more by changes in the Poisson's ratio.

4.6.2.1 Tubåen AVO response

For the Tubåen reservoir, substituting oil for gas in well 7122/7-1 and 7122/7-2 causes an increase in the strength of the zero offset reflection coefficient (becomes more negative) (Figure 4.13). The presence of less dense gas reduces the impedance of the reservoir and increases the acoustic impedance contrast between the Fuglen cap rock and the underlying reservoir. Due to the dependence of Vp on the bulk modulus, the Poisson's ratio also decreases significantly in the presence of gas in both reservoirs (Figure 4.21).

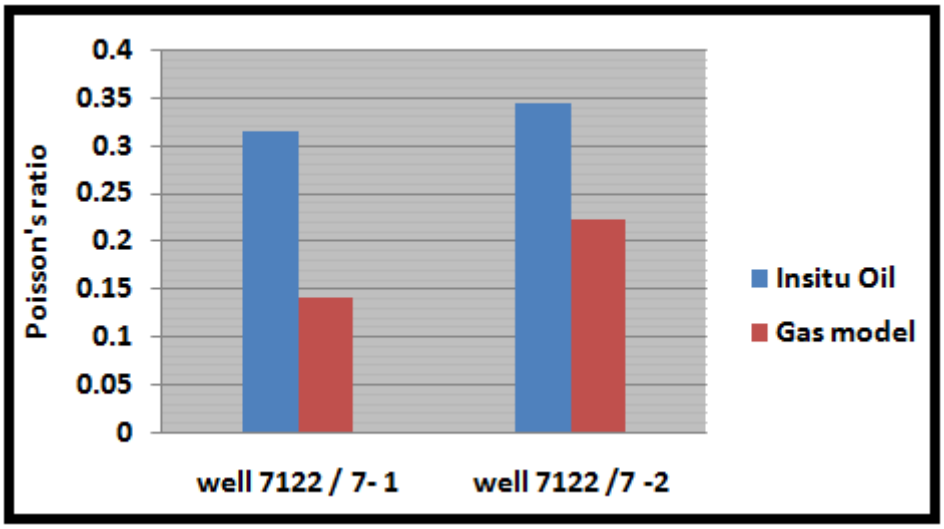

Fig. 4.21 Change in Poisson's ratio for Tubåen reservoir after fluid substitution.

The AVO gradient based on a first order linearized simplification of the Zoeppritz equation is given by:

$$B = \frac{1}{2}\frac{\Delta Vp}{Vp} - 2\left(\frac{Vs}{Vp}\right)^2\left(2\frac{\Delta Vs}{Vs} + \frac{\Delta\rho}{\rho}\right) \qquad (4.14)$$

From equation 4.14, it is evident that a decrease in the Poisson's ratio (Vp/Vs) leads to an increase in $(Vs/Vp)^2$ and causes the AVO gradient to become more negative. The increase in reflection coefficient with angle/offset (gradient) is stronger for the gas model in well 7122/7-1 than the corresponding gas model in well 7122/7-2. This can be correlated to the change in Poisson's ratio as a result of fluid substitution. The change in the Poisson's ratio for both the insitu oil scenario and the corresponding gas model is shown in Figure 4.21. The change in Poisson's ratio is larger for well 7122/7-1 compared to 7122/7-2 and explains why the gradient is stronger. Based on the gradient, well 7122/7-1 gas model is a class III (negative gradient) Tubåen reservoir; meanwhile in well 7122/7-2 Tubåen reservoir shows a positive gradient typical for class IV sands. Castagna et al. (1998), showed the contribution of Vp, Vs and density on the gradient of class III and class IV sands. Based on this study, contribution from the density contrast leads to positive gradients. Meanwhile a contribution from ΔVp leads to a negative gradient. However it was concluded that the key parameter controlling the gradient with offset is ΔVs. Combining this information together with Aki and Richards (1980) approximation, it is then possible to explain the difference in the positive and negative gradient for the Tubåen gas models.

$$R(\theta) = \frac{1}{2}(1 - 4\langle Vs\rangle^2 P^2)\frac{\Delta Vp}{\rho} + \frac{1}{2Cos^2\theta}\frac{\Delta Vp}{\langle\rho\rangle} - 4\langle Vs\rangle^2 p^2 \frac{\Delta Vs}{\langle Vs\rangle} \quad (4.15)$$

Where P is the ray parameter given by (Sin θ/Vp) and θ is the average of the angle of incidence and refraction. The remaining terms are linearized described in equations 4.10 and 4.11.

Table 4.10 Change in Vs for Tubåen reservoir.

Well and Pore Fluid		**Reservoir (Tubåen) Vs (m/s)**	**Cap Rock (Fuglen) Vs (m/s)**	**(ΔVs)**
7122/7-1	Insitu oil	1710.17	1800.36	-
	Gas model	2024.23		+
7122/7-2	Insitu oil	1540.43	1676.22	-
	Gas model	1810.84		+
7122/7-3	Insitu gas	1722.55	1289.49	+

Mode conversion of Vp into Vs occurs only for angles of incidence greater than zero. This implies that ΔVs has no effect on the zero offset reflection coefficient. From equation 4.15, a

positive ΔVs (increase in shear velocity across the cap rock-reservoir interface) increases the shear contribution for increasing offsets, leading to an increase in the total amplitude with offset. This leads to a more class III type signature. A reverse scenario occurs for a negative ΔVs.

For the Tubåen reservoir, the insitu oil models in well 7122/7-1 and 7122/7-2 show a decrease in shear velocity across the cap rock- reservoir interface (Table 4.10). This correlates well with the corresponding class IV signatures for this scenario. After substituting oil for gas, ΔVs becomes positive and correlates with an increase in reflection coefficients at higher angles/offsets in a class III type response. However, a classical class IV response is usually anticipated when a high velocity unit (‘’tight cap rock’’) such as the Fuglen cap rock overlies a porous reservoir. This is the case observed insitu in well 7122/7-3, using direct shear wave measurements as opposed to the other wells using the linear transform from the measured Vp according to Castagna et al. (1985).

4.6.2.2 Kobbe AVO response

There is a change of class observed for all the Kobbe insitu scenarios in Figure 4.15 except for well 7122/7-3, after fluid substitution. The insitu brine case in well 7122/7-5 shows the smallest zero offset reflection coefficient. This is due to a lower acoustic impedance contrast with the overlying cap rock which is brine filled. The corresponding gas model for this well shows the strongest zero offset reflection coefficient. This is consistent with the fact that, the acoustic impedance contrast for brine and gas larger than that for oil and gas as is the case in the other wells. The base of the Snadd formation, which serves as the cap rock for the Kobbe reservoir, is not a ‘tight cap’ rock compared to the Fuglen cap rock. The introduction of gas, lowers the Poisson’s ratio in all the wells, and causes both the AVO intercept and AVO gradient to become more negative. Except for well 7122/7-3, all the other wells show ‘’less positive gradients’’ after fluid replacement with gas. The positive ΔVs observed for all the gas models after fluid substitution (Table 4.11), is also consistent with equation 4.15, leading to an enhanced total amplitude increase with offset. Well 7122/7-4 shows the strongest gradient compared to the insitu oil model. This is consistent with the largest observed Poisson’s ratio change for well 7122/7-4. On the other hand well 7122/7-3 in Figure 4.22 shows the smallest change in Poisson’s ratio, and therefore very similar gradients before and after fluid substitution.

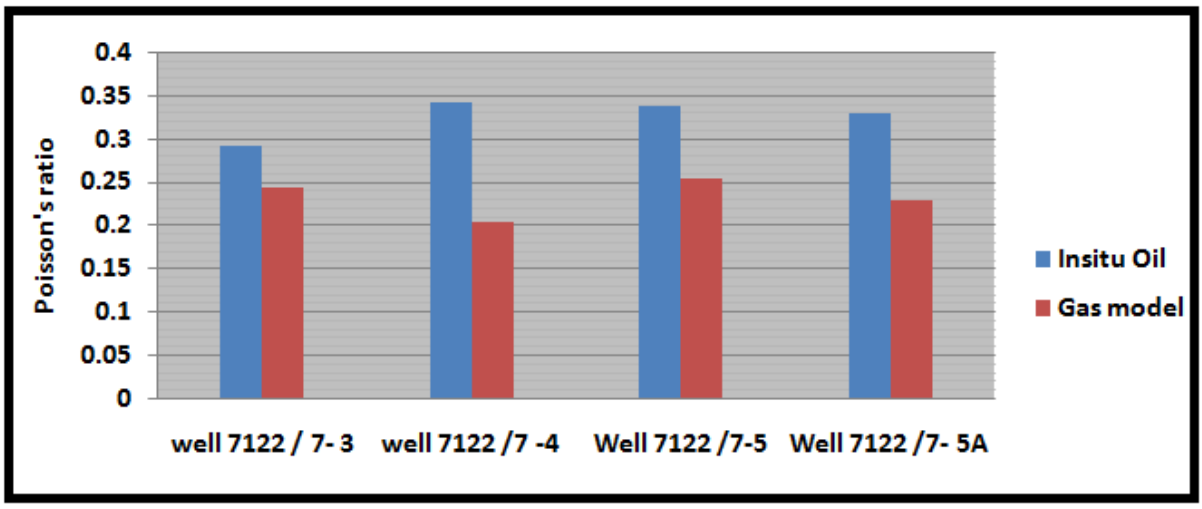

Fig. 4.22 Change in Poisson's ratio for Kobbe reservoir after fluid substitution.

Table 4.11 Change in Vs for Kobbe reservoir.

Well and Pore Fluid		Reservoir (Kobbe) Vs (m/s)	Cap Rock (Snadd) Vs (m/s)	(ΔVs)
7122/7-3	Insitu oil	1724.19	1497.96	+
	Gas model	1765.37		+
7122/7-4	Insitu oil	1557.16	1528.63	+
	Gas model	1836.85		+
7122/7-5	Insitu brine	1596.58	1499.48	+
	Gas model	1671.19		+
7122/7-5A	Insitu oil	1661.68	1614.74	+
	Gas model	1907.06		+

4.6.2.3 Tubåen and Kobbe AVO gas response and the effects of block size variation

Differences in the strength of the cap rocks are known to influence the AVO response of the underlying reservoirs (Lars et al., 2006, Avseth et al., 2008). The difference in class III and IV for Kobbe and Tubåen respectively in Figure 4.19 may be due to a combined effect of compaction and differences in the cap rock. The Fuglen formation is a ‘’tight cap rock’’ unlike the Snadd formation. Similar observations for ‘tight cap rocks’ have been observed by Castagna et al. (1998). Despite this, the zero offset coefficient for the Snadd gas model, is

larger than for the Tubåen reservoir. This is possibly due to the fact that the model uses frame properties of pure quartz.

The target reflector (B) for the insitu Tubåen reservoir in Figure 4.23 is seen as a strong negative reflector and can be followed in block 15, but this same reflector is averaged out in block 25. This explains the difference in the AVO response. The zero offset coefficients for the top Tubåen is almost zero for a gas model.

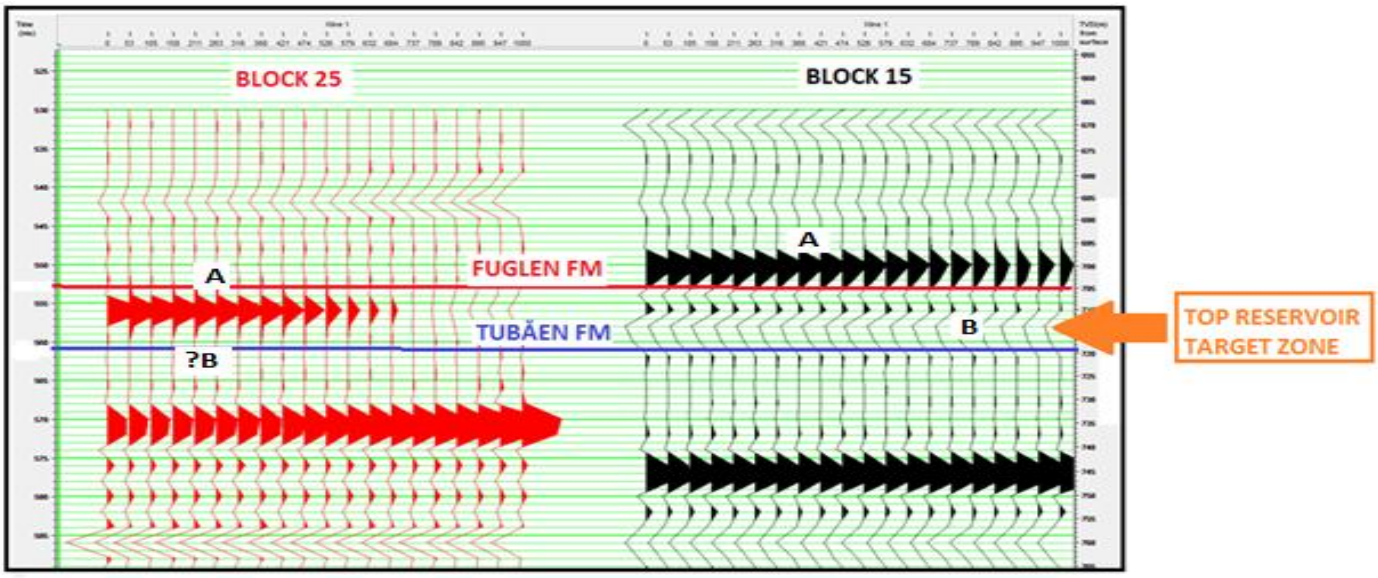

Fig. 4.23 NMO corrected synthetic CDP gathers for block 25 and block 15 for top Tubåen reservoir in well 7122/7-3.

The modeled reservoir interval is too thin to be observed in the seismic due to the large averaging used. Top Fuglen (cap rock) is seen as a strong positive reflector and can be correlated across both synthetic sections. Amount of noise in the data is increasing with increasing block size. This is due to a reduction in resolution with increasing block size. The phase change observed in block 25 may be the result of effects of NMO stretching for large offsets for the top Fuglen reservoir in block 25. This study puts more emphasis on the zero offset reflection coefficient, and the AVO gradient for near offsets, to minimize possible effects of NMO stretching in the synthetic seismic section.

4.7 Uncertainties in the modeled scenarios

Due to the absence of core data there was no control on the mineralogy. Differences in the gas models obtained using Gassmann fluid substitution and the insitu gas model in well 7122/7-3

may arise due to over simplifications made in the model. The frame properties were set to be equal to that of pure quartz. These assumptions impose a limitation in the interpretation of the AVO response. This is because observed reservoir heterogeneity from the gamma ray log has not been taken into account as shown in Figure 4.24.

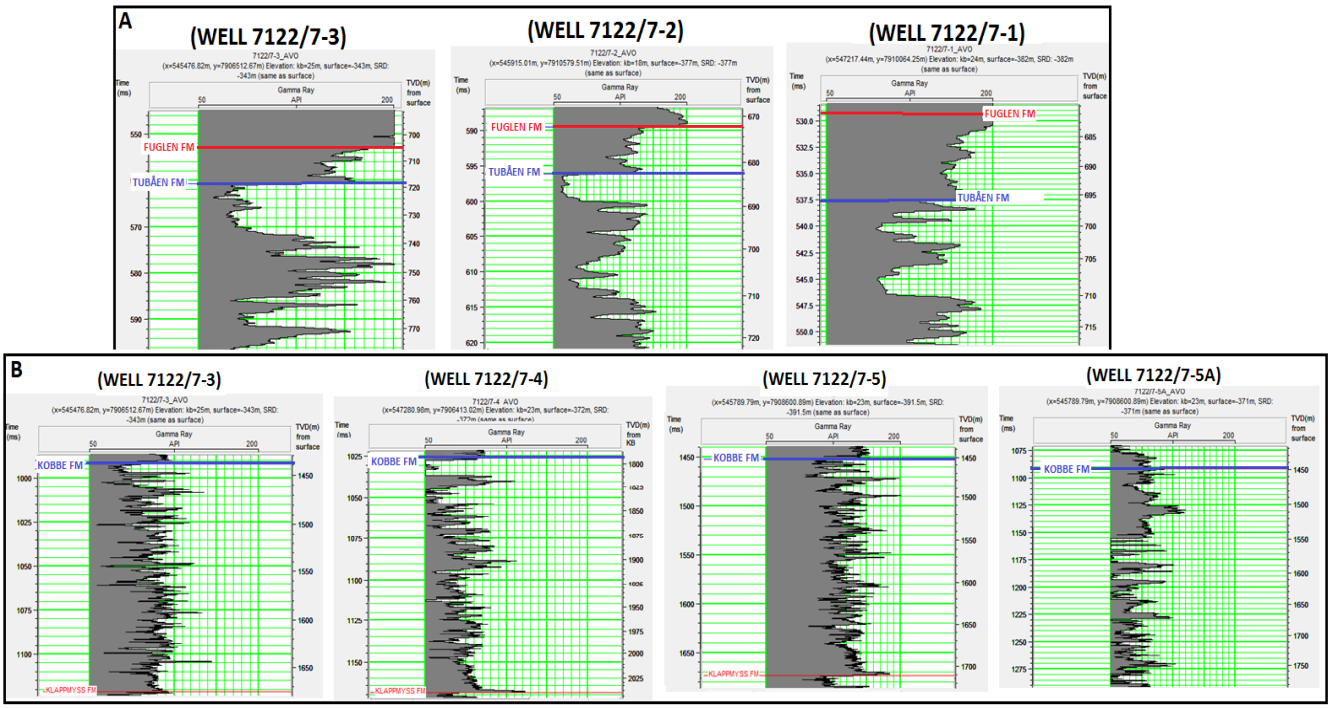

Fig. 4.24 Gamma ray logs for Tubåen (A) and Kobbe (B) reservoirs.

These siliciclastic reservoirs have differential amounts of shale even for the same reservoir in the different wells. The presence of shale increases the Vp/Vs ratio, which influences the AVO gradient. In addition, shales usually have unconnected pores, which violates Gassmann's assumption of total communication in the pore space.

The pressure dependence on the output for fluid substitution has not been taken into account, due to the absence of data to constrain the different pressure regimes in both the Kobbe and Tubåen reservoirs, located at different depths. As a result, the input porosity is set equal to the output porosity, and this distorts the effect of compaction on the AVO response. The effects of biodegradation have also not been taken into account. The oil in the Kobbe reservoir is not biodegraded (NPD Factpages), unlike the hydrocarbon accumulations of the Tubåen formation. Biodegraded oils are usually denser than non biodegraded oils. This difference may also pose limitations to the interpretations discussed in this study.

CHAPTER 5 SUMMARY AND CONCLUSION

5.1 Summary and conclusion

The Barents shelf area has recorded a higher success rate than the Norwegian North Sea in terms of initial frontier exploration efforts. Multiple source rocks are also found at different stratigraphic intervals, including the wide spread Upper Jurassic-Cretaceous Hekkingen Formation which is equivalent to the Kimmeridge shale unit in the North Sea. The distance to potential markets, climate, dominant gas products, large water depths, and the Cenozoic uplift pose a lot of challenges for frontier exploration, development and production from the discovered oil and gas fields.

The PDO approved Goliat oil field located on the Finnmark platform, is one among a series of rather few oil finds among the major gas reserves such as the Snøhvit and Shtokmann gas fields. The occurrence of non-cogenetic gas in this field is a good sign of a live petroleum system in the area. Uplift had devastating consequences not just to the source rocks, but also the reservoir and cap rocks in this area. The main reservoir intervals include; the Tubåen, Fruholmen, Snadd, Kobbe, Klappmyss, Havert Formations. However this work lays emphasis on the Kobbe and Tubåen reservoirs including their cap rocks (base Snadd and Fuglen Formations respectively). The major structure cutting through this field is the Troms Finnmark Fault Complex (TFFC). The main structural trap is a roll over anticline.

Compaction trends in the Goliat have been investigated by comparing a suite petrophysical well log data, and experimental laboratory compaction trends. Different clay – clay and clay – silt curves have been utilized. Generally as a function of depth, Vp and density increase meanwhile the porosity reduces as expected. The transition from mechanical to chemical compaction for siliciclastic rocks has been investigated using two techniques. First by recognizing an abrupt increase in the Vp – depth trend within the same lithology (inferred from the gamma ray log. Incorporating information from a shear modulus-porosity cross plot also helped to constrain the depth at which this transition occurs. There are uncertainties in the paleogeothermal gradient, and the actual mineralogy of the rock units discussed in this work.

AVO fluid replacement modeling of the Kobbe and Tubåen reservoir provides additional insight into the rock properties of these reservoir rocks. Despite the major limitations and simplifications in the Gassmann fluid replacement model, it still provides a robust approach. The AVO signature is not dependent on the properties of the reservoir alone but also on the overburden through which the seismic pulse propagates. As a result, fluid replacement modeling needs to take into account not just the properties of the reservoir but the cap rock as well. Using a constant matrix property obliterates any variation in the AVO response due to differential amounts of clay in the reservoir. Also setting input porosity same as the output porosity removes the effect of pore pressure (mechanical compaction) which is also an important parameter that may give rise to AVO anomalies.

However, despite these simplistic assumptions and limitations the following conclusions can be arrived at;

- The Vp depth trends in the Goliat Field generally increase with depth, except for some anomalous zones. These zones show decreasing Vp with depth due to a combined influence of pore fluid, pore pressure and the presence of source rocks. The chemical compaction trend shows a smaller increase of Vp with depth (less sensitive to increasing compaction) due to enhanced strength of the grain framework as a result of cementation. Vp and density tend to show an inverse relationship with depth. The source rock (Hekkingen Formation) tends to show a characteristic velocity inversion with depth even though it has been affected by quartz cementation based on the well log data. Sand and shale tend to show very different compaction trends. This is most likely due to differences in the grains size.

- The minimum estimate of the exhumation experienced by the Goliat Field is 700m based on experimental laboratory compaction Kaolinite-silt (50:50) curve. Meanwhile an upper limit based on pure kaolinite stands at 1500m based on a pure kaolinite laboratory compaction curve. Different estimates are obtained between these two limits depending on the laboratory compaction curve used. However XRD analysis for the shallow formations in the mechanical compaction regime will provide the adequate mineralogical control to constrain these results.

- The present day transition from mechanical to chemical compaction occurs between 600-700m BSF, as defined by the Vp depth trend and the porosity/shear modulus cross plot. This transition shows a clear change from mudstone to shale with a significant

increase in the shear modulus as a result on the onset of chemical compaction. This temperature controlled transition occurs at similar depths in all the wells. The low temperatures of transition estimated at 41^0C using a geothermal gradient of 31^0C/Km has been attributed to a silica phase transformation, rather than a smectite to illite transformation reaction. Future SEM petrographic analysis at depth intervals above and below the transition zone will be important to ascertain this claim.

- The Poisson's ratio and Vp tend to be most sensitive to changing gas saturation in the Kobbe oil-gas two phase system. Density and Vs on the other hand are only relatively slightly sensitive. Only Vs shows an increase with increasing gas saturation due to decreasing effective bulk density. However after 10% gas saturation, there is a significant drop in the sensitivity of these parameters and no observed change in the synthetic seismic. The key parameter controlling the sensitivity of Vp is the saturated bulk modulus which is also only sensitive to the initial 10% addition gas to the full oil system.

- The insitu (real) AVO response for the Tubåen reservoir with a tight cap rock shows a typical class IV behavior. Meanwhile the insitu (real) Kobbe AVO response shows a class III signature. The corresponding modeled scenarios for gas show a positive ΔVs contribution which enhances the total increase of amplitude (becomes more negative) with offset.

- Block sizes greater than 25m average out thin reservoir intervals such as the Tubåen reservoir. A block size of 15m has the potential to separate both cap rock and reservoir and hence has a better resolution. However this resolution in the synthetic seismic cannot be feasibly achieved in a real seismic survey, due to wave dispersion and attenuation effects.

The exhumation estimates obtained can be used to correct porosity depth relationships used in basin modeling and reservoir characterization workflows.Meanwhile AVO modeling may be used as a complimentary tool with 3D seismic in reservoir monitoring during production since the effects of changing saturation are less visible on the stacked seismic data compared to the changes in the reflection coefficient as a function of offset in the prestack domain.

REFERENCES

AASE, N. E., BJORKUM, P. A. & NADEAU, P. H. 1996. The effect of grain-coating microquartz on preservation of reservoir porosity. AAPG Bulletin-American Association of Petroleum Geologists, 80**,** 1654-1673.

AKI, K. & RICHARDS, P. G. 1980. Quantitative seismology: theory and methods, San Francisco, Freeman.

AVSETH, P., DRÆGE, A., AART-JAN, V. W., TOR, A. J. & ARILD, J. 2008. Shale rock physics and implications for AVO analysis: A North Sea demonstration. The Leading Edge, 277, 788.

AVSETH, P., MUKERJI, T., MAVKO, G. & DVORKIN, J. 2010. Rock-physics diagnostics of depositional texture, diagenetic alterations, and reservoir heterogeneity in high-porosity siliciclastic sediments and rocks --- A review of selected models and suggested work flows. Geophysics, 75**,** 75A31-75A47.

BATZLE, M. L., HAN, D. & CASTAGNA, J. P. 2005. Fluid effects on bright spot and AVO analysis. SEG Technical Program Expanded Abstracts, 14, 1119 (1995).

BJØRLYKKE, k. & JAREN, H. 2010. ‘’Sandstones and Sandstone reservoirs’’. In BJØRLYKKE, K. 2010. Petroleum Geoscience: from Sedimentary Environments to Rock Physics, Berlin, Heidelberg, Springer-Verlag Berlin Heidelberg, 113 – 140.

CASTAGNA, J. P., BATZLE, M. L. & EASTWOOD, R. L. 1985. Relationships between Compressional-Wave and Shear-Wave Velocities in Clastic Silicate Rocks. Geophysics, 50**,** 571-581.

CASTAGNA, J. P., HERBERT, W. S. & DOUGLAS, J. F. 1998. Framework for AVO gradient and intercept interpretation. Geophysics, 63**,** 948-956.

DALLAND , A., WORSLEY, D. & OFSTAD, K. 1988. A lithostratigraphic scheme for the Mesozoic and Cenoizoic succession offshore mid- and northern Norway. NPD-Bulletin, 4**,** 65.

DORE, A. G. 1995. Barents Sea geology ,petroleum resources and commercial potential. Arctic, 48**,** 207-221.

DVORKIN, J. 2008. Yet another Vs equation. Geophysics, 73(2)**,** E35-E39.

Eni Norway Goliat Factpage,(http://www.eninorge.no/EniNo.nsf/page /DED71D42177627E0C12574E60040DAF9?OpenDocument&Lang=english),accessed (02.02.11).

FALEIDE, J. I., GUDLAUGSSON, S. T. & JACQUART, G. 1984. Evolution of the western Barents Sea. Marine and Petroleum Geology, 1**,** 123-128, IN1-IN4, 129-136, IN5-IN8, 137-150.

FAWAD, M., MONDOL, N. H., JAHREN, J. & BJØRLYKKE, K. 2010. Microfabric and rock properties of experimentally compressed silt-clay mixtures. Marine and Petroleum Geology, 27**,** 1698-1712.

GABRIELSEN, R. H., FÆRSETH, R. B., JENSEN, L. N., KALHEIM, J. E. & RIIS, F. 1990. Structural elements of the Norwegian Continental Shelf Part I : The Barents Sea Region. NPD-Bulletin, 6**,** 33.

GASSMANN, F. 1951. Uber Die elastizitat poroser medien. Vier, der Natur Gesellschaft.

GELIUS, L.-J. & JOHANSEN, T. A. 2010. Petroleum geophysics, Bergen, Unigeo.

GLØRSTAD-CLARK, E., FALEIDE, J. I., LUNDSCHIEN, B. A. & NYSTUEN, J. P. 2010. Triassic seismic sequence stratigraphy and paleogeography of the western Barents Sea area. Marine and Petroleum Geology, 27**,** 1448-1475.

GOFFREY, R. 2007. Advances in reservoir characterization. Exploration and Production.

HAN, D., NUR, A. & MORGAN, D. 1986. Effects of porosity and clay content on the wave velocities in sandstones. Geophysics, 51(11)**,** 2093-2107.

JAPSEN, P. 1999. Overpressured Cenozoic shale mapped from velocity anomalies relative to a baseline for marine shale, North Sea. Petroleum Geoscience, 5**,** 321-336.

JARVIS, K. 2006. Intergrating Well and Seismic Data for Reservoir Characterisation: Risks and Rewards.

JOHANSEN, S. E., OSTISTY, B. K., BIRKELAND, Ø., CRISTENSEN, O., CHEREDEEV, S. I., IGNATENKO, E. A. & MARGULIS 1993. Hydrocarbon potential in the Barents Sea region: Play distribution and potential

Norwegian Petroleum Directorate (NPD) Factpages, PDO approved, (http://factpages.npd.no/factpages/Default.aspx?culture=en) accessed (02.02.11).

Norwegian Petroleum Society (NPF) Special Publication 2**,** 273–320.

KRIEF, M., GARAT, J., STELLINGWERFF, J. & VENTRE, J. 1990. A petrophysical interpretation using the velocities of P and S waves. The Log Analyst**,** 355-369.

LARS, H., KARSTEN, M. & ALSING, S. 2006. Improving AVO modeling using geological knowledge, 4 examples from the Norwegian Continental Shelf. SEG Technical Program Expanded Abstracts, 25, 259.

LOENG, H. 1991. Features of the physical oceanographic conditions of the barents sea. Polar Research, 10**,** 5-18.

MARCUSSEN, O., MAAST, T. E., MONDOL, N. H., JAHREN, J. & BJØRLYKKE, K. 2010. Changes in physical properties of a reservoir sandstone as a function of burial depth - The Etive Formation, northern North Sea. Marine and Petroleum Geology, 27**,** 1725-1735.

MARCUSSEN, O., THYBERG, B. I., PELTONEN, C., JAHREN, J., BJØRLYKKE, K. & FALEIDE, J. I. 2009. Physical properties of Cenozoic mudstones from the northern North Sea: Impact of clay mineralogy on compaction trends. AAPG Bulletin, 93**,** 127-150.

MOHAGHEGH, S., AREFI, R., AMERI, S., AMINIAND, K. & NUTTER, R. 1996. Petroleum reservoir characterization with the aid of artificial neural networks. Journal of Petroleum Science and Engineering, 16**,** 263-274.

MONDOL, N. H. (2011). Personal communication, University of Oslo, Norway.

MONDOL, N. H. 2010. ‘’Seismic Exploration’’. In BJØRLYKKE, K. 2010. Petroleum Geoscience: from Sedimentary Environments to Rock Physics, Berlin, Heidelberg, Springer-Verlag Berlin Heidelberg, 375 – 402.

MONDOL, N. H., AVSETH, P., FAWAD, M. & SMITH, T. 2010. Vs Prediction in Unconsolidated Sands - Physical and Geological Controls on Shear Wave Velocities. 72nd EAGE Conference & Exhibition incorporating SPE EUROPEC Barcelona, Spain.

MONDOL, N. H., BJØRLYKKE, K. & JAHREN, J. 2008. Experimental compaction of Kaolinite Aggregates: Effect of Grain Size on Mudrock Properties. EAGE Extended Abstract, I037.

MONDOL, N. H., BJØRLYKKE, K. & JAHREN, J. 2008a. Experimental compaction of clays: relationship between permeability and petrophysical properties in mudstones. Petroleum Geoscience, 14**,** 319-337.

MONDOL, N. H., BJØRLYKKE, K., JAHREN, J. & HOEG, K. 2007. Experimental mechanical compaction of clay mineral aggregates - Changes in physical properties of mudstones during burial. Marine and Petroleum Geology, 24**,** 289-311.

MONDOL, N. H., FAWAD, M., GRANDE, L., JAHREN, J. & BJØRLYKKE, K. 2009a. Vs Estimation in Mudrocks - Implications about Mineralogy and Grain Size. 71st EAGE Conference and Exhibition. Amsterdam,The Netherlands.

MONDOL, N. H., FAWAD, M., GRANDE, L., JAHREN, J. & BJØRLYKKE, K. 2009b. Vs estimation in mudrocks - Implications about mineralogy and grain size. EAGE Extended Abstract, Z012.

MØRK, A., EMBRY, A., F. & WEITSCHAT, W. Year. Triassic transgressive-regressive cycles in the Sverdrup Basin, Svalbard and the Barents Shelf. In: Norwegian Society conference, 1989 Graham and Trotman,London. 113-130.

MØRK, A., KNARUD , R. & WORSLEY, D. 1982. Depositional and diagenetic environments of the Triassic and Lower Jurassic succession of Svalbard. Canadian Society of Geologist,Calgary Alberta, Canada**,** 371e398.

OHM, S. E. & KARLSEN, D. A. 2008. Geochemically driven exploration models in uplifted areas : Examples from the Norwegian Barents Sea. AAPG Bulletin, 92,NO.9**,** 1191-1223.

RIIS, F., LUNDSCHIEN, B. A., HOY, T., MORK, A. & MORK, M. B. E. 2008. Evolution of the Triassic shelf in the northern Barents Sea region. Polar Research, 27**,** 318-338.

ROALDSET, E. & HE, W. 1995. Silica-phase Transformation of Opal-A to Opal-CT to Quartz-an experimental Approach.Report.: Department of Geology and Mineral Resources Engineering, Norwegian Insitute of Technology, Trondheim.

RUTHERFORD, S. R. & WILLIAMS, R. H. 1989. AMPLITUDE-VERSUS-OFFSET VARIATIONS IN GAS SANDS. Geophysics, 54**,** 680-688.

SOLHEIM, A. & ELVERHOI, A. 1993. GAS-RELATED SEA-FLOOR CRATERS IN THE BARENTS SEA. Geo-Marine Letters, 13**,** 235-243.

STAINFORTH, J. G. & REINDERS, J. E. A. 1990. Primary migration of hydrocarbons by diffusion through organic-matter networks, and its effect on oil and gas generation. Organic Geochemistry, 16**,** 61-74.

STORVOLL, V., BJORLYKKE, K. & MONDOL, N. H. 2005. Velocity-depth trends in mesozoic and cenozoic sediments from the Norwegian shelf. AAPG Bulletin, 89**,** 359-381.

THYBERG, B., JAHREN, J., WINJE, T., BJORLYKKE, K., FALEIDE, J. I. & MARCUSSEN, O. 2010. Quartz cementation in Late Cretaceous mudstones, northern North Sea: Changes in rock properties due to dissolution of smectite and precipitation of micro-quartz crystals. Marine and Petroleum Geology, 27**,** 1752-1764.

VERNIK, L. & LIU, X. Z. 1997. Velocity anisotropy in shales: A petrophysical study. Geophysics, 62**,** 521-532.

WALDERHAUG, O. 1994. Precipitation rates for quartz cement in sandstones determined by fluid-inclusion microthermometry and temperature-history modeling. Journal of Sedimentary Research Section a-Sedimentary Petrology and Processes, 64**,** 324-333.

WORSLEY, D. 2008. The post-Caledonian development of Svalbard and the western Barents Sea Polar Research 27**,** 298 -317

WORSLEY D., AGA O.J., DALLAND A., A., E. & A., T. 1986. The geological history of Svalbard- evolution of an Arctic archipelago

XU, S. & WHITE, R. E. 1996. A physical model for shear-wave velocity prediction. Geophysical Prospecting, 44(4)**,** 687-717.

YONGYI, L., JONATHAN, D. & YONG, X. 2007. Practical aspects of AVO modeling. The Leading Edge, 26(3)**,** 295.

APPENDIX

LIST OF FIGURES

Chapter 1 Introduction

Chapter 2 Regional Geologic Setting

Chapter 3 Compaction and Rock Properties

Chapter 4 AVO Modeling

LIST OF TABLES

Chapter 1 General Introduction

Chapter 2 Regional Geologic Setting

Chapter 4 AVO Modeling